Akademia Górniczo-Hutnicza im. Stanisława Staszica
Wydział: Inżynierii Metali i Informatyki Przemysłowej
Katedra: Metaloznawstwa i Metalurgii Proszków

Rozprawa doktorska

"Microstructure stability of second and fourth generation single crystal nickel-base superalloys during high temperature creep deformation"

mgr inż. Maciej Ziętara

Promotor: Prof. dr hab. inż. Aleksandra Czyrska-Filemonowicz

Kraków 2011

Table of contents

I. INTRODUCTION……...1

1. Introduction……...1

II. LITERATURE REVIEW……...2

1. General aspects of single crystal nickel-base superalloys…….....2
   1.1. Application…….2
   1.2. Generations……2
   1.3. Evolution of the properties……6
   1.4. Technology and manufacturing…….7
   1.5. Solidification and microstructure (as cast)……...11
   1.6. Heat treatment and microstructure……...13

2. Constituent phases of single crystal nickel-base superalloys……..15
   2.1. Alloy elements and their microstructural effects…….15
   2.2. γ phase……..17
   2.3. γ' phase…….18
      2.3.1. Impact of γ' volume fraction……19
      2.3.2. The role of γ/γ' misfit……20
   2.4. Carbides and borides……....21
   2.5. Topologically-Closed-Packed phases……..22

3. High temperature microstructural stability of single crystal nickel-base superalloys during ageing, without external stresses…….23

4. Mechanisms of Single Crystal superalloys creep deformation……..24

5. Microstructural evolution during high temperature creep deformation (rafting)……25

III. EXPERIMENTAL PROCEDURE……..30

1. Materials investigated…….30
   1.1. Chemical composition and heat treatment……...30
2. Creep tests……...30
   2.1. Geometry of the specimens……..31
   2.2. Creep conditions……..31
3. Specimens preparation for structure and surface investigation ……..……32
4. X-ray diffractometry……...34
5. Light microscopy……34
6. Scanning electron microscopy……35
7. Transmission electron microscopy…….35
8. Nano-indentation hardness measurements by Atomic Force Microscopy…….36
9. Image analysis…….37
   9.1. Stereological procedure for characterization of baseline materials…….37

9.2. Stereological procedure for characterization the degree of rafting……..39
10. Focused Ion Beam tomography……..41

IV. RESULTS ……..……44

1. Microstructural characterization of second generation nickel-base superalloy PWA 1484…..…….....44
   1.1. Baseline material……...……44
   1.2. Creep deformed material…….……...46
2. Microstructural characterization of fourth generation nickel-base superalloy PWA1497……...…55
   2.1. Baseline material……55
   2.2. Creep deformed material……57
3. Comparison of creep induced microstructural changes of 2nd and 4th generation superalloys……66
   3.1. Comparison of superalloys creep tested under the same conditions……..66
   3.2. Comparison of superalloys creep tested at different stress……..…68
4. High temperature microstructural stability of both superalloys during ageing…….71
5. The γ/γ' misfit measurements by X-ray diffractometry …….……...76
6. Nanoindentation hardness measurements by atomic force microscopy……77
7. Focused Ion Beam tomography of 4th generation PWA 1497 superalloy……82

V. SUMMARY AND DISCUSSION…….85

VI. CONCLUSIONS……...91

LITERATURE……..93

LIST OF SYMBOLS……....99

ACKNOWLEDGEMENT……..100

I. INTRODUCTION

1. Introduction

Single crystal (SC)* nickel-base superalloys have been developed over the past 40 years especially for modern gas turbine applications. Their introduction into commercial use as turbine blades in aero-engines is regarded as one of the most significant technological achievements of the past two decades [1]. This group of alloys have superior mechanical properties such as creep resistance and high temperature strength. They are hardened by a high volume fraction of the ordered γ' phase, which is coherently precipitated in the γ matrix. These materials are mainly applied as turbine blades and vanes in aero-engines and industrial gas turbines. Turbine blades operate at high temperature under a centrifugal force causing creep deformation of the material, which leads to so-called rafting (i.e. directional coarsening). A characteristic microstructural property of SC superalloys is the ability of cubic γ' phase particles to transform under the influence of stress and temperature into the plates (rafts). The rafts develop in the early stages of creep at high temperature (about 1000 °C) and low stress (about 100 MPa). Rafting appears to be an essential factor determining creep strength of nickel-base single crystal superalloys at high temperature and influencing their applications [2].

A new, 4th generation single crystal superalloy has been jointly developed by GE Aircraft Engines (GEAE), Pratt & Whitney (P&W) and NASA. The focus of the effort was to develop a turbine airfoil alloy with long-term durability for use in the High Speed Civil Transport. In order to achieve adequate long time strength improvements at moderate temperature and to retain good microstructure stability, it was necessary to make significant composition changes from 2nd and 3rd generation single crystal superalloys. These include lower chromium levels, higher cobalt and rhenium levels and the addition of a new alloying element, ruthenium. The new superalloy is known as MX4 at GEAE and PWA 1497 at P&W [3].

The aim of this study was to compare the microstructure stability of 4th (PWA 1497) and 2nd (PWA 1484) generation SC nickel-base superalloys, during creep deformation at 982 ˚C and various stresses.

* Single crystal are labeled in the literature as SC or SX

II. LITERATURE REVIEW

1. General aspects of single crystal nickel-base superalloys

1.1. Application

Single crystal (SC) superalloys are a group of nickel-base superalloys. They exhibit superior high temperature strength (at temperatures as high as 0.8 T_m of their melting point) and hot corrosion resistance compared to the conventionally produced superalloys.

The SC superalloys are used for manufacturing turbine blades, nozzle guide vanes, and majority of the other parts of the hot gas path for civil and military aircraft gas turbine engines, as well as for stationary gas turbine plants [4, 5, 6]. The main types of turbine blades were shown on Fig. 1 [7].

Fig. 1. Main types of turbine blades [7].

1.2. Generations

Over the past 60 years, the turbine blade temperature capability has increased significantly. Some of the advances have been achieved through improved alloy

compositions, others have been accomplished by major innovation in processing and cooling technology.

The superior mechanical properties of SC alloys are achieved due to the optimization of chemical composition, heat treatment and microstructure. A great advantage of SC superalloys over conventionally cast (CC) equiaxed-grain polycrystalline superalloys and directionally solidified columnar-grained (DS) superalloys is the improvement of creep resistance by elimination of grain boundaries, which are easy diffusion paths. Additionaly the directional solidification process of DS and SC superalloys provides a low Young's modulus <001> crystallographic direction, which influences fatigue resistance [4].

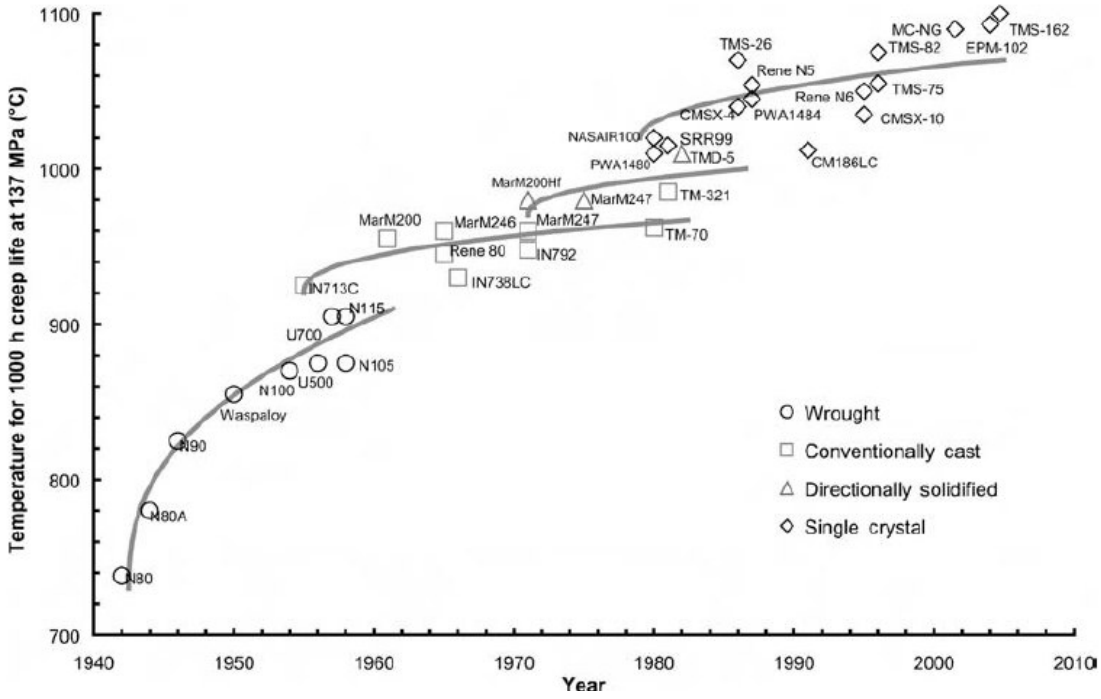

Fig. 2. Evolution of the high-temperature capability of the superalloys over 60 year period since their emergence in 1940s [4]

R.C. Reed [4] presented evolution diagram (Fig. 2) for the superalloys and process development which has occurred since the first superalloys appeared in the 1940s. The data relate to the materials and processes for turbine blades, so that the creep performance (here

taken as the highest temperature at which rupture occurs in not less then 1000h at 137 MPa) is suitable measure for the progress which has been made [4]. As a comparison, Figure 3 shows the evolution of high strength Ni-base superalloys for turbine blade application at Pratt & Whitney company.

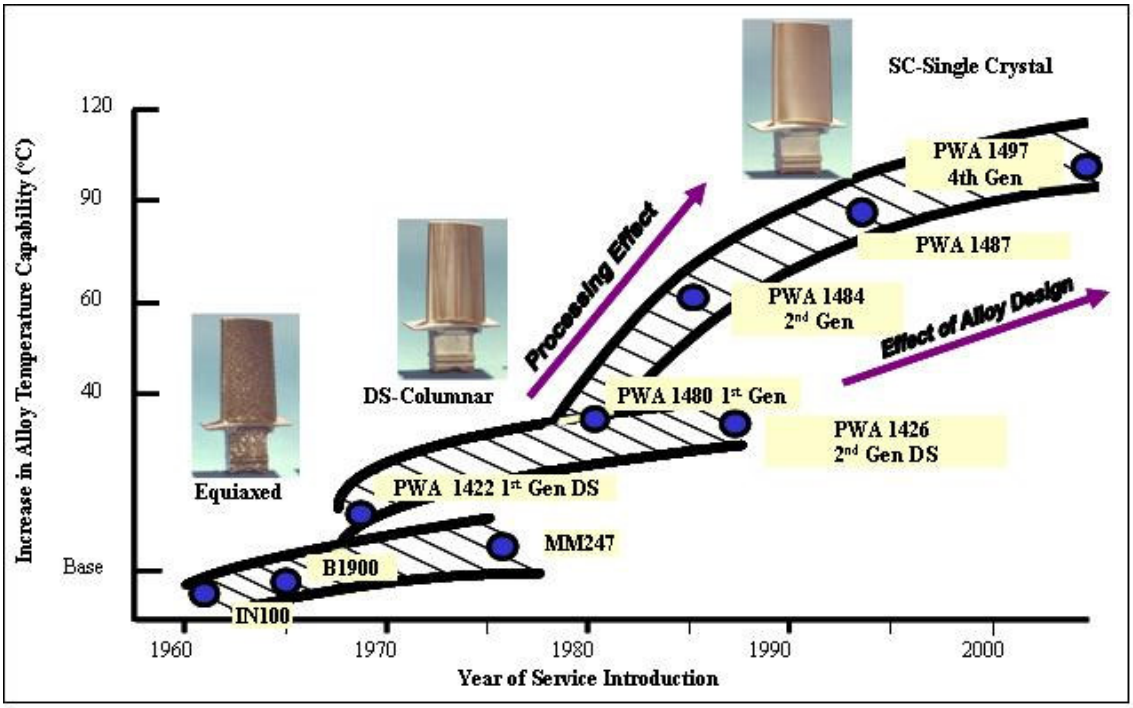

Fig. 3. Evolution of high strength Ni-base superalloys for turbine application (equiaxed to DS to SC) at Pratt & Whitney [1]

The development of SC superalloys resulted in fifth generations of these alloys. The fifth generation and even 6th is already under investigations [8, 9]. Compositions of the several examples of the 1st to 5th generations of SC alloys, are given in Table I.

Chemical composition of the earliest **first generation** of SC superalloys was based on those of conventional polycrystalline Ni-base superalloys. The grain boundary strengthening elements, such as C, B, Zr or Hf, were removed. Tantalum partially substitute W and Co content was maintained to increase solid solubility and microstructural stability [10]. The CMSX-2 and CMSX-3 single crystal superalloys were derived from Mar-M247, and CMSX6 from the alloy IN6212. René N4 was developed by General Electric and the alloys SRR99 and RR2000 were developed by Rolls-Royce in the United Kingdom [11]. PWA 1480, developed by Pratt & Whitney, was the first single crystal alloy specifically designed to be

used as a single crystal. Several alloy designers showed that a significant improvement of the creep strength of the single crystal superalloys may be obtained by the addition of rhenium. The introduction of 3 wt % Re to **second generation** of SC superalloys resulted in a temperature capability improvement of about 30 °C [11]. Rhenium partitions mainly to the γ matrix resulting in solid solution strengthening and also forming small clusters (~ 1nm), which act as efficient obstacles for dislocation motion, thus improving the alloy creep strength [10]. Reduction of Cr content from 8 to 5% and increased of Co (from 5 to 10%) in second generation SC superalloys minimizes the precipitation of brittle topologicaly close -packed (TCP) phases after long-time high temperature exposure [10]. Typical examples of this class of alloys are PWA1484, CMSX-4, René N5, SC180 and SMP14. The maximum application-temperature of second generation SC superalloys is about 1160ºC.

Table 1. Chemical composition of some 1 – 5 generations of SC superalloys (wt %) [1]

Alloy generation		Cr	Co	Mo	Re	Ru	W	Al	Ti	Ta	Nb	Hf	Others
1st	CMSX-2	8	4.6	0.6	-	-	8	5.6	1	6	-	-	
	CMSX-3	8	4.6	0.6	-	-	8	5.6	1	6	-	0.1	
	CMSX-6	9.8	5	3	-	-	-	4.8	4.7	2	-	0.1	
	PWA1480	10	5	-	-	-	4	5	1.5	12	-	-	
	AM1	7.8	6.5	2	-	-	5.7	5.2	1.1	7.9	-	-	
	René N4	9	8	2	-	-	6	3.7	4.2	4	0.5	-	
	SRR99	8	5	-	-	-	10	5.5	2.2	3	-	-	
2nd	CMSX-4	6.5	9	0.6	3	-	6	5.6	1	6.5	-	0.1	
	MC2	8	5	2	-	-	8	5	1.5	6	-	-	
	PWA1484	5	10	2	3	-	6	5.6	-	8.7	-	0.1	
	René N5	7	8	2	3	-	5	6.2	-	7	-	0.2	
	SC180	5	10	2	3	-	5	5.2	1	8.5	-	0.1	
	SMP14	4.8	8.1	1	3.9	-	7.6	5.4	-	7.2	1.4	-	
3rd	CMSX-10	2	3	0.4	6	-	5	5.7	0.2	8	0.1	0.03	
	René N6	4.7	12.5	1.4	5.4	-	6	5.75	-	7.2	-	0.15	0.05 C
	TMS 75	3	12	2	5	-	6	6	-	6	-	0.1	
	TMS 80	2.9	11.6	1.9	4.9	-	5.8	5.8	-	5.8	-	0.1	3 Ir
4th	PWA1497	2	16.5	2	5.95	3	6	5.55	-	8.25	-	0.15	
	TMS 138	2.9	5.9	2.9	4.9	2.0	5.9	5.9	-	5.6	-	0.1	
5th	TMS 162	2.9	5.8	3.9	4.9	6.0	5.8	5.8	-	5.6	-	0.1	
	TMS 173	2.8	5.6	2.8	6.9	5.0	5.6	5.6	-	5.6	-	0.1	

The **third generation** SC superalloys are characterized by increases in rhenium content to about 6% and relatively low chromium content (2 - 4%). More recent third generation SC alloys contain some additions of ruthenium or iridium [9] to reduce the tendency to form undesirable TCP phases. The results of creep testing [10] suggest that the functionality of 3rd generation of SC superalloys may be extended up to 1200 °C. However a new type of instability, called "secondary reaction zone" (SRZ) was observed by Walston in superalloys containing high Re contents [3]. Formation of cracks at the SRZ interfaces indeed induce premature failure leading to a life-time reduction of up to 70% [11]. The third generation SC superalloys includes CMSX-10 developed by Canon-Muskegon, Rene N6 developed by General Electric as well as Japanese alloys TMS75 and TMS80.

The efforts to develop the **fourth generation** SC alloy were focused on improvements of long-time creep strength and microstructural stability. It was achieved by significant composition changes from 2nd and 3rd generation single crystal superalloys. These included lower chromium levels, higher cobalt and rhenium levels and the addition of ruthenium. It was found that higher Co levels were beneficial in reducing both TCP precipitation and SRZ formation. Ruthenium caused the refractory elements to partition more strongly to the γ' phase, which resulted in better overall alloy stability [3]. Examples of fourth generation SX superalloys are PWA 1497 of Pratt &Whitney and Japanese alloy TMS-138 [12].

Fifth generation SC superalloys were developed in 2004 at the National Institute for Materials Science (NIMS) in Japan based on the 4th generation TMS-138 superalloy. These alloys, TMS-162 and TMS-173, contain higher total amounts of refractory elements, Nb, Ta, Mo, W and Re for strengthening. The Ru content was also increased to improve the phase stability [8, 9].

The development of new **sixth generation** SC superalloys is recently in progress at NIMS in Japan in the cooperation with Rolls-Royce. The aim in this generation is to reach 1150 °C temperature capability with better fatigue properties and oxidation resistance [13].

1.3. Evolution of the properties

The relative improvement of creep strength, thermomechanical fatigue resistance and oxidation resistance resulting from the transition from CC superalloys, to DS materials and then to 2nd generation of SC alloys are illustrated in Figure 4. Mechanical properties are

significantly improved by advances in casting technology and compositional design. Single crystal superalloy PWA 1480 offered 25 to 50 °C temperature capability improvement in terms of time-to-1% creep, compared to DS MAR-M 200 alloy [10]. Increased creep strength of 2nd generation PWA1484 alloy results from the increased Al and refractory element (Re + W + Mo) content compared to the 1st generation alloy PWA 1480. Thermomechanical fatigue life significantly increased (greater than 10 times life improvement) by reduced Young's modulus going from equiaxed-grain to <100> DS columnar-grained and SC superalloys. Oxidation resistance is a function of alloy composition and not casting processing mode. For example; the oxidation resistance of PWA 1484 is improved over PWA 1480 by increasing Al and reducing Ti and Cr contents.

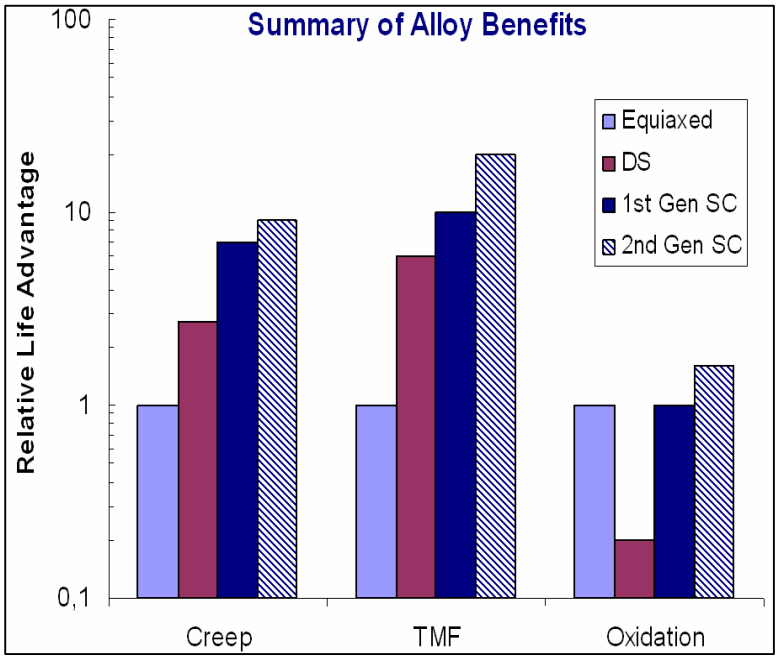

Fig. 4. The relative improvements of creep strength, thermomechanical fatigue resistance (TMF) and oxidation resistance of equiaxed, DS and SC (1st and 2nd generation) superalloys [1]

1.4. Technology and manufacturing

Early development on SC turbine airfoils was conducted at Pratt &Whitney in the mid-60's in parallel with the DS process. The first single crystal casts of nickel-base superalloys were produced in laboratory condition at Pratt &Whitney by Barry Piearcey who in 1970 patented the manufacturing technology [14].

According to R.C. Reed [4] there are three main advantages of SC over the CC and DS components:

a) Elimination of grain boundaries transverse to the principal tensile stress axis has reduced grain boundary cavitations and cracking, resulting in greatly enhanced creep ductility,

b) Elimination of grain boundaries strengthening elements, such as carbon and hafnium redundant. This has facilitated heat treatment and allowed for the further optimization of the alloy chemistry to increase of the high temperature capability,

c) The preferred <001> solidification crystallographic direction, which coincides with the minimum in Young's modulus and is oriented parallel to the component axis minimizes the thermal stresses developed on engine start-up and shut-down, this has dramatically improved the thermal fatigue resistance of the turbine hot gas path components.

The manufacturing of SC turbine blades is based on investment casting technology and starts from preparing a wax model of the particular blade. Single wax model are arranged in clusters by wax replicas of runners and risers, this enables several blades to be produced in a single casting process (Fig. 5).

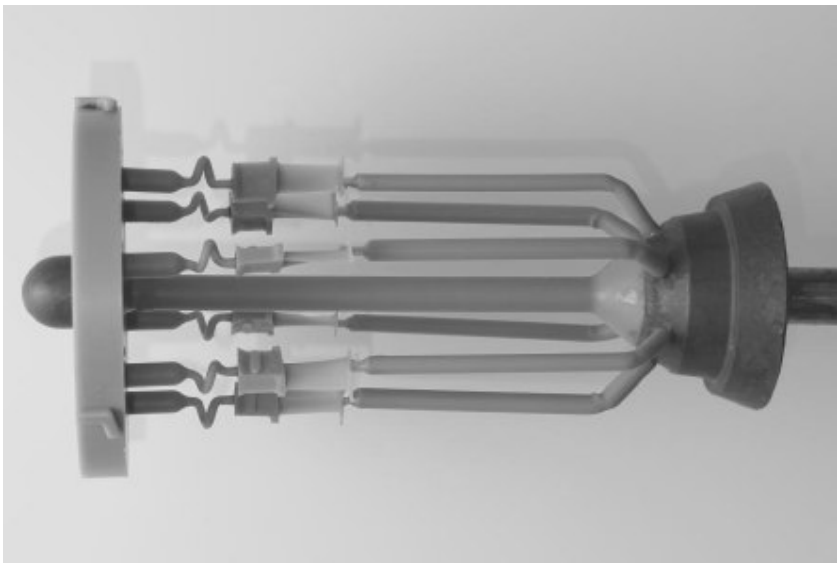

Fig. 5. Wax model of turbine blades (Onyszko et at. [15])

Further on an investment shell is produced by dipping the wax model into ceramic slurries consisting of binding agents and mixtures of zircon ($ZrSiO_4$), alumina (Al_2O_3) and silica (SiO_2), followed by powder with larger particles of these same materials. This operation is perform until the ceramic shell thickness reach adequate dimension, usually three or four times. After that, the ceramic shell is calcinated in multistage process to melt out the wax and build its strength (Fig. 6) [15].

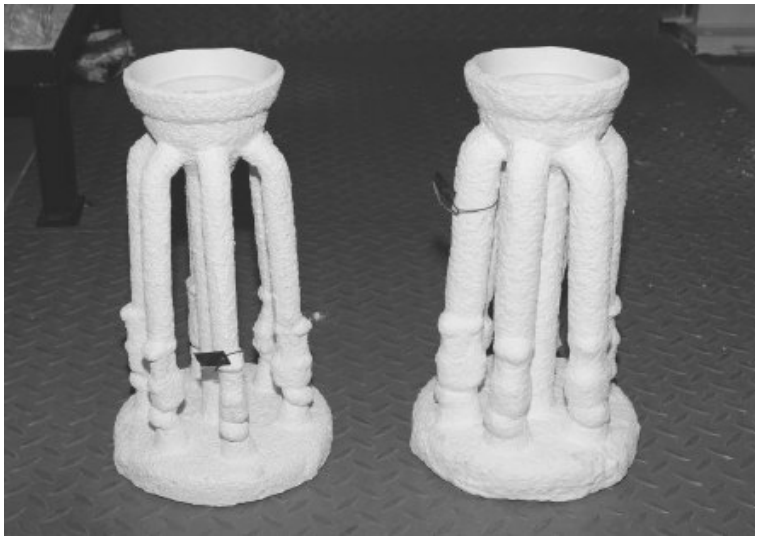

Fig. 6. Ceramic moulds for production the single crystal turbine blades (Onyszko et at [15])

Modern gas turbine applications require complex cooling passages. Hollow castings with complex internal features are made by first creating a ceramic positive replica of the internal hollow passage through injection of a ceramic slurry into a die cavity, forming a ceramic core. This core is then placed into the wax injection die, which contains the external pattern of the turbine blade, and then wax fills the die, encapsulating the core with wax. The result is a wax pattern that, at the wax interfaces with the air or the ceramic core, has the form desired for the finished part [5].

The next step before pouring in molten superalloy is to preheating and degassing of ceramic mould. The pouring process is perform under vacuum at temperature of ~1550 °C using a special vacuum furnace [16]. Maintaining proper crystallization conditions is the most difficult part of production. Crystallization process require carefully controlled mold temperature distributions to ensure transient heat transfer in one dimension only, to a water-

cooled chill plate. Grains are nucleated on the chill surface and grow in a columnar manner parallel to the unidirectional temperature gradient. The crystals have to pass through a narrow helical channel called the single crystal grain selector or “pigtail”, which only allows a few crystals to pass. As the metal solidifies from bottom to top, crystal elimination takes place so that only one crystal emerges from the selector into the bottom of the blade and start the single crystal structure of the airfoil. The single crystal casting processes is shown schematically in Fig. 7 [16].

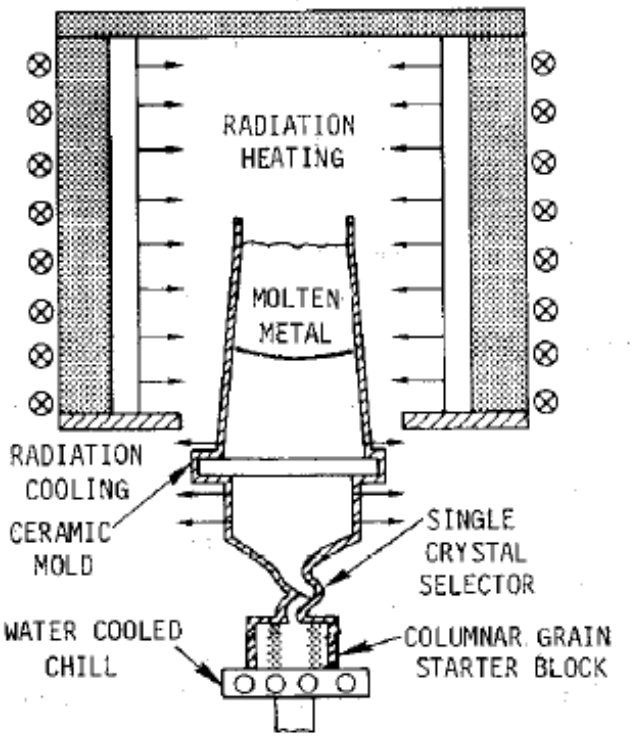

Fig. 7. Scheme of a single crystal casting process (Gell et at. [16])

The temperature gradient in the nucleation chamber is controlled by the chill, the molten metal superheat and the mold temperature is typically 1500 - 1600 °C. The high temperature prevent the nucleation of spurious grains during the pour, ahead of the advancing dendritic growth interfaces or on the mold surface. At the water cooled copper chill many grains are nucleated with essentially random orientations. Distribution of grain orientation and rocking curve analyses indicate that the <111> oriented grains are quickly overgrown by those with <110> and <100> orientations. The latter two orientations have similar growth

rates. It requires at least 2 cm of growth before more than 90% of all grains have orientation up to 15° of the <001> orientation. The single crystal grain selector has a circular cross-section instead of a series of ramps with a rectangular cross-section in order to minimize grain nucleation at sharp edges. After solidification is complete, the investment shell is removed and the blades can by separated from the cluster, Fig 8. [15, 16].

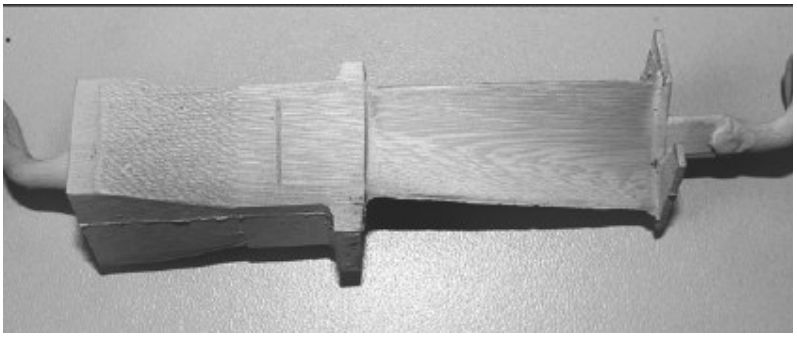

Fig 8. Turbine blade after removal of the investment shell (Onyszko et at. [15])

The turbine blades are finely machined to obtain a precise shape, and additional, tiny cooling holes are made by laser machining. The surface of the blades are usually coated with a ceramic thermal barrier coatings (TBC) to increase their thermal resistance.

1.5. Solidification and microstructure (as cast)

The blades obtained during single crystal solidification are described as being "single crystals" although they are still polycrystals, since they consist two phases: cuboidal γ' precipitates (fcc, ordered, L12) separated by narrow channels of γ matrix (fcc solid solution based on Ni) [*].

However, this terminology is widespread because of the fact that these two phases are coherent with ([001]||[001]) crystallographic relationship [1, 17].

Single crystal solidification of superalloys proceeds by dendrite growth. Each dendrite grows in three perpendicular <001> directions as a primary, secondary and tertiary dendrite arms. Microstructure within dendrite arms consists of cuboidal γ' precipitates, separated by narrow channels of γ matrix. In the interdendritic regions, eutectic γ-γ' areas with coarse

[*] Detailed description of the constituted phases is given in chapter II-2

irregular γ' particles are present [1, 17]. Figure 9 shows the dendritic structure of second generation CMSX-4 superalloy after solidification.

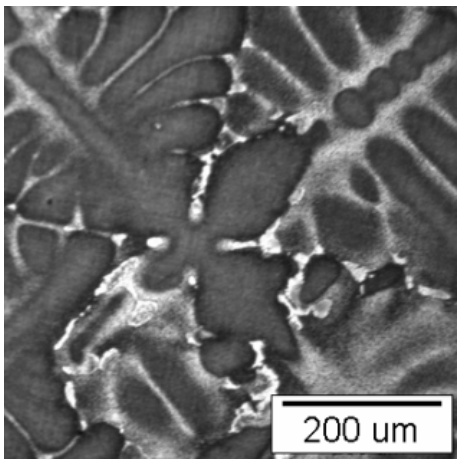

Fig. 9. Dendritic structure of as-cast 2nd generation CMSX-4 superalloy [1]

During solidification, some of the solute elements remain in the liquid phase while other elements diffuse to the solid phase. It has been established that Co, Cr, W, Mo and Re segregate preferentially to the dendrite cores, while Ti, Al and Ta segregate preferentially to the interdendritic regions [17]. The chemical heterogeneity in the solidified structure leads to instabilities. Dendrite cores, being rich in Cr and Re, are preferred precipitation of the brittle TCP phases that degrade both the creep and fatigue resistance of the alloy. Consequently, SC alloys after casting process are not suitable for application [18].

The quality of cast component depends on a number of parameters, including the temperature gradient at the liquid/solid interface, the velocity of the solidification front, and the spatial temperature distribution which determines the macroscopic shape of the interface. The melting and casting conditions must be closely controlled to obtain both a correct grain orientation and the absence of micropores or other grain defects at the dendrite boundaries [17].

Fortunately, the natural direction of dendritic growth in cubic crystals is <001> and that also corresponding to optimum creep strength. Maximum creep strength is obtained for orientations within 5° of <001> orientation, but in practice, deviations of up to 10° are tolerated [17].

1.6. Heat treatment and microstructure

In order to achieve alloy chemical homogeneity and eliminate microsegregation, solidified alloys undergo heat treatment (homogenization), which dissolves the γ' phase (both within the dendrites and interdendritic reggions). This heat treatment is performed isothermally or stepwise, between the γ' solvus and solidus temperatures (often referred as the 'solutioning window') and then is followed by fast cooling to the room temperature. To obtain the desired γ-γ' microstructure, the homogenization is followed by ageing treatment, below γ' solvus temperatures, where fine and uniform γ' particles are precipitated within the γ matrix. To obtain a bimodal distribution of γ' phase, two-step ageing is performed. The complete dissolution of eutectic γ' phase is difficult because of its coarse blocky morphology with a low surface area per volume ratio which makes it dissolve very slowly into the γ matrix [18]. Figure 10 shows the microstructure of fully heat treated PWA 1484 superalloy with a presence of residual eutectic islands as seen on image [1].

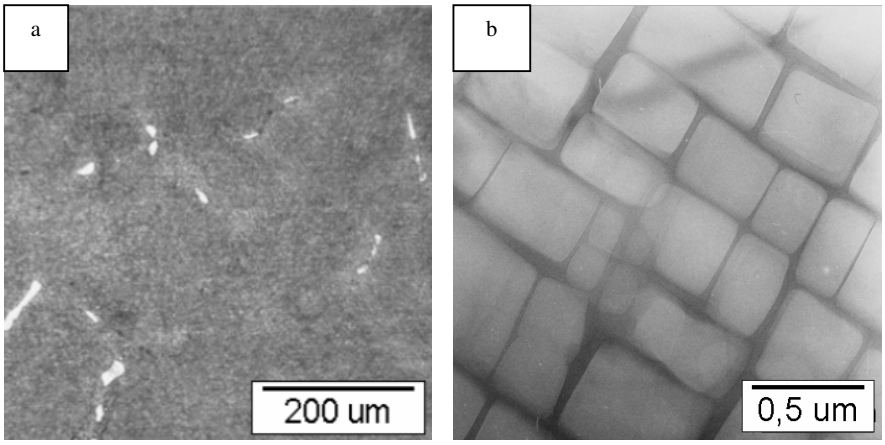

Fig. 10. Microstructure of fully heat treated PWA 1484 superalloy: a) LM, b) TEM images [1]

A highly segregated solidified microstructure may have a local solidus temperature in the interdendritic region significantly lower than the average solvus temperature within the dendrites. Under such a circumstance, a super-solvus homogenization leads to localized melting at the interdendritic region and complete solutionizing becomes almost impossible [18].

Recently it has been shown [18] that due to high degree of element segregation in the superalloys, a small fraction of liquid exists at the interdendritic region even below the

eutectic temperature (which is normally the lowest temperature at which liquid can exists in an alloys). It is also suggested that there is a possibility of up-hill diffusion in heavily alloyed superalloys during extended holding leading to incipient melting at the interdendritic region. Consequently, it is very difficult to predict the onset of incipient melting during the homogenization treatment of highly segregated superalloys. To overcome a problem of incipient melting, during homogenization, the superalloys are frequently heated in series of temperature steps. At each temperature step, the alloy is increasingly homogenized so that the tendency for incipient melting is minimized [18, 19].

To increase the high temperature capabilities, modern SC superalloys contain higher quantities of the refractory elements. In particular, the W, Re and Ta levels have been reported to increase steadily in each next generations of SC Ni-base superalloys. For example, a sum of the refractory metal (i.e. W, Mo, Re, Ta) content of representative first (CMSX-2), second (CMSX-4) and third generation (CMSX-10) alloys has increased from about 14 wt % to approx. 16.5 wt % and above 20 wt %, respectively. These increased refractory elements result in increased strength and creep resistance of the superalloy due to enhanced solid solution strengthening, precipitation strengthening by the γ' phase and slow diffusion rates. However, on the other hand, the microsegregation of these elements is more pronounced leading to higher eutectic fractions and greater chemical instability. The slow diffusion rates, affect also solution heat treatment. Therefore, recent generations of SC alloys require increased solution treatment conditions (temperature and time). Typical commercial heat treatment cycles for three generations of SC superalloys are presented in the Table 2 [18, 20].

Table 2. Typical solution heat treatment cycles for SC Ni-base superalloys [21]

Alloy	Refractory metal content W+Re+Mo+Ta (wt %)	Solution heat treatment
CMSX-2	14.6	1315 °C for 3 h/GFQ
CMSX-4	16.4	1276 °C for 2 h → 1287 °C for 2 h → 1296 °C for 3 h → 1304 °C for 3 h → 1315 °C for 2 h →1321 °C for 2 h → 1324 °C for 2 h/GFQ
CMSX-10	20.7	1315 °C for 1 h → 1329 °C for 2 h → 1335 °C for 2 h → 1340 °C for 2 h → 1346 °C for 2 h → 1352 °C for 3 h → 1357 °C for 3 h → 1360 °C for 5 h → 1363 °C for 10 h → 1365 °C for 15 h/GFQ

Where: GFQ – Gas (argon or helium) Furnace Quench

2. Constituent phases of single crystal nickel-base superalloys

2.1. Alloy elements and their microstructural effects

Single crystal (SC) superalloys contain a number of alloying elements, often greater than ten, and this is the reason why superalloys are considered as one of the most complex engineering materials. The chemical composition of some important nickel-based superalloys have been given already in Chapter 1.2 (see Table 1).

Superalloys contain a variety of elements in a large number of combinations to produce the desired effects. Table 3 presents the major alloying additions in Ni –base superalloys (SC) and their equivalent atomic radius, while Table 4 lists the role of some alloying elements in nickel-base superalloys [5].

Table. 3. Major alloying additions in SC Ni –base superalloys and their equivalent atomic radius [5, 22]

Element	Range, %	Atomic radius [Å]
Ni	bal.	1.243
Co	4 - 18	1.25
Cr	2 -10	1.25
Ru	0 - 6	1.322
Re	0 - 7	1.367
W	0 - 10	1.37
Mo	0 - 4	1.36
Nb	0 - 2	1.43
Ta	2 - 12	1.47
Al	3 - 6	1.43
Ti	0 - 5	1.46
Hf	0 - 0.2	1.58

Chromium and aluminum provide corrosion resistance and also strengthen the matrix, although aluminum partitions preferentially to the γ'. The most efficient matrix hardeners are the heavy elements, molybdenum and tungsten, together with niobium and tantalum not associated with the γ'. These elements diffuse slowly but unfortunately, the resulting increase in density is a major handicap for aeronautical applications [17]. Excessive amounts of chromium, molybdenum and tungsten promote the formation of so-called topologically close-packed (TCP) phases (σ, μ, or Laves phase). The TCP phases usually have low ductility (are

brittle) and cause loss of mechanical (and sometimes corrosion) properties when they are present in more than trace amounts [5].

Table. 4. The role of alloying elements in Ni-base superalloys [5, 17]

Effect *	**Nickel-base**
Solid solution strengtheners	Co, Cr, Fe, Mo, W, Ta, Re, Ru
MC	W, Ta, Ti, Mo, Nb, Hf
M_7C_3	Cr
$M_{23}C_6$	Cr, Mo, W
M_6C	Mo, W, Nb
γ' Ni_3(Al, Ti)	Al, Ti
Raises solvus temperature of γ'	Co
Hardening precipitates	Al, Ti, Nb
Oxidation resistance	Al, Cr, Y, La, Ce
Sulfidation resistance	Cr, Co, Si
Improves creep properties	B, Ta
Increases rupture strength	B **
Grain-boundary refiners	B, C, Zr, Hf
Retard γ' coarsening	Re, Ru
Promotes TCP phases	Cr, Mo, W, Re
* Not all these effects necessarily occur in a given alloy ** If present in large amount, borides are formed	

Because of this disastrous effect, overall contents of chromium, molybdenum and tungsten must be limited, despite their beneficial effect on oxidation resistance or creep strength [17]. Cobalt appears to have little direct influence on strengthening. Its atomic size is very similar to that of nickel and cobalt generally lowers stacking fault energy [17]. Moreover, cobalt raises the solidus temperature and also has been found to improve the resistance to TCP formation. Cobalt also reduces the formation of the secondary reaction zone (SRZ) beneath PtAl coatings [3]. The principal γ' forming elements are aluminum and titanium, and to a lesser degree niobium. Tantalum replaces titanium to a significant extent in SC superalloys, since it both strengths the γ' and raises the solidus temperature. Rhenium partitions mainly to the γ matrix resulting in solid solution strengthening and the formation of small clusters (~ 1 nm), which act as efficient obstacles for dislocation motion, thus improving the creep strength. On the other hand, higher amounts of rhenium may favour TCP phase formation [5, 1, 3]. The 4th generation and the latest of SC superalloys contain additions of ruthenium which cause "reverse partitioning" effect. This effect leads to the refractory elements

partitioning more strongly to the γ' phase. This is the reason why ruthenium improved the microstructural stability and allowed for higher levels of refractory elements to be added thereby improving high temperature strength of the superalloy [3].

Designing the chemical composition of superalloys is quite difficult; there are limits to the concentrations of alloying elements that can be added without inducing precipitation of undesired phases. It is particularly important to avoid TCP phase formation. There are no simple rules governing the critical concentrations and it is best to calculate or measure the appropriate part of the phase diagrams and balance the amount of alloying elements [5].

2.2. γ phase

The gamma phase (γ) is a solid solution with a fcc structure and $Fm\bar{3}m$ space group (Fig. 11) and a random distribution of the different kind of atoms. The total nickel content, for the γ phase is between 78 to 100 at. %.

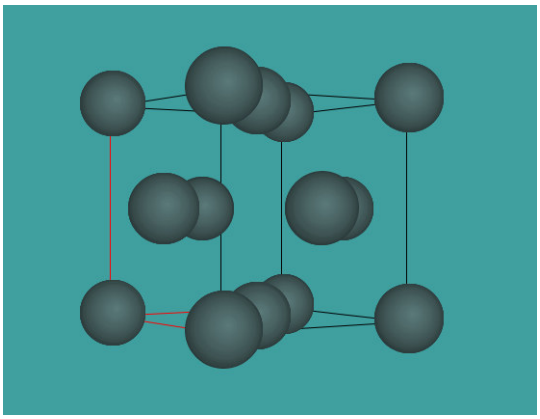

Fig. 11. The cubic unit cell of the γ phase ($Fm\bar{3}m$) crystal structure

In nearly all cases it forms a continuous, matrix phase in which the other phases are precipitated [4, 5]. Because of its electronic structure the fcc nickel lattice has a large solubility for many other elements. Solid solution strengthening is caused partly by lattice distortion, and therefore increases with atomic size difference, up to maximum of about 10%. The γ phase contains significant concentrations of cobalt, chromium, molybdenum, ruthenium and rhenium (if they are present in the alloy). High melting point elements provide strong lattice cohesion and reduce diffusion, particularly at high temperatures [17].

In superalloys the γ phase forms the matrix in which the γ' phase precipitates. Since both the phases have a cubic lattice with similar lattice parameters, the γ' precipitates are in a cube-cube orientation relationship with the γ [4, 5, 17].

2.3. γ' phase

The gamma prime phase (γ') Ni_3Al has a ordered cube structure ($L1_2$) and $Pm\bar{3}m$ space group. The total nickel content for the γ' phase, is between 73 to 76 at. %. In this structure the nickel atoms are at the face-centres and the aluminum or titanium atoms at the cube corners (Fig. 12). It is notable that each Ni atom has four Al and eight Ni as the nearest neighbours. This atomic arrangement has the chemical formula $Ni_3(Al,Ti)$. In addition to aluminum and titanium, also niobium, hafnium and tantalum partition preferentially into γ' [4, 5].

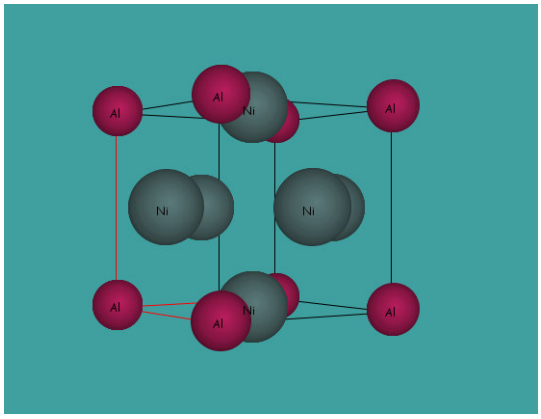

Fig. 12. The cubic unit cell of the γ' phase ($Pm\bar{3}m$) crystal structure

The γ' phase exists in SC superalloys as precipitates and is largely responsible for the high temperature strength of the material and resistance to creep deformation. The amount of γ' depends on the alloys chemical composition and temperature. For a given chemical composition, the volume fraction of γ' decreases as the temperature is increased [5,17].

2.3.1. Impact of γ' volume fraction

The volume fraction of γ' phase in modern SC superalloys is about 70 to 80%. This is apparently the optimum value, and is an essential factor for high creep strength. In the development of the superalloys, the volume fraction of γ' has steadily increased with time (Fig. 13) [17, 23].

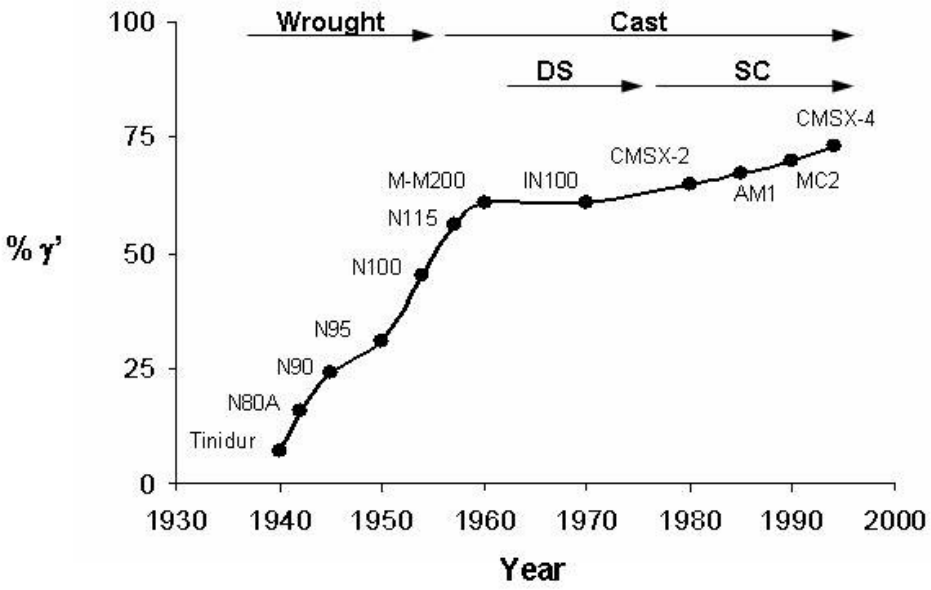

Fig. 13. Increase in the γ' volume fraction of superalloys and related processing development [17]

Across a wide range of temperature and level of applied stress, creep deformation on the microscale is restricted to the γ channels which separate the precipitates of γ' phase. Therefore, creep dislocations do not penetrate the γ' precipitates, so a reduced volume fraction of γ phase improves the creep properties. The optimum microstructure consists of high volume of fine γ'particles which are separated by very thin channels of the γ matrix [4]. This spatial packing leads to a strong strengthening effect from the γ/γ' interfaces, which impart resistance to creep deformation. This effect has been confirmed by measuring the creep life-time of alloys with identical chemical compositions, but heat treated to give different volume fractions of γ' precipitate [4, 23].

It should be mentioned that the creep performance does not increase monotonically as the γ' fraction is increased. Therefore there is a useful maximum, since further increases towards 100% of γ' precipitates lead to significant drop in superalloy strength [6, 23].
To find the optimum γ' volume fraction, γ and γ' forming elements are balanced but with a special care to maintain a sufficient "solutioning window" (ΔT), that is, a range of temperature below the solidus and in which γ is the only stable phase. This is necessary because, after solidification, heat treatment is required to remove residual microsegregation and γ-γ' eutectic rich in the γ' particles. This treatment dissolves the γ' precipitates, and then during ageing at lower temperatures, the γ' precipitate forms a uniform microstructure with an optimum precipitate size.

Since the solutioning window (ΔT) decreases as the γ' fraction is increased, the heat treatment of the higher-strength alloys can be difficult in practice. For third and fourth generation superalloys (which are rich in Re), the solutioning time is substantially longer than for first and second generation superalloys [4].

2.3.2. The role of γ/γ' misfit

Both the fcc γ matrix and the ordered γ' cuboidal precipitates in SC superalloys, have similar lattice parameters. The γ' precipitates are therefore often coherent with the matrix, with the {100} planes forming the interface. Nevertheless, there is usually a small difference in lattice parameter between the two phases; this is commonly called the "misfit" or "mismatch" [17].

The lattice misfit (δ), is defined as [4] :

$$\delta = \frac{2(a_{\gamma'} - a_{\gamma})}{a_{\gamma'} + a_{\gamma}}$$

where the lattice parameters of the γ and γ' phases (a_{γ} and $a_{\gamma'}$, respectively), depend on the elemental compositions in each phase and consequently on the extent of the γ/γ' partitioning effect [4]. The variation in the lattice parameter between each individual phase by the addition of substitutional alloying elements to pure nickel and pure Ni_3Al has been extensively studied. In particular, titanium and tantalum have been found to increase significantly the lattice parameters of both phases, whereas chromium has little effect [17].

The value of the misfit has been found to exhibit a significant effect on the morphology of the γ' precipitates. When the misfit is small, less than about +/− 0.2%, the γ' particles tend to occur as spheres, and for misfits in the range +/− 0.5 to 1% γ' precipitates are cuboids. The plate-like morphology is observed for misfits above +/− 1.25% [5, 24].

The misfit has a strong influence not only on the initial microstructure, but also on its evolution during high temperature creep deformation, when the directional coarsening known as rafting occurs. In a specimen subjected to mechanical stress, both phases experience external and internal stresses, and the lattice parameter will depend not only on the chemistry of each phase, but also on the local stress state [25].

It is commonly known that alloys with negative misfit possess greater creep resistance than those with positive misfit. This is because creep deformation is controlled by dislocation activity in the γ channels promoted by the externally applied tensile stresses, which are superimposed on the misfit stresses [4]. The different alloys display various lattice misfits. For example, it has been reported that in the SRR99 SC superalloy, the lattice parameters are $a_\gamma = 0.35887$ nm and $a_{\gamma'} = 0.35837$ nm at room temperature, which gives a misfit, $\delta = -1.4 \times 10^{-3}$ [4, 26]. Lattice misfit is strongly temperature dependent. Experiments using high temperature X-ray diffractometry indicate that the expansion coefficient of γ' is considerably lower than that of γ phase. Therefore, for all known SC superalloys, the lattice misfit becomes more negative as the temperature increases [4].

According to T. Suagi et al. [27] the SC superalloys with larger misfit display better creep resistance due to the effect of the coherent strain strengthening when the temperature is lower than 0.6 T_m. But when the temperature is higher than 0.6 T_m, the coarsening trend of the γ' phase in alloys increases due to the sufficient diffusion of the elements, which may result in the reduction of creep lifetime. The superalloys alloys with smaller misfit retain a smaller lattice strain at the γ/γ' interface, conferring a better creep resistance at high temperature due to the improvement of the microstructure stability [27].

2.4. Carbides and borides

Various types of carbides and borides appear in the superalloys, their type depending upon the alloy composition, processing conditions (specially heat treatment), as well as component operating conditions [4, 5].

Some of the more important types include MC, M_6C, $M_{23}C_6$, M_7C_3 and M_3B_2, where M stands for a metal atom such as Cr, Mo, Ti, Ta or Hf. Generally, MC is a high-temperature carbide, M_6C is intermediate in temperature of formation, and $M_{23}C_6$ and M_7C_3 are lower-temperature carbides [5]. In many superalloys the MC carbide, which is usually rich in Ti, Ta and/or Hf since these are strong carbide formers, precipitates at high temperatures from the liquid phase. Consequently, the carbide is often found in interdendritic regions with no distinct orientation relationship with the matrix [4].

Carbon and boron are often referred to as grain-boundary strengtheners. This is primarily due to the preferred location of carbides and borides at the γ grain boundaries, which has a strong effect in minimising grain-boundary sliding, resulting in an increase in rupture strength [4]. This explains why carbon and boron levels are generally higher in polycrystalline or DS superalloys, and why these elements are absent in the SC superalloys, in which grain-boundary strengthening is unnecessary [4].

The carbon content in SC superalloys is very low, so that carbides are rare. However, $M_{23}C_6$ type carbides have been reported in second generation CMSX-2 and AM1 alloys [28, 29]. They can be either blocky or elongated along preferential growth planes. Carbides of the η type, with the general formula $(Fe, Co, Ni)_3(W, Mo, Ta)_3C$, have been detected in MC2 alloy. This carbide occurs at fairly high concentrations of the heavy elements, Mo, W and Ta, and this is the reason why it forms more readily in MC2 than in other SC superalloys (see Table 1) [17].

2.5. Topologically-Closed-Packed phases

Topologically close-packed (TCP) phases are intermetallic compounds which can be found as precipitates in SC superalloys. They are generally brittle and detrimental to the mechanical properties of superalloys [4, 5, 17]. Usually, TCP phases are composed principally of the elements Ni, Cr, Mo, Co, W and Re, and unfortunately this list contains the elements which are most effective at conferring resistance to creep. The TCP phases are forming during exposure to conditions of high temperature and stress, if the concentration of the refractory elements are too large [30]. Precipitation of TCP phases during service depleting the matrix of refractory elements and reduce their solid strengthening effect. Moreover, TCP precipitates can delaminate in the fracture zone, and the precipitation of TCP

phases at high temperatures is frequently associated with the formation of voids which may potentially act as initiation sites for fracture [30, 31, 32].

The crystallographic structures of TCP phases have common features and no specific orientation relationship to the matrix. Table 5 summarizes the basic crystallography of the common TCP phases P, R, μ and σ [30]

Table 5. Crystallography of the TCP phases [30]

TCP phase	System	Space group	Space group No.	Atoms per unit cell
σ	Tetragonal	$P4_2/mnm$	136	30
P	Orthorhombic	Pa	62	56
μ	Rhombohedral	$R\bar{3}m$	166	13
R	Rhombohedral	$R\bar{3}$	148	53 (hex. 159)

At present, it appears that most modern SC superalloys (with high concentration of refractory elements) are thermodynamically unstable with respect to TCP phase formation [54]. Therefore several studies have been performed to overcome this problem. It has been found that platinum group metals are effective in controlling the precipitation of TCP phases. The growth rate of the TCP phase decreases with the addition of ruthenium. It has been proposed by A. Sato et al. [33] that the interface diffusion coefficient decreases with the addition of Ru [33].

3. High temperature microstructural stability of single crystal nickel-base superalloys during ageing, without external stresses

SC superalloys exposed at high temperature in the absence of external stress undergo microstructural changes. The γ' particles increase in size and change in morphology. The γ' cuboidal precipitates tend to group together in short chains or blocks of about ten particles, distributed fairly uniformly, which subsequently coalesce (Fig. 14). However, the slightest internal anisotropy tends to orientate the coalescence. This is probably caused by residual chemical gradients resulting from segregation during solidification. When the homogenizing treatment is prolonged to 50 h and more, this phenomenon completely disappears [17]. The mechanism which is responsible for this local directional coarsening behaviour is complex,

and can involve both the residual gradients in chemical potential and the internal stress fields associated with a slight variation of lattice parameters on the dendritic scale [17].

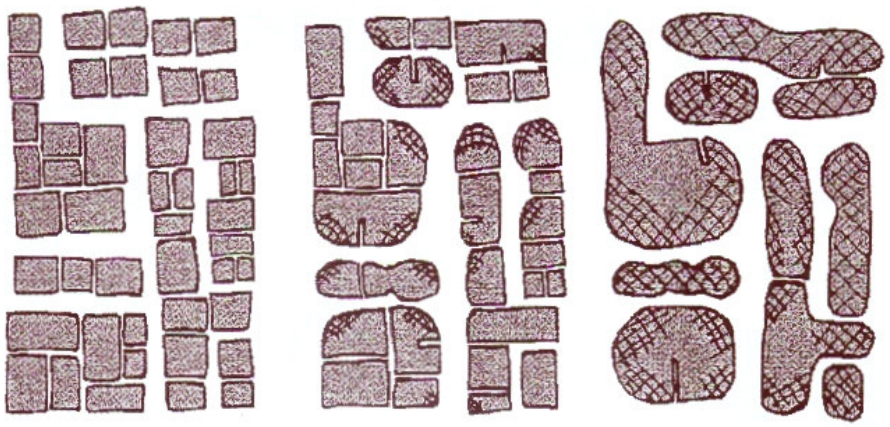

a) b) c)

Fig. 14. Schematic illustration of the formation of γ' platelets: a) Alignment of γ' particles to minimize misfit stresses, followed by coalescence to reduce interface area. This rearrangement widens certain matrix corridors, facilitating dislocation movement; b) Continued coalescence and formation of interfacial dislocation networks; c) Final coalescence and complete loss of coherence [17].

The dislocations often present at the particle/matrix interfaces also tend to orientate the coalescence. They have two effects, relaxing the stress anisotropy and establishing short-circuit diffusion paths [15].

4. Mechanisms of SC superalloys creep deformation

The deformation of SC superalloys is controlled by the activated dislocation movement within the solid solution γ and the interaction of dislocations with γ' precipitates [34]. The microstructural evolution during service and the deformation mechanisms are strongly connected with the strain and stress distributions at the γ/γ' interfaces and with the loss of coherency between the matrix and strengthening precipitates [35]. Depending on the temperature and applied stress, two primary creep mechanisms may be distinguished:

• creep involving shearing of γ' particles which occurs at high levels of applied stresses (about 700 MPa) and at temperatures close to the temperature of maximum γ' yield stress:

• high temperature creep involving the formation of equilibrium dislocation networks and rafting of γ' particles which occurs at about 1000 °C and at low stress levels: no shearing of γ' particles is found.

The creep curves of the second generation superalloy CM186LC (presented in Figure 15) show the typical shapes of the strain versus time curves for both creep mechanisms [36]. At low temperature/high stress (750 °C/675MPa), creep involves shearing of γ' particles and high primary creep strains arise due to frequent shearing of the γ' precipitates. At high temperature/low stress (950 °C/207MPa), creep involves rafting with a short primary stage and steady state represented by a plateau and pronounced strain appearing at tertiary stage.

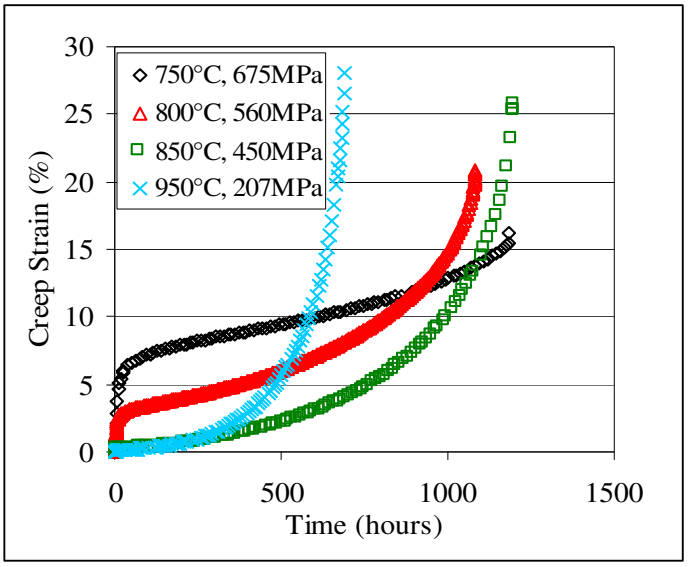

Fig. 15. Strain versus time curves of the second generation SC superalloy CM186LC showing the reduction in the primary creep with increase in temperature and reduction in stress [36]

5. Microstructural evolution during high temperature creep deformation (rafting)

A characteristic microstructural property of SC superalloys is the ability of cubic γ'phase particles to transform under the influence of stress and temperature into flat plates. This process of directional coarsening is usually called "rafting". Morphological changes in the two-phase microstructure are especially important in nickel-base superalloys due to their influence on creep resistance in the stress and temperature range experienced by turbine blades under service conditions. Two types of rafting behaviour in <001> oriented nickel-base single crystals have been identified:

1. N-rafts, which develope transverse to the direction of the externally applied stress,

2. P-rafts, which develope parallel to the direction of the externally applied stress.

Type N behaviour is usually associated with negative misfit alloys stressed in tension, or positive misfit alloys stressed in compression. Conversely, type P behaviour is associated with positive misfit alloys stressed in tension, and negative misfit alloys stressed in compression [37]. In the commonly used commercial nickel-base superalloys, lattice mismatch is negative, and an external stresses in tension produces a lamellar structure perpendicular to the [001] stress axis and an external stress in compression parallel to the stress [001] axis. Figure 16 shows the schematic diagram of rafting for an alloy with negative misfit.

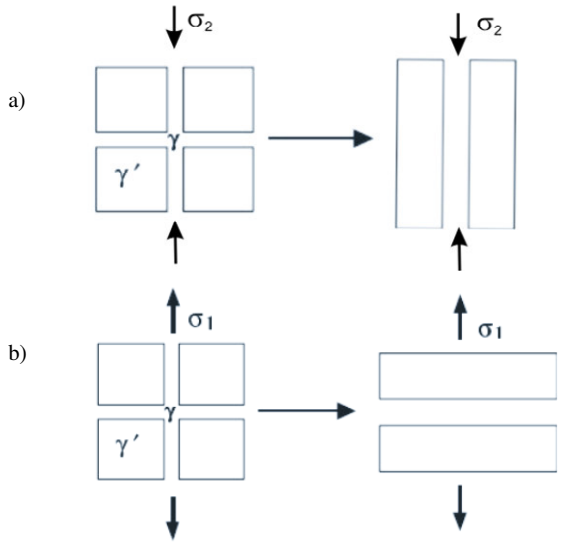

Fig. 16. Rafting process of a material with a negative γ/γ' misfit (δ<0) under stress a) compression (rafts parallel to the compressive axis), b) tensile (rafts perpendicular to the tensile axis) [1]

At elevated temperatures under uniaxial loading, the initially cubic-shaped precipitates evolve to plates, with the broad faces of the plates orientated normal to the axis of the applied tensile stress (Fig. 16 a) or parallel to the axis of the applied compressive test (Fig. 16 b).

In service the SC superalloys are subjected to uniaxial tension due to high centrifugal forces and most of the investigations are devoted to study the microstructural and mechanical aspects of these alloys under uniaxial test conditions. However, during service the SC superalloys components are not only subjected to uniaxial tension but also to a biaxial state of stress in some regions. These stresses are generated due to the thermal gradients in cooled regions, bending stresses exerted by the flowing gas and local stress concentrations. In these

circumstances, rafting in real components occurs under multiaxial state of stress [6]. Rafting occurs in all single crystal superalloys and becomes an essential factor in their high temperature creep strength. The rafts develop in the early stages of creep at high temperature (about 1000 °C) and low stress (about 100MPa). Rafting is observed under laboratory conditions as well under service conditions for turbines blades [38]. Concurrent with the rafting process, a thickening of the matrix channels parallel to the rafts occurs.

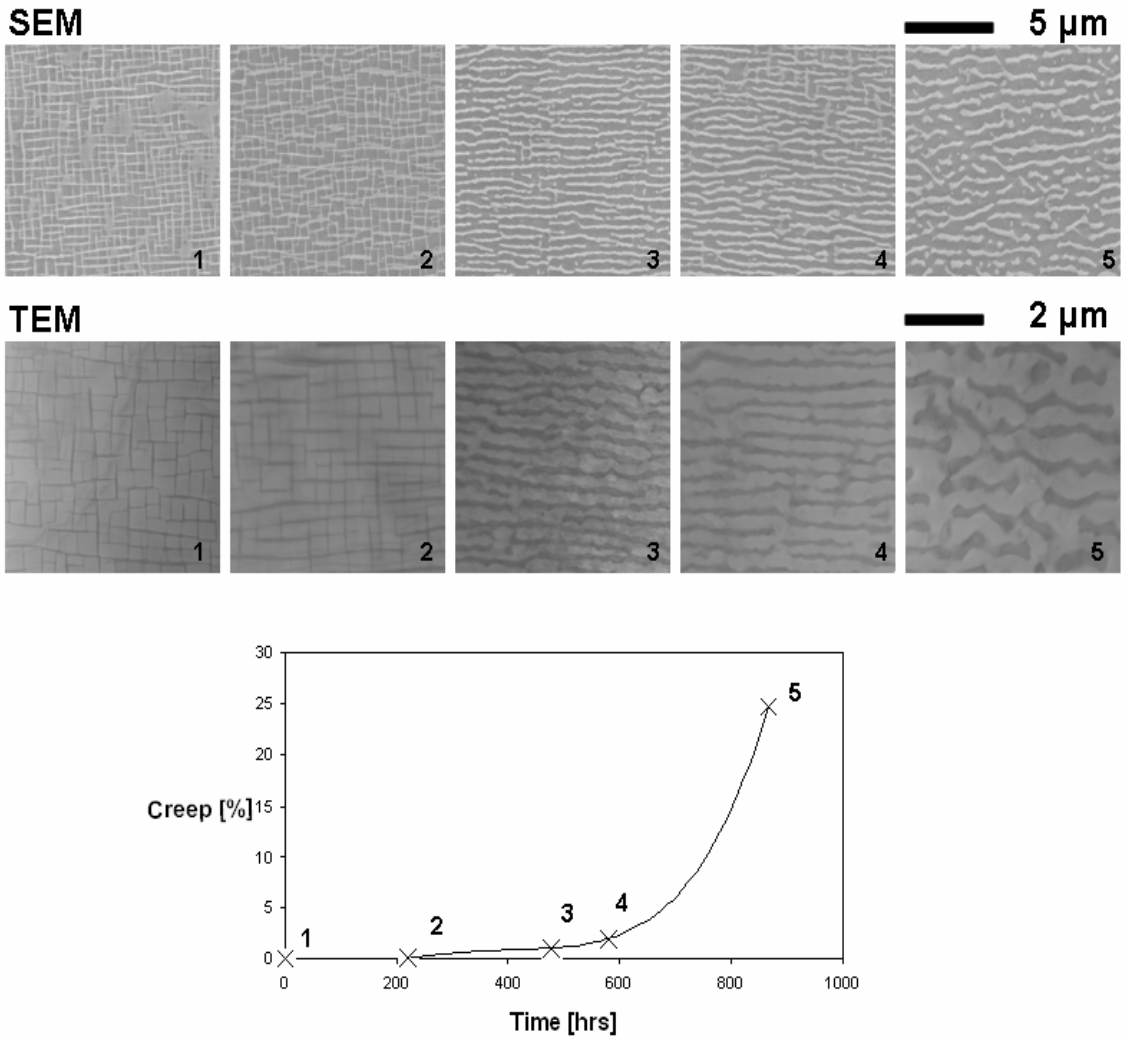

Fig. 17. SEM and TEM micrographs showing microstructural evolution of PWA1497 superalloy during high temperature creep deformation (982 ˚C and 248 MPa) with the corresponding creep curve [2].

Figure 17 shows the microstructural evolution of the fourth generation superalloy PWA1497 during high temperature creep deformation. The micrographs 17, 1 to 3 illustrate the development of γ' particules shape, from a cuboidal to a plate - like morphology, orientated perpendicular to the applied stress axis [2].

The evolution of a rafted structure leads to an effect called "topological inversion". This process is explained by Epishin et al [39]. During high temperature creep, the γ' phase coalesces, coarsens and finally surrounds the γ phase, thereby becoming topologically the matrix (Fig. 17, microstructures no 4 and 5). The beginning of this process starts when terminations of γ phase and finite γ' lamellae begin to occur. The formation of γ terminations as well as the formation of the finite γ' lamellae are evidently caused by the irregularity of the initial microstructure: the sizes of the γ' precipitates scatter considerably, their shape is often tetragonal and the habit planes deviate from {001}. Usually a row of γ' precipitates, well-aligned in the <001> direction, consists of 10-20 cuboids. Two typical configurations of the initial microstructure are given schematically in Fig. 18 [39].

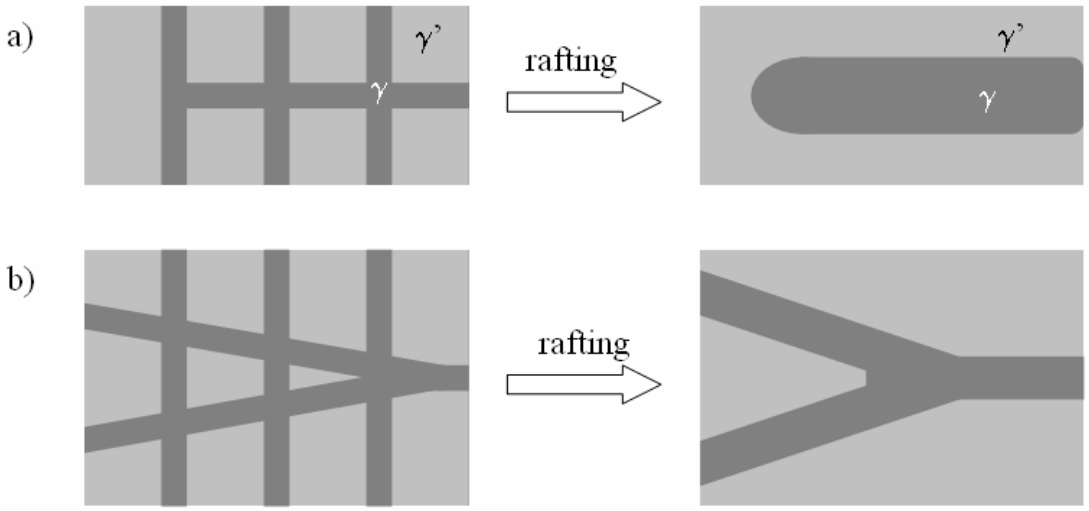

Fig. 18. Two typical configurations of the initial microstructure leading to the formation of γ and γ' terminations: a) formation of a γ termination, b) formation of a γ' termination [39]

The topological inversion is explained by the formation of junctions connecting neighbouring γ' rafts and separating the γ phase, as schematically shown in Figure 19. The

junctions are generated by the surface diffusion of γ'-forming elements moving along the interface towards dislocation concentrations in the γ phase. At the final step of the process, γ' phase becomes topologically the matrix surrounding the γ phase. The transformation of long γ lamellae into short inclusions leads to an increase in dislocation motion in γ' phase. Moreover, the isolation of the γ phase is not complete, still making dislocation climb possible. Therefore topological inversion of the γ-γ' microstructure is accompanied by a drastic increase in the creep rate. [39].

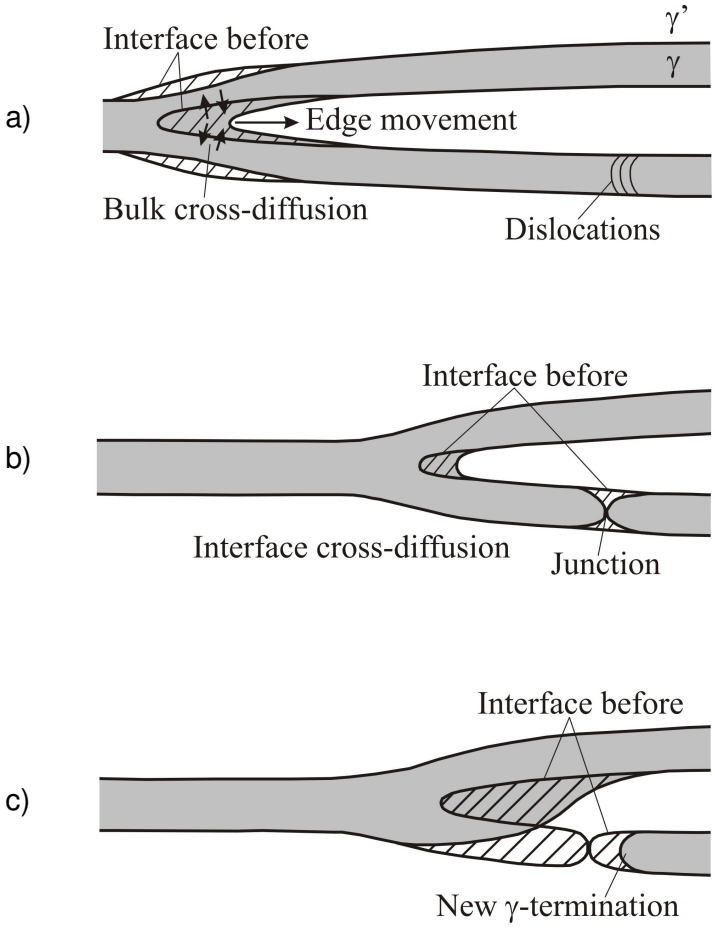

Fig. 19. Steps in the coarsening of the raft microstructure: a) thickening of the γ and γ' lamellae due to dissolution of a γ' edge controlled by bulk diffusion through the γ phase, b) nucleation of a γ' junction, c) growth of the γ' junction resulting in the formation of a γ' termination [39].

III. EXPERIMENTAL PROCEDURE

1. Materials investigated

Two nickel-base SC superalloys were investigated:

- PWA 1484, a typical second generation single crystal superalloy
- PWA 1497, new fourth generation single crystal superalloy

Both PWA 1484 and PWA 1497 superalloys were solidified into single crystal bars and provided by Pratt & Whitney, US. Bars with orientations within 5° of the <001> casting direction were selected for mechanical testing to minimize the effect of orientation on the results.

1.1 Chemical composition and heat treatment

The chemical compositions of the two "as – received" superalloys are presented in Table 6.

Table 6. Chemical compositions of the PWA 1484 and the PWA 1497 alloys (Ni-bal., wt %)

Alloy	Cr	Co	Mo	Re	Ru	W	Al	Ta	Hf
PWA 1484	5	10	2	3	-	6	5.6	8.7	0.1
PWA 1497	2	16.5	2	5.95	3	6	5.55	8.25	0.15

The solid bars of the PWA 1484 and PWA 1497 superalloys were subjected to the customary heat treatment, involving solution annealing followed by ageing. The heat treatment condition for both superalloys are confidential and protected by the patent law. It cannot be disclosed without Pratt & Whitney permission.

2. Creep tests

All creep tests were performed by the Institute of Aviation in Warszawa.

2.1. Geometry of the specimens

All specimens used for creep tests were delivered by Pratt & Whitney. They were machined with preservation of <001> crystallographic orientation along sample axis. The geometry of the specimens is given on Fig. 20.

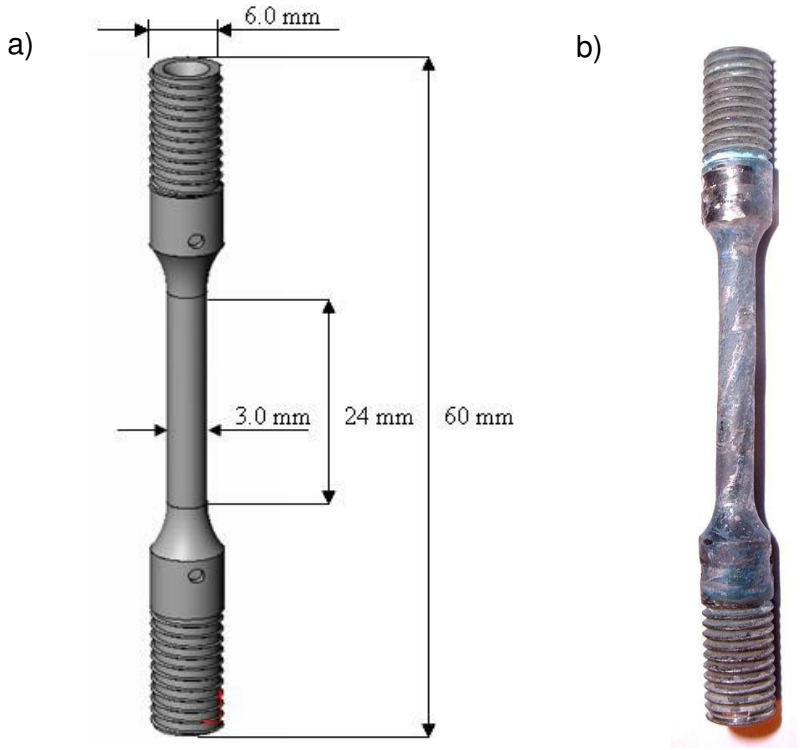

Fig. 20. Creep specimen: a) geometry of the specimen, b) after creep test

2.2. Creep conditions

Twenty two specimens (10 of the PWA 1484 and 12 of the PWA 1497) were creep tested at the same temperature 982 ºC (1800 ºF) and various strain and stress conditions. The creep conditions for both alloys are given in Tables 7 and 8. For both alloys two groups of stresses can be distinguished. Five specimens of PWA 1484 superalloy were creep tested at constant load of 193 MPa (23 ksi) and five at 248 MPa (36 ksi). For the PWA 1497 superalloy six specimens were creep tested at constant load of 248 MPa (36 ksi) and six at 310 MPa (45 ksi). All creep tests were terminated after systematically increasing strain (excluding two samples of PWA 1484 and four of PWA 1497 superalloy which were creep tested until rupture) and the specimens were rapidly cooled under load.

Table 7. Creep test conditions of second generation superalloy, PWA 1484

No	Temperature		Stress		Run to	Creep strain [%]	Duration [h]
	[°C]	[°F]	[MPa]	[ksi]			
8	982	1800	193	28	0.5 %	0.629	264.3
9	982	1800	193	28	1.0 %	1.002	473.9
10	982	1800	193	28	2.0 %	2.522	596.6
4	982	1800	193	28	rupture	28.762	898.6
3	982	1800	193	28	rupture	29.758	971.2
5	982	1800	248	36	0.5 %	0.714	69.7
6	982	1800	248	36	1.0 %	1.465	139.4
7	982	1800	248	36	2.0 %	2.223	141.5
2	982	1800	248	36	rupture	25.633	280.7
1	982	1800	248	36	rupture	11.43	289.1

Table 8. Creep test conditions of fourth generation superalloy, PWA 1497

No	Temperature		Stress		Run to	Creep strain [%]	Duration [h]
	[°C]	[°F]	[MPa]	[ksi]			
8	982	1800	248	36	0.05 %	0.055	1.58
9	982	1800	248	36	0.1 %	0.079	219.58
10	982	1800	248	36	0.5 %	0.843	477.17
11	982	1800	248	36	1 %	1.05	477.45
12	982	1800	248	36	2.0 %	1.976	580.18
2	982	1800	248	36	rupture	24.793	867.41
4	982	1800	310	45	0.05 %	0.066	17.11
6	982	1800	310	45	0.1 %	0.06 + 0.05 *	2.47 + 37.14 *
5	982	1800	310	45	0.5 %	0.543	138.06
7	982	1800	310	45	1 %	0.9765	167.1
3	982	1800	310	45	2.0 %	2.008	190.02
1	982	1800	310	45	rupture	24.808	285.05

***** Specimen number 6 slipped out from the grips, creep test was continued after readjustment

3. Specimens preparation for structure and surface investigation

All samples were prepared and treated in the same manner to minimize the influence of sample preparation on the results of investigation. Fig. 22 shows the way of basic sample preparation (cutting) for further XRD, LM, SEM, TEM and AFM investigation. All samples were cut into small pieces with special care to obtain the same crystallographic orientations, (010) or (100). To set the same orientation of the samples, cutting was performed along the axis of primary dendrite arms x or y, as revealed by etching with a γ'- dissolving agent (25ml ethanol + 25 ml HNO_3 + 27ml HCl), see Fig. 23.

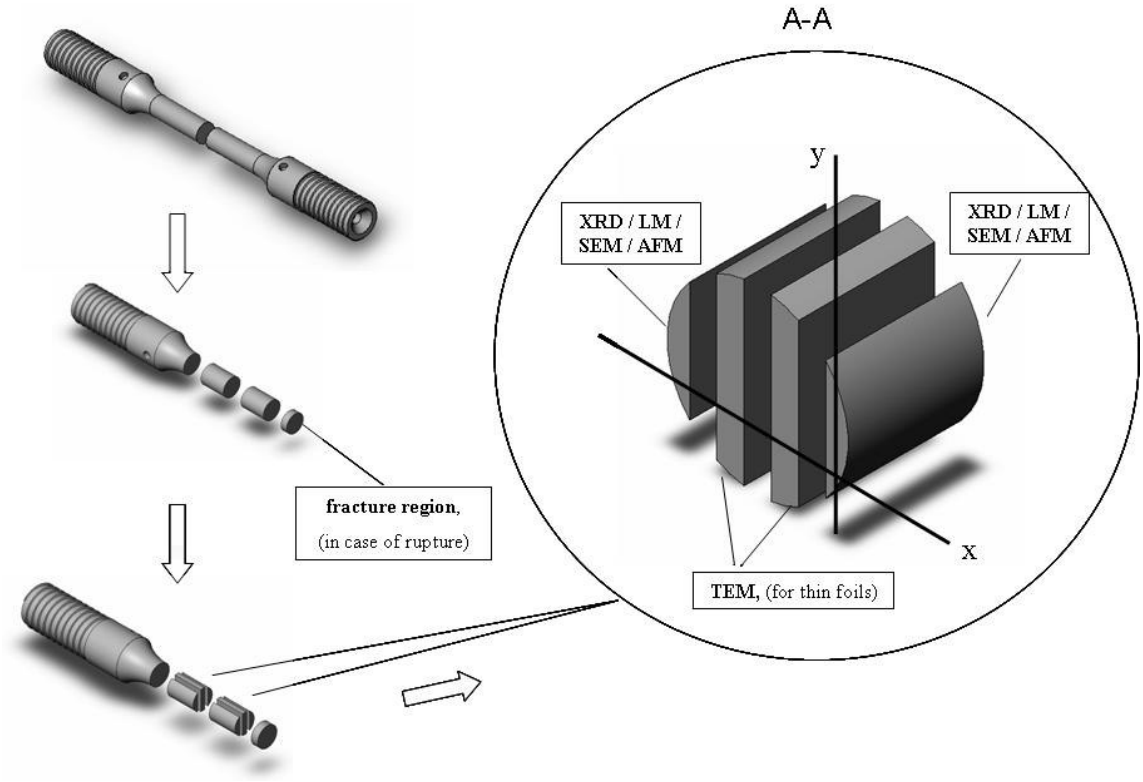

Fig. 22. Basic sample preparation for XRD, LM, SEM, TEM and AFM investigation

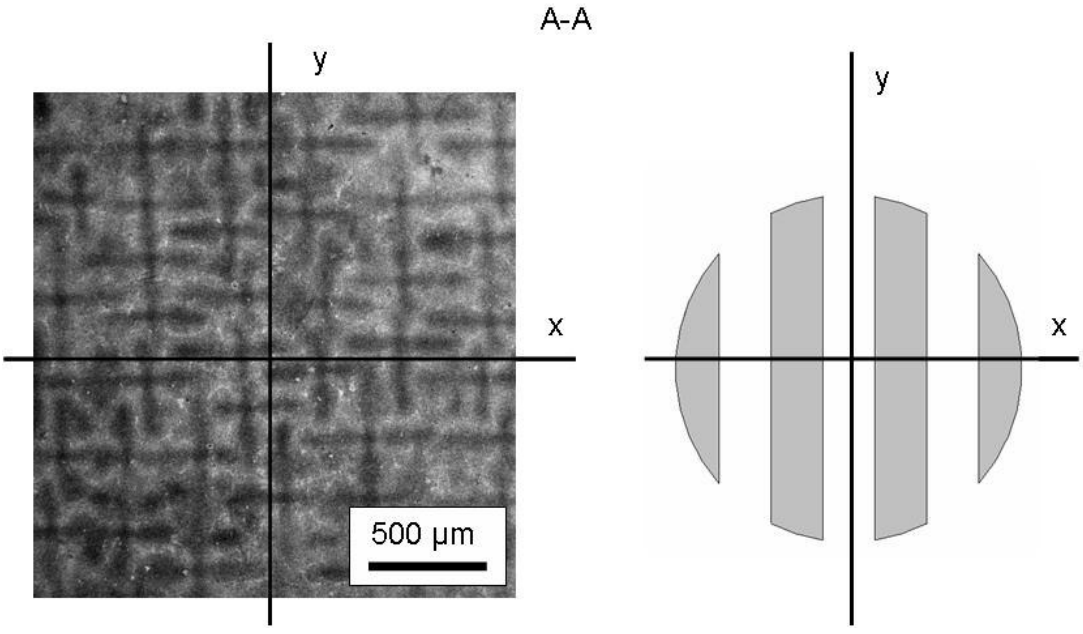

Fig. 23. Determination of sample cutting. Cross-section of the PWA 1484 superalloy sample; LM micrograph showing primary dendrite arms axis.

4. X-ray diffractometry

The X-ray diffractometry (XRD) measurements consisted of crystallographic orientation and γ/γ' misfit measurements. The samples were prepared from the test piece cross-sections (perpendicular to the crystallization axis), cut with low-speed diamond saw. The surfaces of the samples were mechanically polished with diamond and silica suspended solids.

The XRD measurements of crystallographic orientation were performed on as-received samples of the PWA 1484 and the PWA 1497 superalloys, to establish disorientation angle from (001) plane. The XRD investigation was carried out using TuR M60 apparatus with Co X-ray tube and continuous spectrum and measurements were made using the back-reflection Laue method. The distance between sample and film was 30 mm.

The results were obtained with the assistance of LAUE non-commercial computer software [40] and show the orientation of single crystals (hkl) planes and <uvw> directions as well as disorientation angle from (001) plane.

The XRD measurements of γ/γ' misfit were performed on selected samples including two samples from the as-received materials (one for each generation of the superalloys) and two samples after creep rupture, with the highest creep exposure time and strain (one for each superalloy generation).

The XRD investigation was carried out using D500 SIEMENS apparatus with Cu X-ray tube and monochromatic radiation obtained by graphite crystal monochromator. The lattice spacings a_γ and $a_{\gamma'}$ were determined from the positions of the $K\alpha_1$ peaks and the γ/γ' lattice misfit was calculated as $\delta = 2 \times (a_{\gamma'} - a_\gamma)/(a_{\gamma'} + a_\gamma)$. The resulting diffraction patterns were analysed with MAKRO 50 non-commercial computer software [41]. Fitting was made by the least squares method applied to the Lorentz function.

5. Light microscopy

LM investigation was performed on each sample of the PWA 1484 and the PWA 1497 superalloy to establish dendrite arm orientation for further SEM and TEM samples preparation, as well as on baseline samples to reveal the presence of remaining dendritic microstructure and γ-γ' eutectic.

LM specimen preparation included low-speed diamond saw cutting, mechanical polishing with diamond and silica suspended solids. To reveal details of the microstructure, chemical

etching in solution of a γ'- dissolving agent: 25ml ethanol + 25 ml HNO_3 + 27ml HCl at room temperature was performed.

LM microstructural examination was carried out using an OPTECH Model XJL-17, and AXIO Imager M1m of Zeiss microscopes.

6. Scanning electron microscopy

SEM investigation was performed on each sample of the PWA 1484 and the PWA 1497 superalloys. This technique was used to investigate microstructural changes of the γ and γ' phases caused by creep deformation under the various conditions.

The specimen preparation for SEM investigation was the same as for LM investigation. SEM microstructural examination was carried out using a CAMBRIDGE STEREOSCAN 120 microscope operating at 30 kV and SEM / FIB NEON 40EsB CrossBeam of Zeiss operating at 30 kV.

7. Transmission electron microscopy

TEM investigation was performed on each sample of the two alloys (PWA 1484 and PWA 1497). This technique was used to analyse microstructural changes in γ and γ' phases caused by creep deformation under the various conditions.

TEM specimen preparation included the following operations:

- low-speed diamond saw cutting,
- mechanical pre-thinning with sandpaper (remaining thickness 75 μm),
- dimpling (remaining thickness 45 μm)
- electrochemical polishing using double-jet Struers TenuPol 3, solution: 450 ml $CH_2OHCH_2OC_4H_9$ + 450 ml CH_3COOH + 100 ml $HCLO_4$, process parameters were: temperature -4 °C, voltage 26V

TEM microstructural examination was carried out using a JEOL JEM-200CX and JEM-2010 ARP transmission electron microscopes operating at 200 kV.

Selected area electron diffraction (SAED) was performed for phase analysis. Indexing of SAED diffraction patterns was made by means of JEMS software [42].

8. Nanoindentation hardness measurements by Atomic Force Microscopye*

In the recent years, the nanoindentation in AFM (NI-AFM) technique has become a valuable tool for materials science. The application of this technique is especially promising for precipitate-hardening materials with the precipitate sizes below 1 μm, e.g. for Ni-base superalloys. This technique has been described in Refs [43-47].

The NI-AFM technique was used for quantitative measurements of nanohardness of the γ and γ' phase. Investigation was performed on selected samples of the PWA the 1484 and the PWA 1497 superalloys, as described in Table 9.

Table 9. Samples of the PWA 1484 and the PWA 1497 superalloys, selected for NI-AFM investigation

PWA 1484 superalloy					PWA 1497 superalloy				
Creep samples conditions					Creep samples conditions				
No	Temp. [°C]	Stress [MPa]	Strain [%]	Time [h]	No	Temp. [°C]	Stress [MPa]	Strain [%]	Time [h]
BM#	-	-	-	-	BM#	-	-	-	-
5	982	248	0.714	69.7	8	982	248	0.05	1.58
6	982	248	1.465	139.4	10	982	248	0.849	477.17
2	982	248	25.633	280.7	2	982	248	24.793	867.41

Baseline material

Sample preparation for NI-AFM technique included low-speed diamond saw cutting, and two-stage polishing; first standard mechanical polishing by using diamond suspended solids and final chemo-mechanical polishing with 0.125 μm silica suspended solids. Final chemo-mechanical polishing allows a smooth surface to be produced, with a small height difference between γ and γ' phases in superalloys, which produces contrast in AFM.

The NI-AFM examination were carried out at room temperature using a Veeco Instruments Multimode atomic force microscope equipped with an add-on Triboscope force transducer from Hysitron. The transducer, mounted on a conventional AFM, controls the z-movement of the tip and measures the indentation force. In all indentation experiments a diamond cube corner tip (three sided pyramid) with a tip angle of 90° was used. The same diamond tip was used to image the topography of a surface of the samples. All indentations in the γ matrix phase (in the initial microstructures of both superalloys γ matrix channels are very narrow) were performed in the cross-section of matrix channels lying perpendicular to the surface of the samples.

* Atomic Force Microscopy (AFM) investigations were carried out during my research stay on the Department of Materials Science and Engineering of the University Erlangen-Nuremberg.

The hardness (H) was derived from the nanoindentation experiments by evaluation of the load displacement curve according to the Oliver Pharr method [46]. The hardness H is calculated from $H = P_{max}/A_c$ equation, where P_{max} is the maximum force during indentation and A_c the projected contact area. The maximum force during indentation P_{max} was kept constant at 250 μN. To secure proper statistics, ten measurements were performed for each phase (γ or γ') in each sample. Schematic IN-AFM technique is shown on Fig. 24 [47].

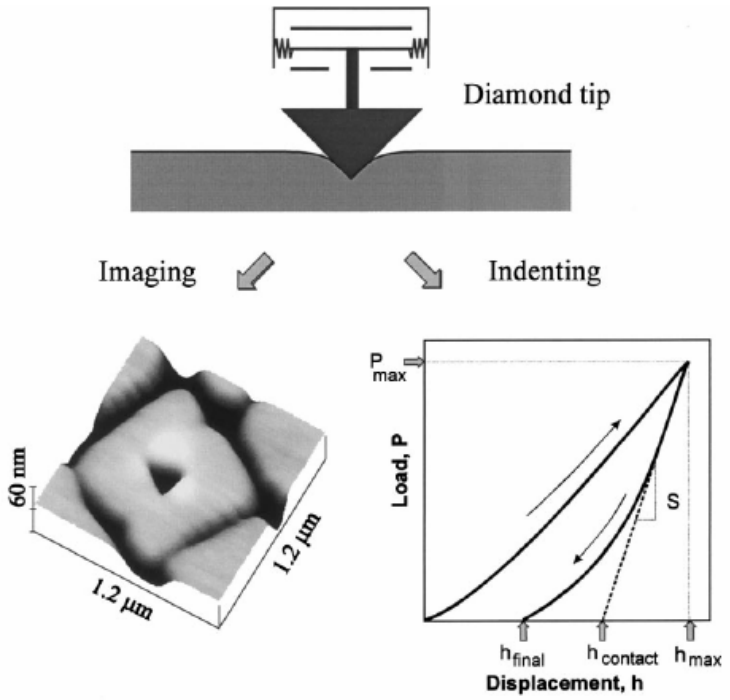

Fig. 24. Schematic representation of the nanoindentation process (NI-AFM). First the sample surface is imaged in AFM contact mode with a diamond tip, where positions for the indents are selected. After that the load-displacement curve is recorded during indenting the surface with the same diamond tip. A second AFM image from the surface then reveals the plastic indent [47]

9. Image analysis

Quantitative image analysis of the SEM and TEM micrographs was made by means of commercial image analysis software "AnalySIS 3.2" [48].

9.1. Stereological procedure for characterization of baseline materials

Both superalloys (baseline materials) were examined in the same manner. Only γ' particles from primary and secondary dendrite arms were taken for quantification; to secure proper statistics more than 300 particles of γ' phase were quantified.

For quantitative description of baseline materials microstructure the following parameters were used:

f_s - surface fraction of γ' particles

V_v - volume fraction of γ' particles ($V_v \cong f_s$)

D - mean size of γ' particles, see Fig. 25

k - shape coefficient, see Fig. 26

S - mean width of γ phase (channels)

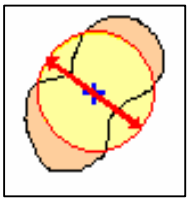

Fig. 25. Parameter **D** - the mean size of γ' particles is calculated as ECD - Equivalent Circle Diameter; the equivalence refers to the area of the particle. The ECD is the diameter of a circle that has an area equal to the area of the particle [48]

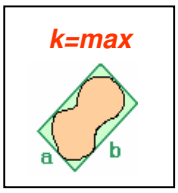

Fig. 26. Parameter **k** - the shape coefficient is calculated as the maximum ratio of width and height of a bounding rectangle for the particle [48]

Schematic procedure of γ' particles detection is given on the Fig. 27. Binarization of TEM micrographs was made manually to overcome problems with differences of grey values on the micrograph (differences in grey values were caused by the differences in the thin foil thickness). Manual binarization in this case was more accurate than an automatic method. Only complete γ' particles were taken into account, particles truncated by micrograph border were excluded.

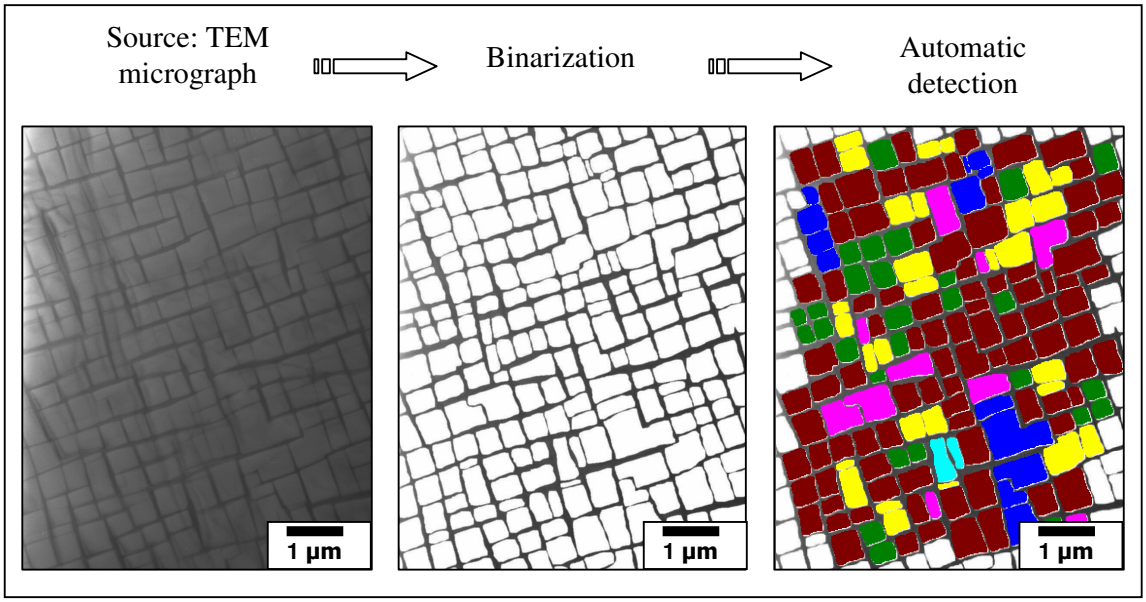

Fig. 27. Schematic procedure of γ' particles detection for stereological procedure

9.2. Stereological procedure for characterization the degree of rafting

Both superalloys after creep deformation were examined in the same manner. Only γ' particles from dendrite areas were taken for quantification. The intersection of grid lines and γ/γ' interfaces was used to define a number of stereological parameters. Those included: **T** and **S**, which represent the mean linear length of γ' phase in directions parallel to the tensile axis and the mean γ interlamellar spacing along the tensile axis respectively [49]. The determination of these parameters was based on TEM micrographs. The grid periodicity chosen for measurement was 0.08 μm (about five times the pixel size). Only complete γ channels and γ' particles, were taken into account. Channels and particles truncated by micrograph borders were excluded. Schematic procedure of **T** and **S** parameters determination is shown on Fig. 28.

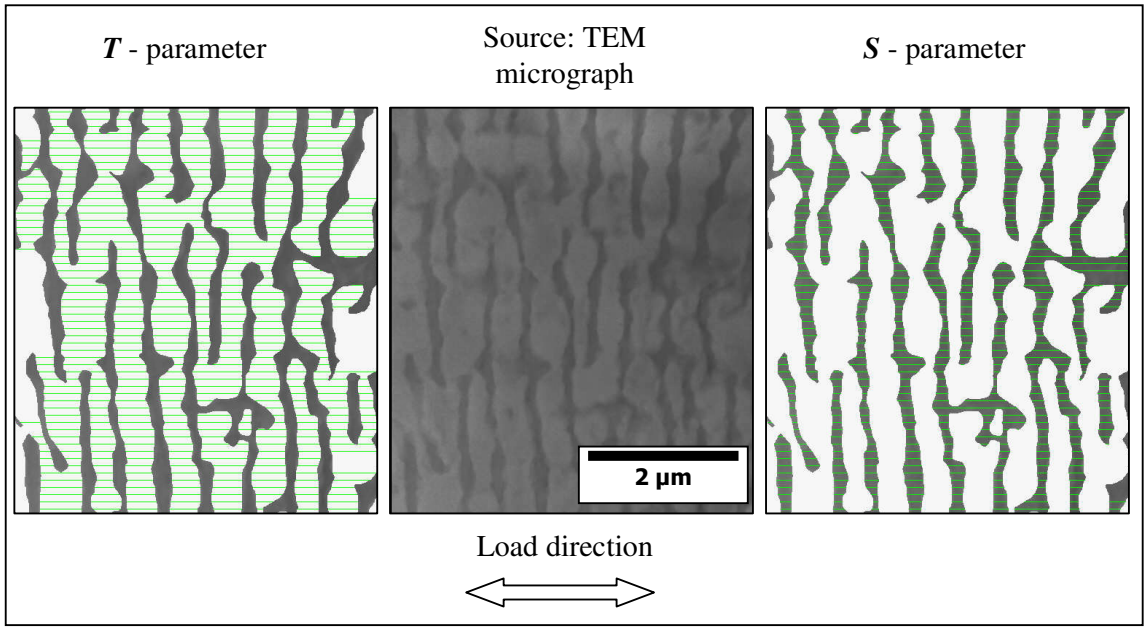

Fig. 28. Schematic procedure for the **T** and **S** parameters determination

The SEM technique, which allows analysis of a significantly larger area, was used to determine the **L** parameter which represents the mean length of γ/γ' interface boundary in directions normal to the tensile axis. **L** is the distance between ± 180º bends of the continuous γ/γ' interfaces. This distance represents the path that a dislocation has to climb during deformation and was measured by analysis of the γ/γ' interface pieces distinguished by the one-side gradient filtering [50].

Filtering process was made using up and down gradient filters, with matrix formula:

$$\text{up} \quad \begin{vmatrix} 0 & 1 & 0 \\ 0 & 0 & 0 \\ 0 & -1 & 0 \end{vmatrix} \qquad \text{down} \quad \begin{vmatrix} 0 & -1 & 0 \\ 0 & 0 & 0 \\ 0 & 1 & 0 \end{vmatrix}$$

Fig. 29 shows the image analysis technique, step by step, for measuring the **L** parameter.

Rafting and further coarsening of rafted microstructure leading to full topological inversion, is a quite complex process. This procedure allows the use of one benchmark for all states and helps visualization of the tendency for the microstructure changes, caused by creep deformation.

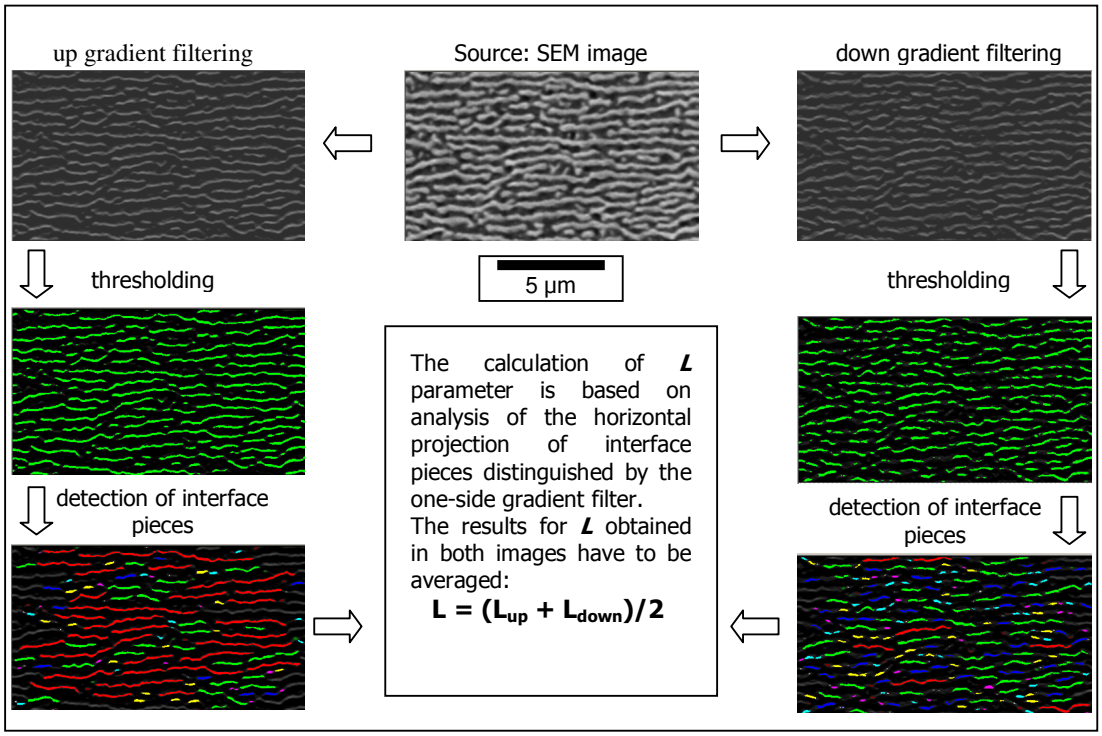

Fig. 29. Schematic procedure for the **L** parameter determination

The parameters **L** and **T** were used to determine rafting parameter **R** proposed by Ignat et al. [51], which is a dimensionless quantity and is therefore independent of a scale. The parameter **R** is defined as **R = L /(2T)** and for un-rafted structure **R** is equal to 0.5, but increases in magnitude rapidly, reaching its maximum for the longest and thinnest rafts and then decreasing during the final rafting process when microstructural inversion occurs [50].

10. Focused Ion Beam tomography

The Focused Ion Beam (FIB) has become an important tool in materials science for studying and modifying materials systems at the micro and nanometer levels. The technique, due to its ability to perform precise in-situ milling in the desired areas (so-called "targeted specimen preparation"), has been widely applied for studying three-dimensional microstructural and chemical relationships. With the help of computer algorithms for processing data and graphics packages for display, three-dimensional systems can easily be reconstructed and provide both qualitative and quantitative information [52, 53].

The FIB tomography investigation was performed on two samples (TEM thin foils) of PWA 1497 superalloy; baseline and after creep rupture test (sample no 2 crept at 982 °C/248 MPa, creep strain 25%, duration 870 h) materials. Tomographic data sets were obtained using

dual-beam FIB NEON 40EsB CrossBeam of Zeiss, by serial sectioning. The Pt protective layer was deposited on the surface of both samples (see Fig. 30), in order to prevented the occurrence of the curtaining effect, i.e., the irregular removal of material [54].

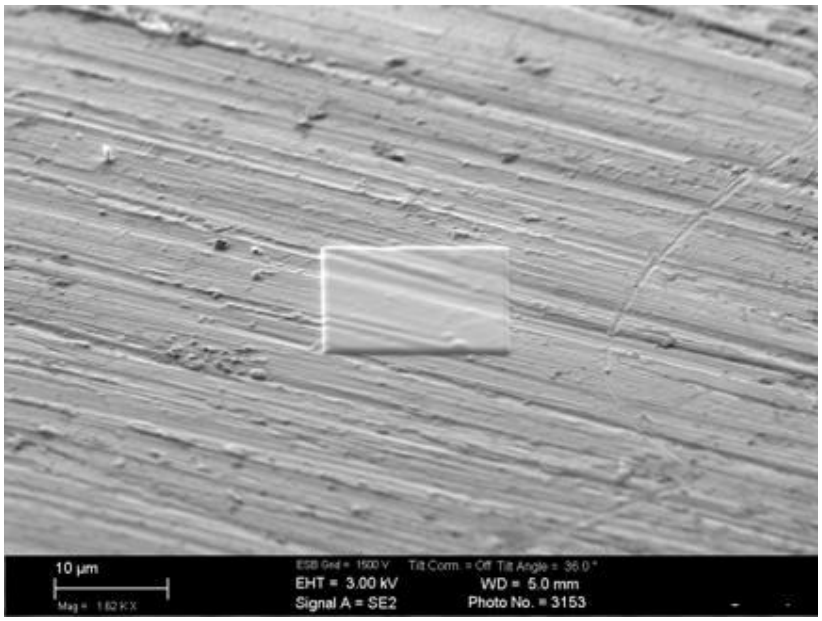

Fig.30. The SEM image shows platinum protective layer deposited on the surface of the PWA 1497 baseline sample.

The material was removed with a Ga-ion beam (optimum beam current and voltage: 200 pA and 30 kV). Fig. 31 shows the PWA 1497 surface prepared (by milling) for step sectioning and image acquisition. The thickness of each slice was chosen as10 nm.

The SEM micrographs of un-etched γ-γ' microstructure were recorded using energy selective backscattered electron (EsB) detector, which provide the best phase contrast and uniform gray level for phase visualization. The working distance was 5 mm and voltage 1.7 kV. More than 200 sections were recorded for baseline sample and around 450 sections for creep ruptured sample. The shift of the electron beam in lateral direction due to slice cutting during recording of the tomogram was calculated and subsequently corrected with the computer software, Fiji [55]. From the series of SEM micrographs, a 3D representation of the investigated alloy volume was generated by computer software, Avizo Fire 6.2 [56]. This program uses the "labelling by reconstruction" technique, based on the "neighbourhood-algorithm" [57]. This algorithm comprises neighboring voxels with the same gray scale to local objects. Non continuous ranges were identified and marked by colours.

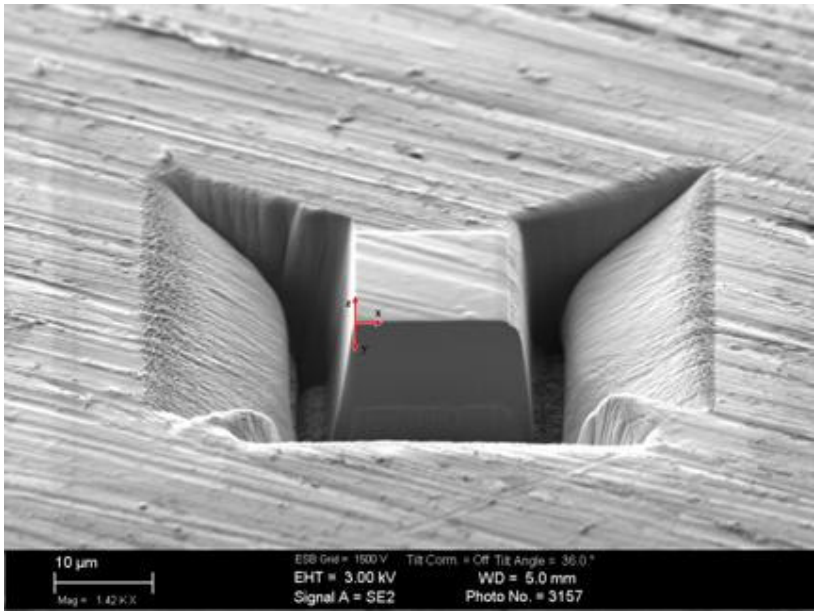

Fig.31. The SEM image shows the surface (perpendicular to the sample surface) prepared (by milling) for step sectioning and image acquisition of the PWA 1497 baseline sample.

IV. RESULTS

1. Microstructural characterization of second generation nickel-base superalloy PWA 1484

1.1. Baseline material

Characterization of baseline material was complex and included XRD measurements of crystallographic orientation, LM, SEM and TEM analyses.

The XRD measurements of crystallographic orientation revealed that the baseline material bar of the PWA 1484 superalloy exhibited (107) plane orientation and disorientation angle from (001) plane was 8.13º, Fig. 32. This disorientation is fully acceptable for commercially manufactured turbine blades [17].

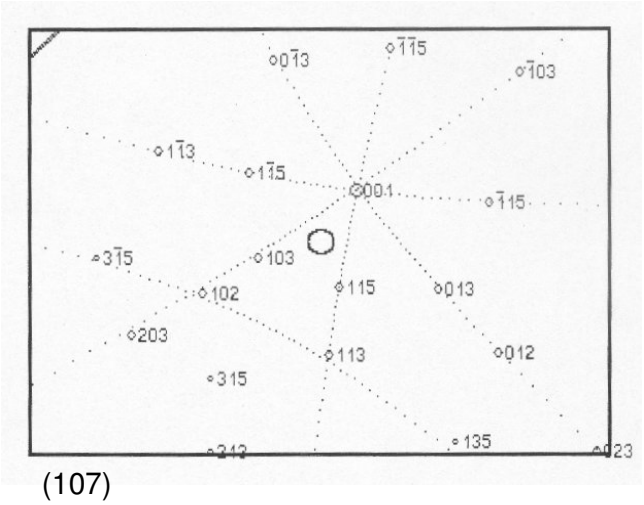

Fig. 32. Crystallographic orientation of the single crystal PWA 1484 baseline bar, disorientation angle from (001) plane is 8.13º

Metallographic examinations of the baseline material by means of LM revealed the presence of remaining dendritic microstructure with residual γ-γ'eutectic areas and pores, Fig. 33.

The TEM analysis of the PWA 1484 microstructure performed using thin foils showed the regular cuboidal morphology of γ' particles separated by γ channels, Fig. 34a. Electron diffraction pattern (SAED) shows lattice reflections belonging to γ and γ' phases, zone axis [010] (Fig. 34b).

Quantitative microstructural analysis of the baseline material was performed on TEM micrographs by means of the AnalySIS program and more than 300 γ'particles were taken into account. The surface fraction of γ' particles was measured as 79%. The mean size of γ'

particles was 447 nm. The particle size distribution is shown in Fig 35. The shape coefficient for γ' particles was approximately 1.5, which means that the shape of particles varied slightly from cuboidal. The mean width of γ channels was measured as 63 nm. All quantitative results of the PWA 1484 baseline material are summarized in Table 10.

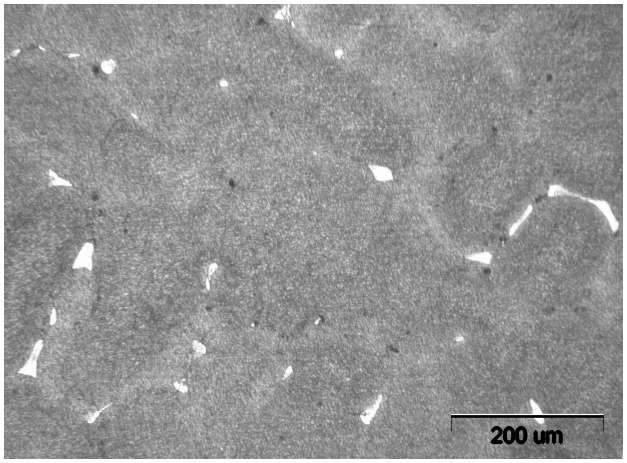

Fig. 33. PWA 1484 baseline material; dendritic microstructure with residual eutectics (white), pores (black), LM

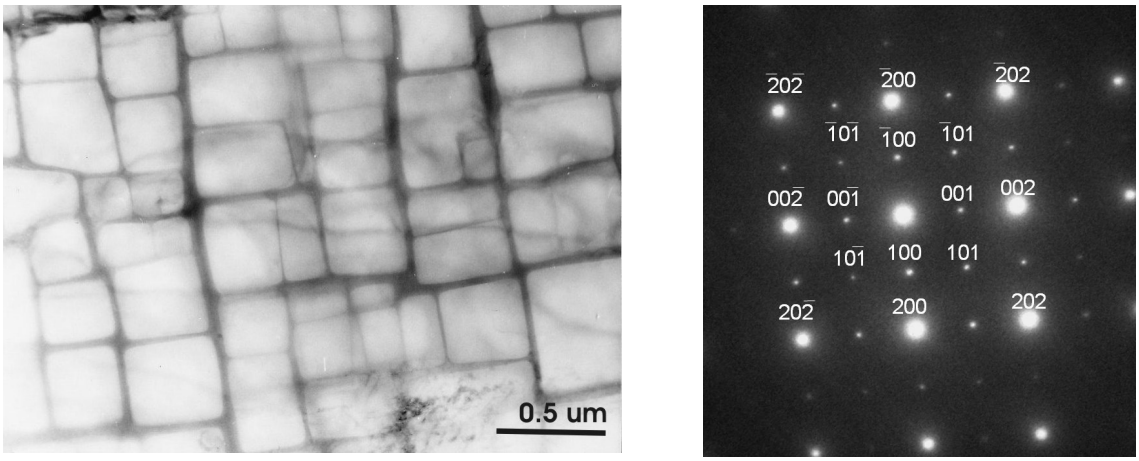

a) b)

Fig. 34. PWA 1484 baseline material; a) regular cuboidal morphology of γ' particles separated by γ channels, b) electron diffraction pattern taken from both γ and γ' phases, TEM

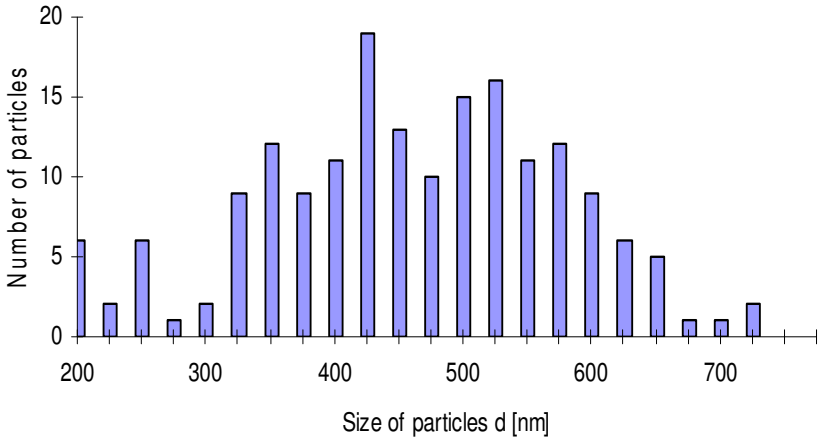

Fig. 35. The γ' particle size distribution of PWA 1484 baseline material

Table 10. Microstructural parameters of the PWA 1484 baseline material

Parameters Material	**f_s [%]** (surface fraction)	**V_v [%]** (volume fraction)	**D [nm]** (γ' mean size)	**k** (shape coefficient)	**S [nm]** (γ average width)
PWA 1484	79	79	447 ± 118	1.44 ± 0.36	63 ± 6

1.2. Creep deformed material

Both SEM and TEM microstructural analyses were performed for investigation of the microstructure stability of PWA 1484 superalloy during creep deformation. Figs 36-40 show microstructure evolution of the samples crept at 982 °C and 193 MPa. The microstructures of the other samples crept at 982 °C and 248MPa are presented on the Figs 41-45.

The micrographs presented in Figs 36-45 show the typical microstructure evolution for single crystal nickel-base superalloys subjected to high temperature creep deformation. The cubic γ' phase particles transform under the influence of stress and temperature into plates (rafts). The rafts develop in the early stages of creep. Simultaneously with the rafting process, a thickening of the γ matrix channels parallel to the rafts occurs.

Samples which were creep tested at 193 MPa exhibited the following microstructural changes. The microstructure of sample no 8 shows that rafting process is at an advanced stage. The γ' particles are mostly connected forming a lamellar microstructure. The microstructure inversion is clearly visible on sample no 9 (Fig. 37) which demonstrates the microstructure with long γ' lamellas and wide γ channels. The coarsening of rafted microstructure is clearly visible on sample no 10 (Fig. 38). The γ' phase particles start to join

neighbouring lamellas and rafts become more “wavy”. Widening of γ channels is still visible. The microstructures of samples no 4 and 3, which were creep tested to rupture, (Figs. 39, 40) show the final state of the coarsening of rafted microstructure, where γ’ phase becoming topologically the matrix and γ phase starting to look like the precipitates.

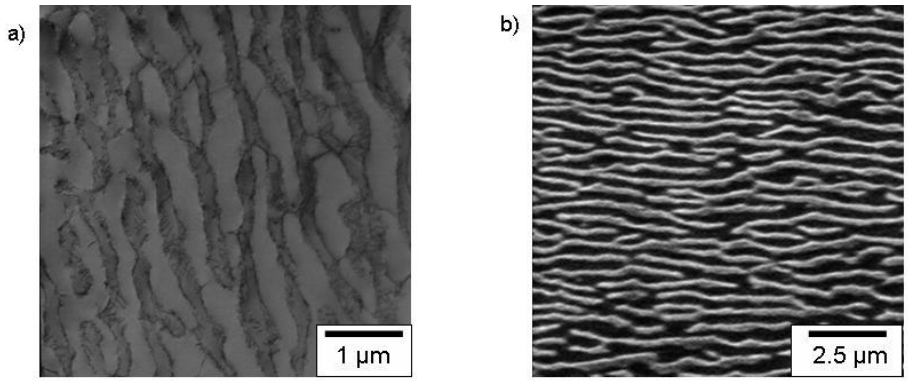

Fig. 36. PWA 1484, sample no 8, crept at 982 °C/193MPa, creep strain 0.63%, duration 264 h. Advanced rafting: γ’ particles are mostly connected, creating a long lamellar microstructure, and widening of γ channels; a) TEM, b) SEM

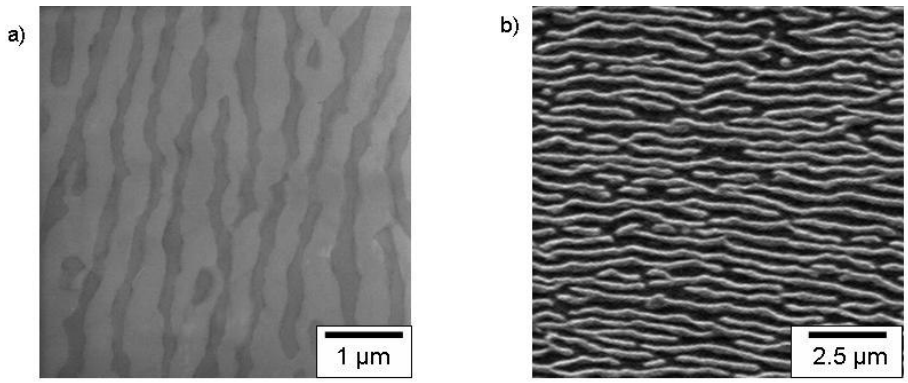

Fig. 37. PWA 1484, sample no 9, crept at 982 °C/193MPa, creep strain 1.0%, duration 473 h. Showing the microstructural inversion: γ’ phase is in the form of long lamellas, widening of γ channels; a) TEM, b) SEM

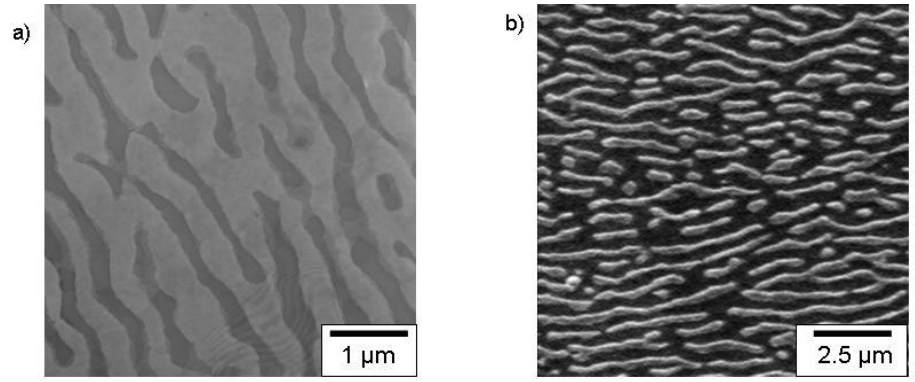

Fig. 38. PWA 1484, sample no 10, crept at 982 °C/193MPa, creep strain 2.5%, duration 596 h, showing the coarsening of rafted microstructure, γ' phase starting to join neighbouring lamellae, rafts become more "wavy", and widening of γ channels; a) TEM, b) SEM

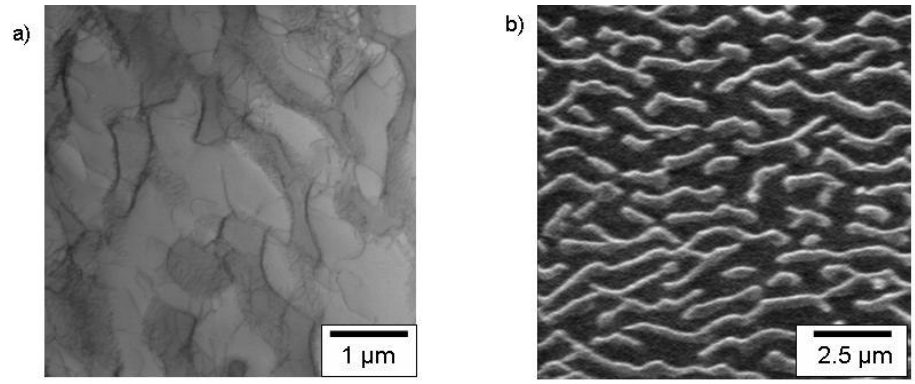

Fig. 39. PWA 1484, sample no 4, crept at 982 °C/193MPa (ruptured), creep strain 29 %, duration 898 h, showing the final state of coarsening of rafted microstructure, γ' phase becoming topologically the matrix and γ phase starting to look like the precipitates; a) TEM, b) SEM

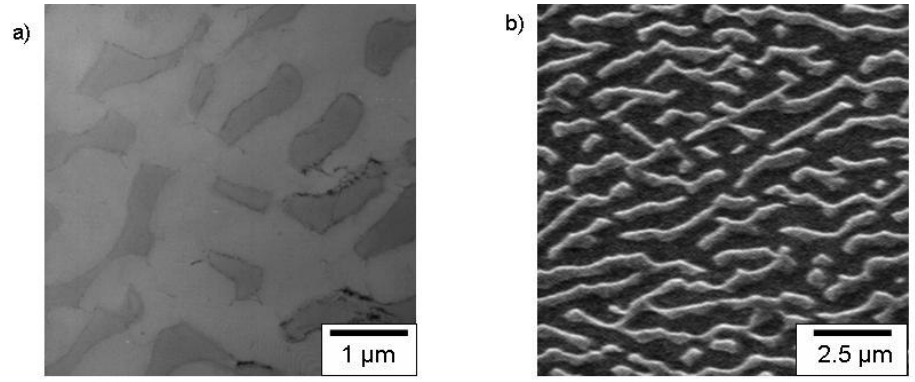

Fig. 40. PWA 1484, sample no 3, crept at 982 °C/193MPa (ruptured), creep strain 30 %, duration 971 h, showing the final state of coarsening of rafted microstructure, γ' phase becoming topologically the matrix and γ phase starting to look like the precipitates; a) TEM, b) SEM

The microstructures of second group of 5 samples (Figs 41-45) which were creep tested at a higher stress of 248 MPa, show similar microstructural changes to the first group of samples creep tested at 193 MPa. However, the rate of microstructural change is faster due to the higher applied stress. Sample no 5 (Fig. 41) shows the advanced stage of the rafting process. The γ' particles are mostly connected creating a lamellar microstructure. The microstructures of samples no 6 and 7 (Fig 42, 43) demonstrate the coarsening of rafted microstructure. The final stage of the coarsening of rafted microstructure is visible on samples no 2 and 1 (Figs 44, 45), which were ruptured. At this duration in the creep tests, the γ' phase become topologically the matrix and γ phase begin to look like the precipitates.

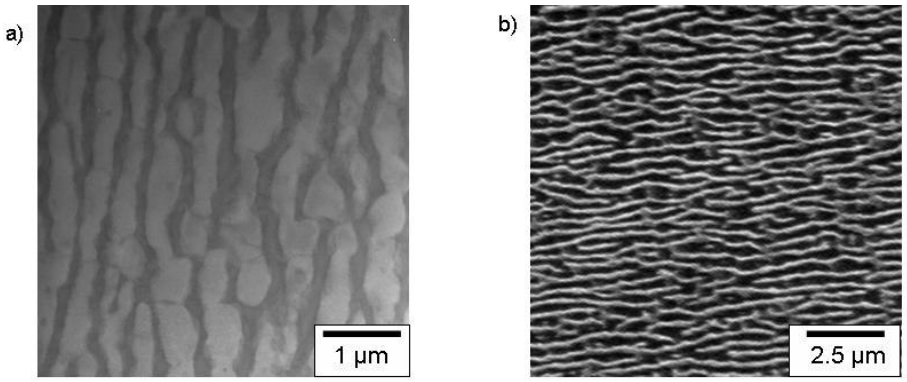

Fig. 41. PWA 1484, sample no 5, crept at 982 °C/248MPa, creep strain 0.71%, duration 70 h, showing the advanced rafting process; γ' particles are mostly connected, creating a long lamellar microstructure, and widening of γ channels; a) TEM, b) SEM

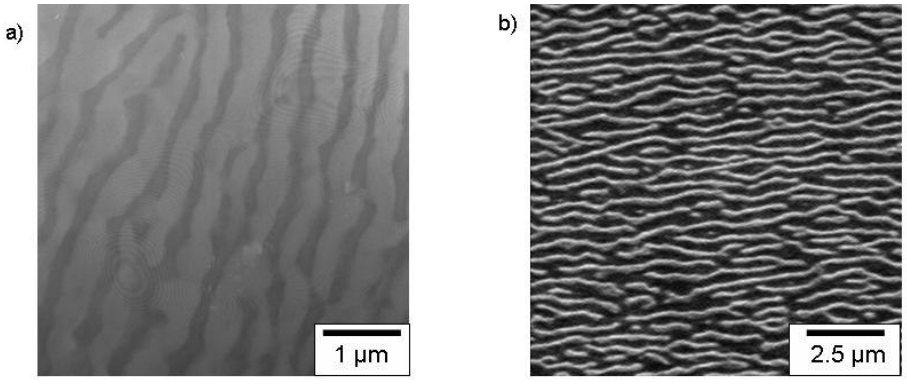

Fig. 42. PWA 1484, sample no 6, crept at 982 °C/248MPa, creep strain 1.5%, duration 140 h showing the coarsening of rafted microstructure. The γ' phase has formed long lamellae, widening of γ channels; a) TEM, b) SEM

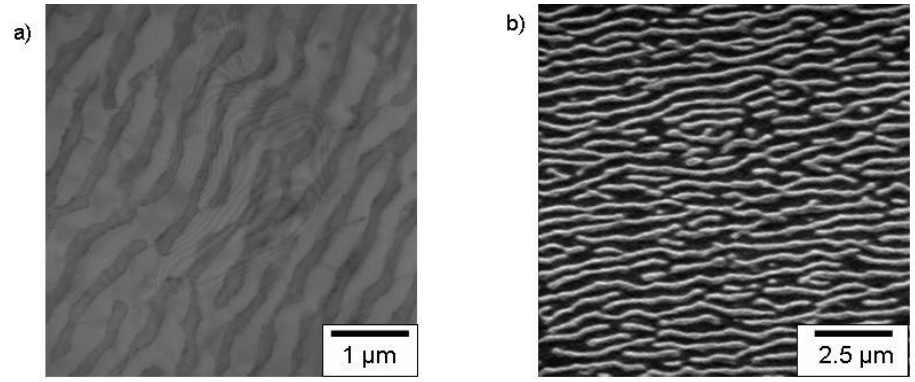

Fig. 43. PWA 1484, sample no 7, crept at 982 °C/248MPa, creep strain 2.2%, duration 142 h, showing the coarsening of rafted microstructure. The γ' phase has formed long lamellae, widening of γ channels; a) TEM, b) SEM

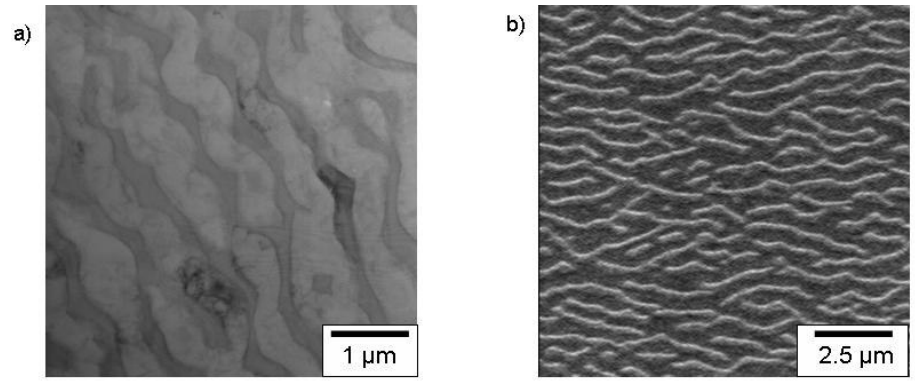

Fig. 44. PWA 1484, sample no 2, crept at 982 °C/248MPa (ruptured), creep strain 26%, duration 281 h. This is the final state of the coarsening of rafted microstructure, γ' phase becoming topologically the matrix and γ phase starting to look like precipitates; a) TEM, b) SEM

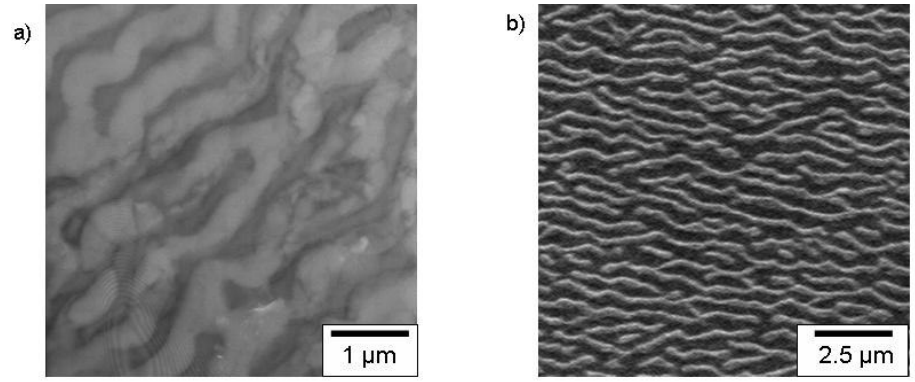

Fig. 45. PWA 1484, sample no 1, crept at 982 °C/248MPa (ruptured), creep strain 12 %, duration 289 h exhibiting the final stage of the coarsening of rafted microstructure, γ' phase becoming topologically the matrix and γ phase starting to look like precipitates; a) TEM, b) SEM

The evolution of the PWA 1484 superalloy microstructure during creep deformation was characterized quantitatively using four parameters: ***L*** – mean length of γ/γ' interface boundary, ***T*** – mean thickness of γ' phase, ***S*** – mean spacing of γ phase, ***R*** – rafting parameter ***R = L /(2T)***. The parameters and procedure of calculation have already been described in detail in Chapter III-9.2. The microstructural parameters with their standard deviations are given in Table 11.

Table 11. Evolution of microstructural parameters during creep deformation of PWA 1484

No.	Temp. [℃]	σ [MPa]	Duration [h]	Creep strain [%]	L [nm]	Δ [nm]	S [nm]	Δ [nm]	T [nm]	Δ [nm]	R
8	982	193	264.3	0.629	2410	±2000	230	±80	280	±100	4.30
9	982	193	473.9	1.002	1720	±1540	210	±60	290	±110	2.96
10	982	193	596.6	2.522	1410	±1110	270	±80	360	±160	1.95
4	982	193	898.6	28.762	1280	±690	410	±190	570	±360	1.12
3	982	193	971.2	29.758	1180	±770	390	±170	730	±440	0.80
5	982	248	697	0.714	1340	±860	170	±70	270	±90	2.48
6	982	248	139.4	1.465	1570	±1240	200	±70	300	±90	2.61
7	982	248	141.5	2.223	1670	±1300	200	±80	300	±90	2.78
2	982	248	280.7	25.633	940	±460	260	±80	440	±150	1.06
1	982	248	289.1	11.43	920	±450	270	±100	430	±170	1.06

The results were also plotted as a function of creep strain and creep duration. Plots are arranged in two columns, corresponding to 193 MPa (right column) and 248 MPa (left column) stresses, respectively. The evolution of parameters S and T is shown on Figs 46 and 47. Parameters L and R are presented on Figs 48 and 49.

The results obtained for both stresses show a similar tendency. The mean spacing of γ phase ***S*** increases during the creep process, more then six times for the ruptured specimen (for 193 MPa) in comparison with baseline material and more then four times for 248 MPa. The evolution of the microstructural parameter **T,** which represents the mean thickness of γ' phase, shows that **T** parameter increases, reaching the highest value for a topological inversion of a microstructure. The mean length of γ/γ' interface boundary (**L** parameter) decreases as evolution of microstructure proceeds and the rafts become more wavy and convoluted, and the change in **L** is more marked for longer creep times and lower creep stresses. The evolution of the rafting parameter **R = L / 2T** shows that it reaches the maximum for the highest L values, then subsequently decreases at higher creep strains due to microstructural inversion of the superalloy.

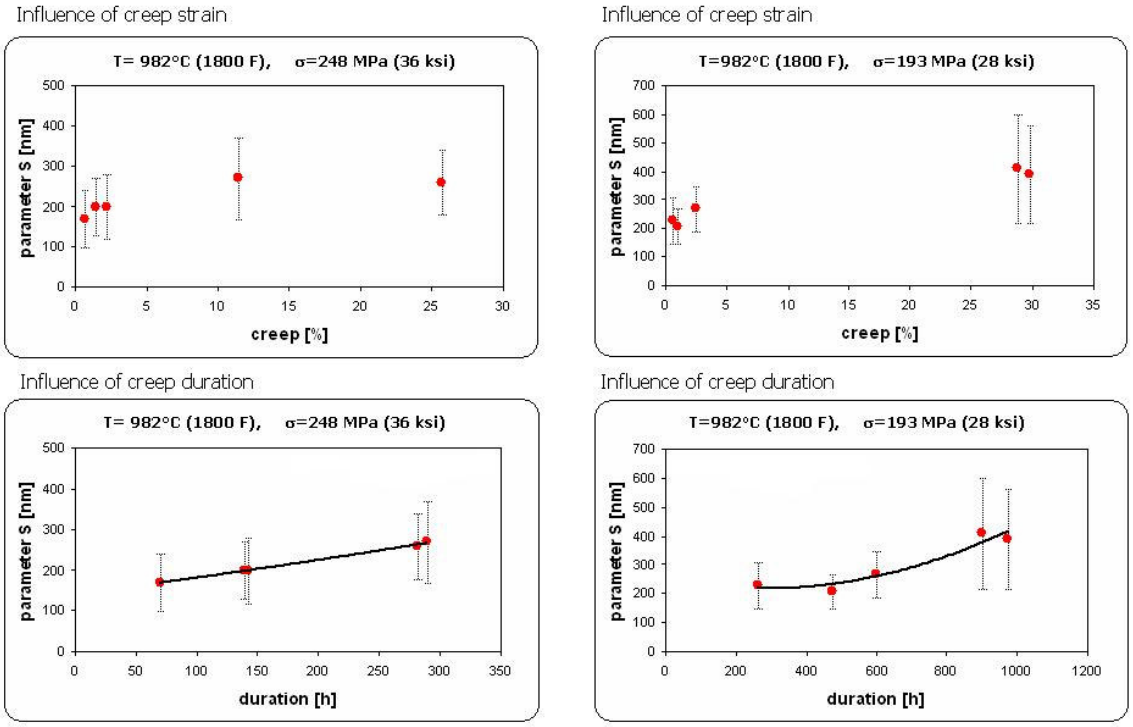

Fig. 46. Evolution of the microstructural parameter **S** (mean spacing of γ phase). The **S** parameter increases during creep process, doubling its value for the ruptured specimen.

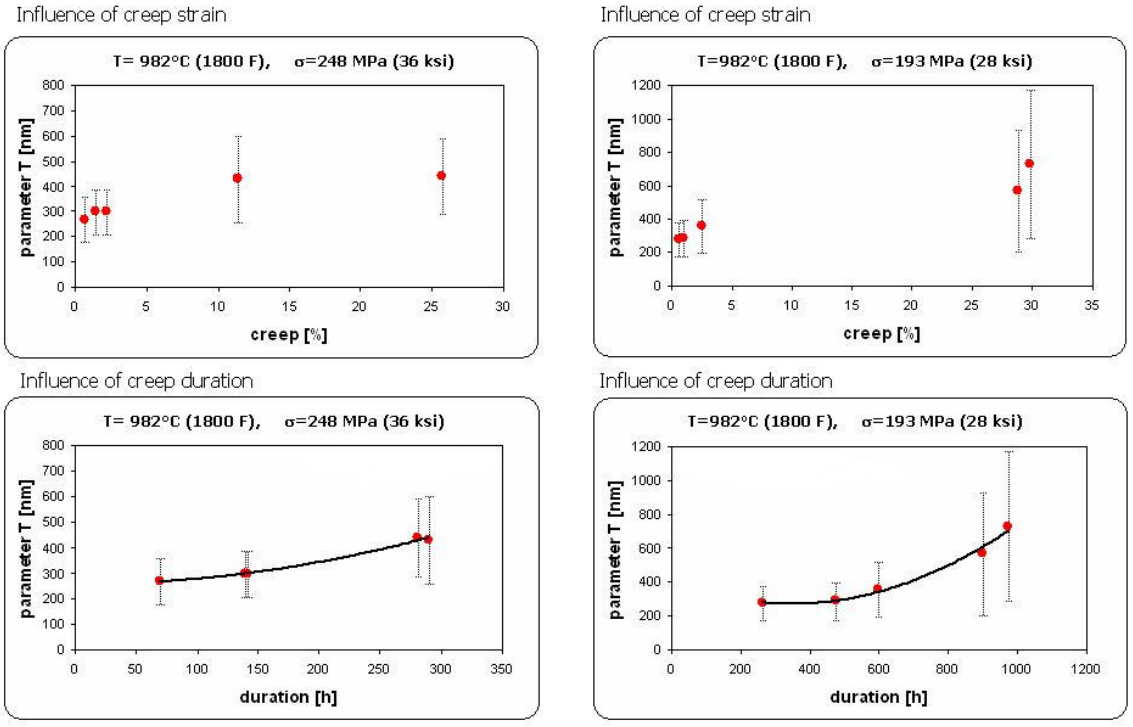

Fig. 47. Evolution of the microstructural parameter **T** (mean thickness of γ' phase). The **T** parameter increases, reaching the highest value for the final state of coarsening of rafted microstructure

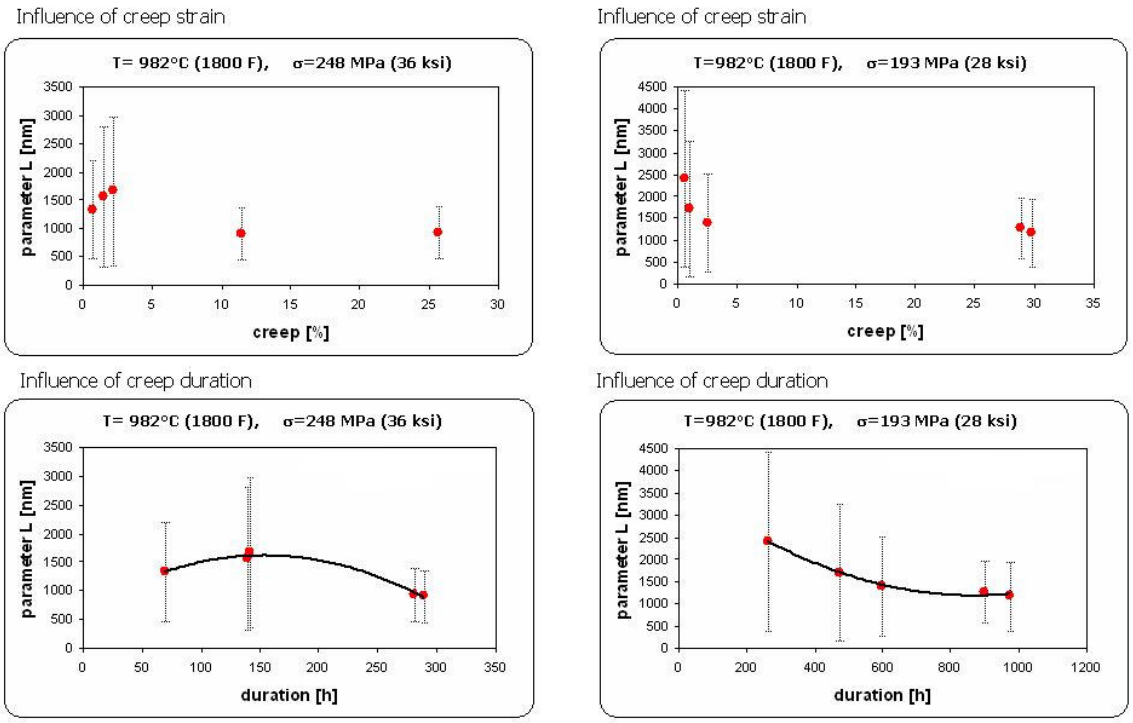

Fig. 48. Evolution of the microstructural parameter **L** (mean length of γ/γ' interface boundary). The **L** parameter decreases as coarsening of rafted microstructure proceeds and the rafts become more wavy and convoluted.

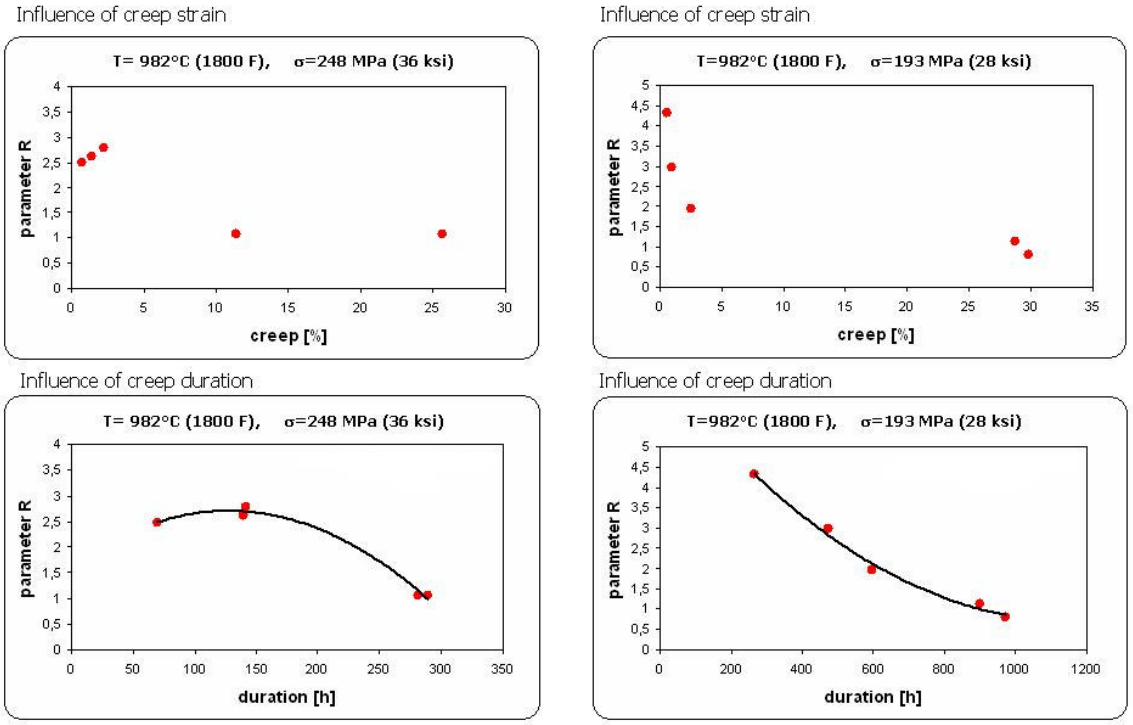

Fig. 49. Evolution of the microstructural parameter: **R = L / 2T**. The rafting parameter R reaches the maximum for the highest L values, then subsequently decreases at higher creep strains as coarsening of rafted microstructure proceeds and the rafts become more wavy and convoluted.

During primary creep, the γ' precipitates start to link together early and continue to develop well into steady-state creep by their increased lateral extension. After about 260 h (for 193 MPa) and 140 h (for 248 MPa) of creep testing, the γ' rafts were very long and extended completely across both SEM and TEM micrographs from one side to the other.
During extended creep deformation (after approx. 900 h for 193 MPa and 280 h for 248 MPa), the rafts become more "wavy" and they started to join each other. This evolution leads to an effect called "topological inversion". This process is described by Epishin et al. [39], explaining the formation of junctions connecting neighbouring γ' rafts and separating the γ phase. At the final stage of the process, the γ' phase becomes topologically the matrix, surrounding the γ phase. Transformation of the long γ-lamellae into short inclusions leads to an increase of dislocation motion in the γ phase [39]. Moreover, the isolation of the γ phase is not completed, making dislocation climb still possible. Therefore a topological inversion of the γ-γ' microstructure is accompanied by a drastic increase in the creep rate of the superalloy [39, 49, 58].

2. Microstructural characterization of fourth generation single crystal nickel-base superalloy PWA 1497

2.1. Baseline material

Characterization of the baseline material of the PWA 1497 was complex and included XRD measurements, LM, SEM and TEM analyses. The whole scientific approach was made in the same manner as for the second generation superalloy PWA 1484, described in Chapter IV - 1.

The XRD measurements of crystallographic orientation reveal that baseline bar of the PWA 1497 superalloy exhibits near (001) orientation and disorientation angle from (001) plane was 0.7º, Fig 50.

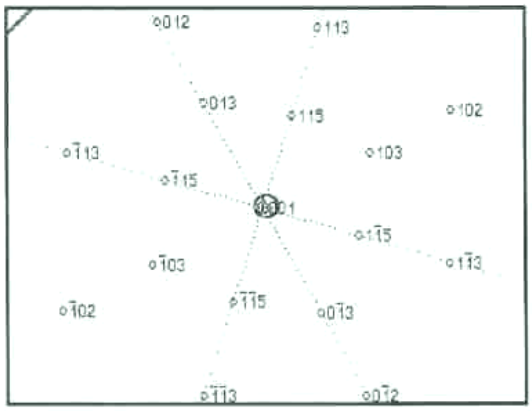

Fig. 50. Crystallographic orientation of the single crystal PWA 1497 baseline bar, disorientation angle from (001) plane is 0.7º

Metallographic examinations of the baseline material by means of LM revealed the presence of residual dendritic microstructure with γ-γ'eutectic areas and pores, Fig 51.

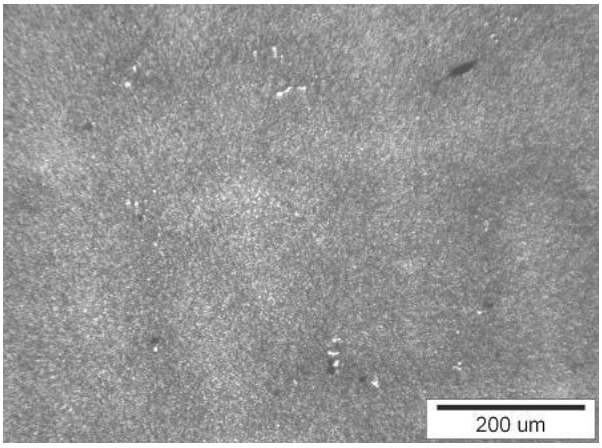

Fig. 51. PWA 1497 baseline material; dendritic microstructure with residual eutectics (white) and pores (black), LM

The TEM analysis of the PWA 1497 microstructure showed the regular cuboidal morphology of γ' particles separated by γ channels, Fig. 52a. Electron diffraction pattern (SAED) shows lattice reflections belonging to γ and γ' phases, zone axis [010] (Fig. 52b).

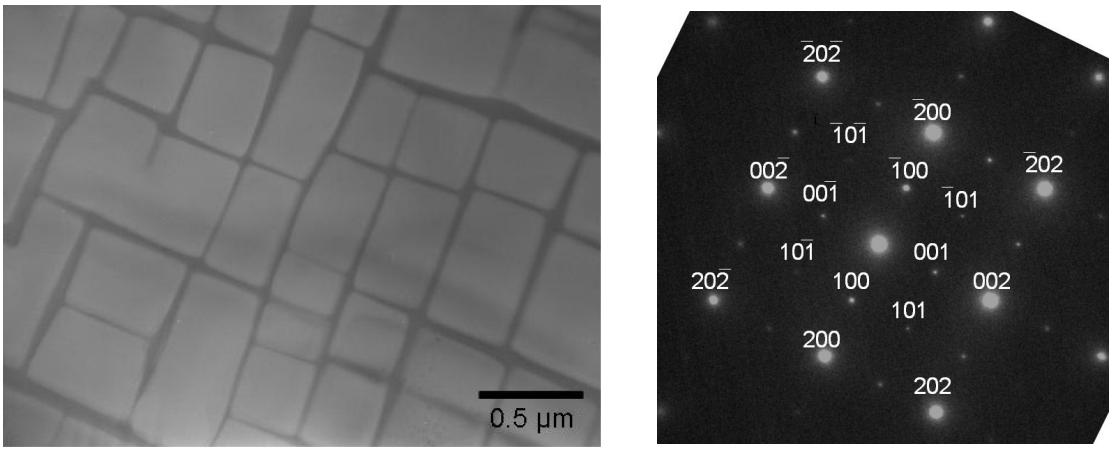

a) b)

Fig. 52. PWA 1497 baseline material; a) regular cuboidal morphology of γ' particles separated by γ channels, b) electron diffraction pattern taken from both γ and γ' phases, TEM

Quantitative microstructural analysis of the baseline material was performed on TEM micrographs; more than 300 γ' particles were taken to account. The surface fraction of γ' particles was measured as 72%. The mean size of γ' particles was 442 nm. The particle size distribution is shown on Fig 53.

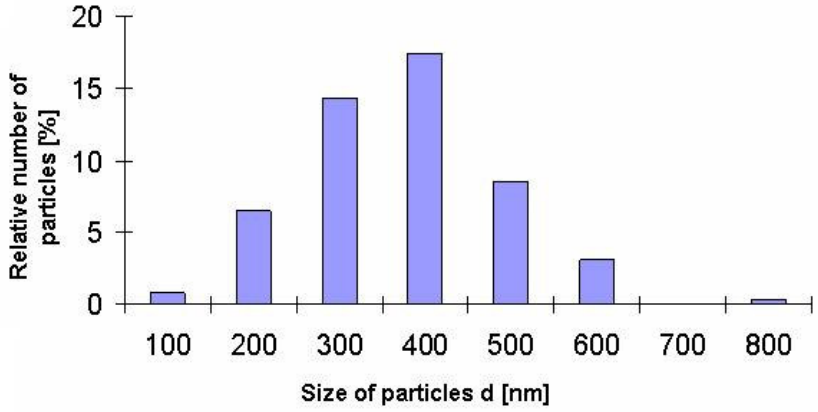

Fig. 53. The γ' particle size distribution of the PWA 1497 baseline material

The shape coefficient for γ' particles was approximately 1.5. The mean width of γ channels was measured as 70 nm. All quantitative results of PWA 1497 baseline material investigation are given in Table 12.

Table 12. Microstructure parameters of the PWA 1497 baseline material

Parameters Material	**f_s [%]** (surface fraction)	**V_v [%]** (volume fraction)	**D [nm]** (γ' mean size)	**k** (shape coefficient)	**S [nm]** (γ mean width)
PWA 1497	72	72	442 ± 113	1.5 ± 0.49	70 ± 3

2.2. Creep deformed material

Likewise for the PWA 1484 superalloy, both SEM and TEM microstructural analyses were performed for investigation of the microstructure stability of the PWA 1497 superalloy during creep deformation. Creep test conditions were given in Table 8 (Chapter III – 2.2). Figs 53-58 show the microstructure evolution of the samples crept at 982 °C and 248 MPa. The microstructure of the other samples crept at 982 °C and 310 MPa is presented in Figs 59-64.

The micrographs presented in Figs 53-64 show the typical microstructural evolution for single crystal nickel base superalloys subjected to high temperature creep deformation.

First six samples which were creep tested with 248 MPa stress, characterize the following microstructural changes. Sample no 8 (Fig. 53) creep tested for 1.6 hours only, does not demonstrate any microstructural changes; its microstructure is similar to the baseline material. The microstructure of sample no 9 (Fig. 54) demonstrates rearrangement of γ' particles, which leads to formation of long lamellas; this process was described in detail in Chapter II-5. The microstructural inversion is visible on samples no 10 and 11 (Figs 55, 56). The γ' particles are mostly connected, creating very long lamellae with rafts extending completely through the sample. The widening of γ channels at this point is clearly seen. Sample no 12 (Fig. 57) demonstrates the coarsening of rafted microstructure. At this point the rafts become more "wavy" and γ' phase start to join neighbouring lamellas. The final state of coarsening of rafted microstructure is clearly visible on sample no 2 (Fig. 58), which was ruptured after nearly 900 h of creep duration. In this case, γ' phase has become topologically the matrix and γ phase begins to look like the precipitates. For the final state of deformation of sample no 2, the γ phase have become the widest.

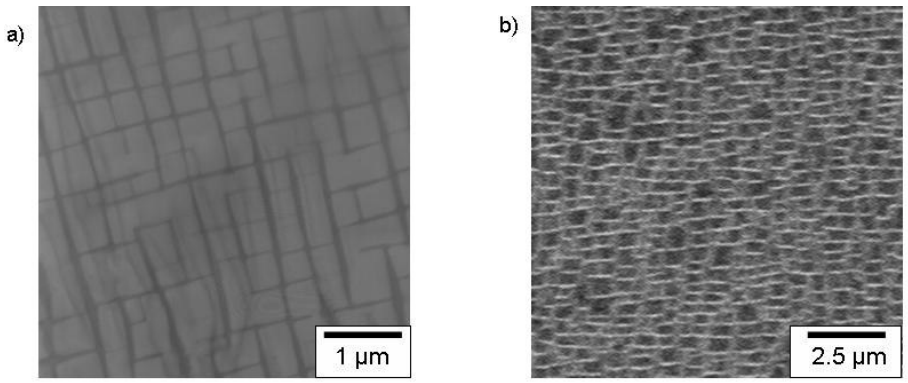

Fig. 53. PWA 1497, sample no 8, crept at 982 °C/248 MPa, creep strain 0.05%, duration 1.6 h. The γ' particles are still well separated; a) TEM, b) SEM

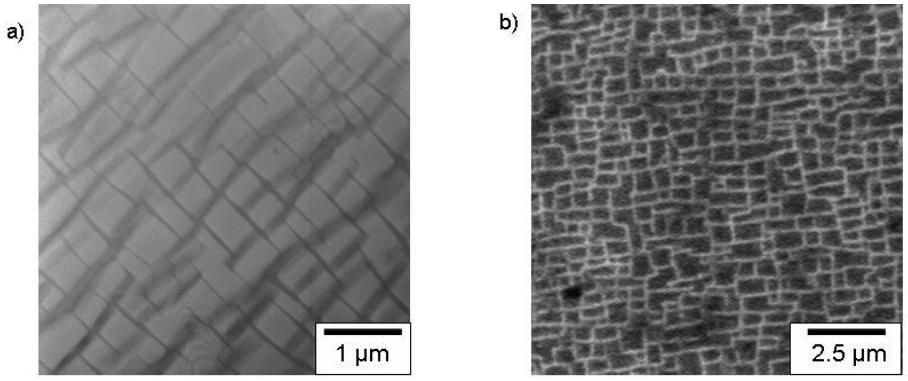

Fig. 54. PWA 1497, sample no 9, crept at 982 °C/248MPa, creep strain 0.08%, duration 220 h. The γ' particles are starting to rearrange, leading to formation of long lamellas and widening of γ channels; a) TEM, b) SEM

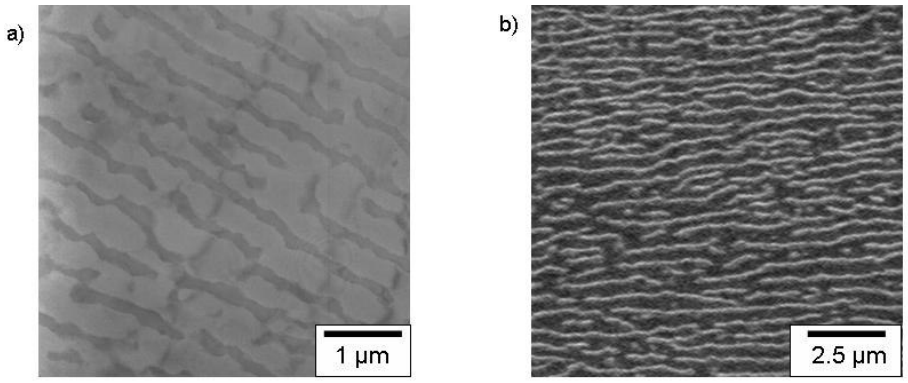

Fig. 55. PWA 1497, sample no 10, crept at 982 °C/248 MPa, creep strain 0.85%, duration 480 h. Microstructural inversion: γ' particles are mostly connected, forming long lamellae, with widening of γ channels; a) TEM, b) SEM

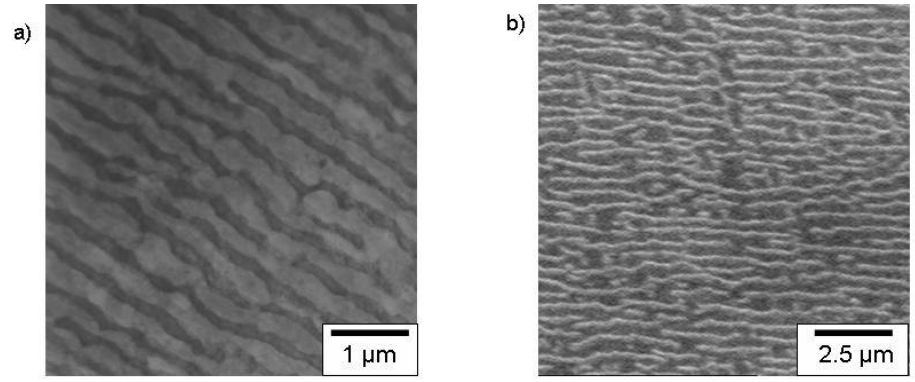

Fig. 56. PWA 1497, sample no 11, crept at 982 °C/248MPa, creep strain 1.1%, duration 480 h, showing the microstructural inversion -γ' particles are mostly connected, creating long lamellae, and widening of γ channels; a) TEM, b) SEM

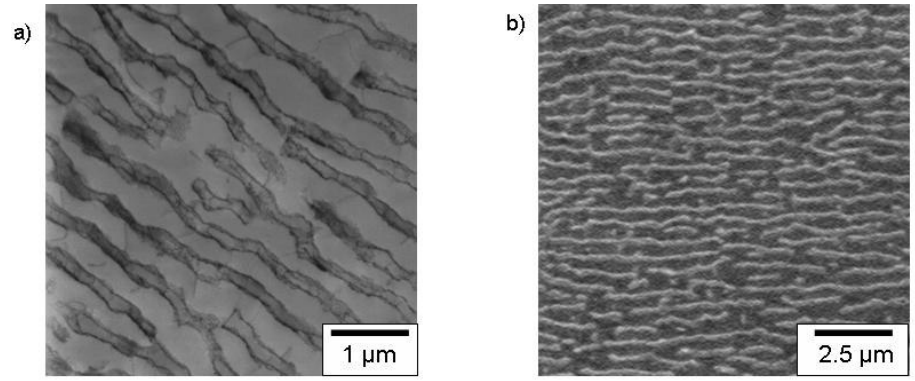

Fig. 57. PWA 1497, sample no 12, crept at 982 °C/248MPa, creep strain 2.0 %, duration 600 h, showing the coarsening of rafted microstructure, the γ' phase beginning to join neighbouring lamellae, rafts becoming more "wavy", and widening of γ channels; a) TEM, b) SEM

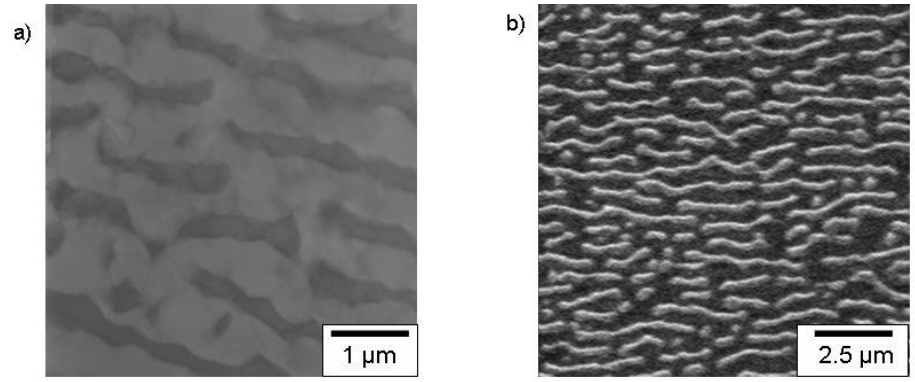

Fig. 58. PWA 1497, sample no 2, crept at 982 °C/248 MPa (ruptured), creep strain 25%, duration 870 h showing the final stage of coarsening of rafted microstructure, γ' phase becoming topologically the matrix and γ phase starting to look like the precipitates; a) TEM, b) SEM

The microstructures of the second group of six samples (Figs 59-64), which were creep tested at a higher stress of 310 MPa, show similar microstructural changes to the samples creep tested at 248 MPa. However, the rate of change is accelerated during entire creep process due to the higher applied stress.

The microstructure of sample no 4 in the beginning of creep deformation (Fig. 59) does not demonstrate any microstructure changes; γ' particles are still well separated. Sample no 6 (Fig. 60) shows the rearrangement of γ' particles, leading to the formation of long lamellas and widening of γ channels. The microstructural inversion is visible on samples no 5, (Figs 61). The γ' particles are mostly connected, forming long lamellae. The widening of γ channels is also very distinct. The coarsening of rafted microstructure is clearly visible on samples no 7 and 3 (Fig 62, 63). At the end of the creep test, sample no 1 which was ruptured after about 285 h (25% of creep strain) exhibited the final state of coarsening of rafted microstructure (Fig. 64).

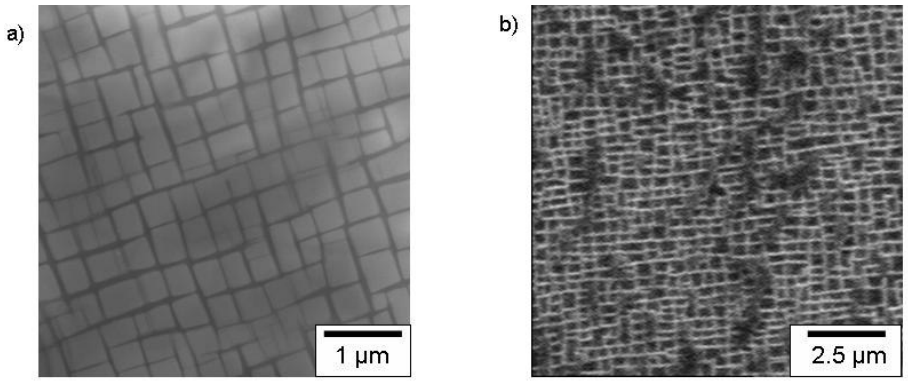

Fig. 59. PWA 1497, sample no 4, crept at 982 °C/310MPa, creep strain 0.07%, duration 17 h. At the beginning stage of creep, the γ' particles are still well separated; a) TEM, b) SEM,

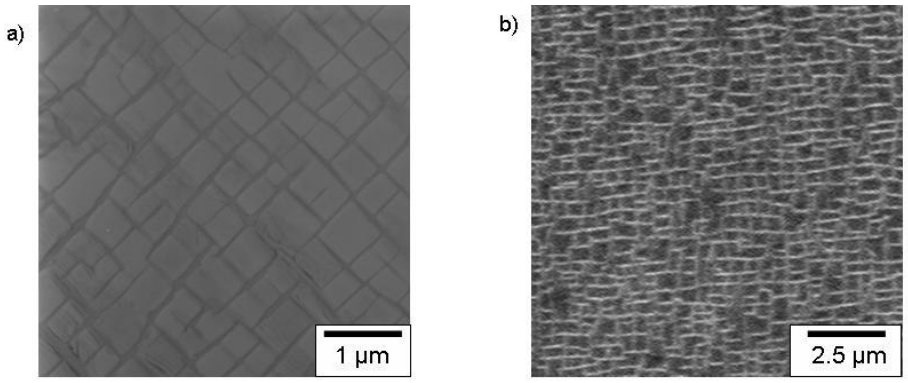

Fig. 60. PWA 1497, sample no 6, crept at 982 °C/310MPa, creep strain 0.1% duration 40 h. The γ' particles are starting to rearrange, leading to the formation of long lamellas and widening of γ phase; a) TEM, b) SEM

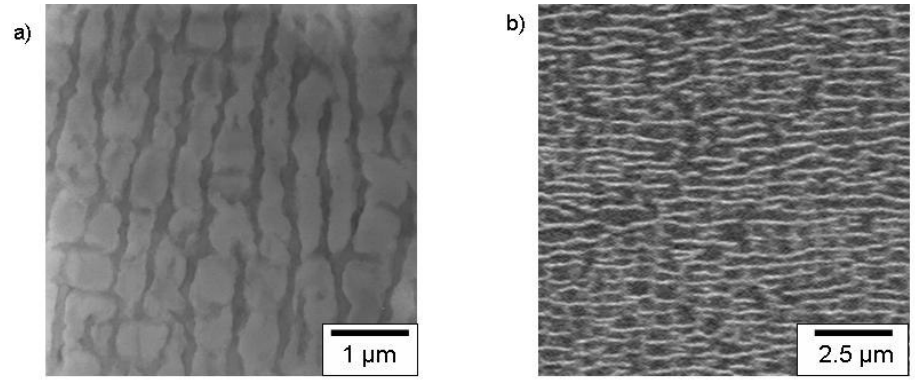

Fig. 61. PWA 1497, sample no 5, crept at 982 °C/310 MPa, creep strain 0.55%, duration 140 h. Showing the microstructural inversion: γ' phase is in the form of long lamellas, widening of γ channels; a) TEM, b) SEM

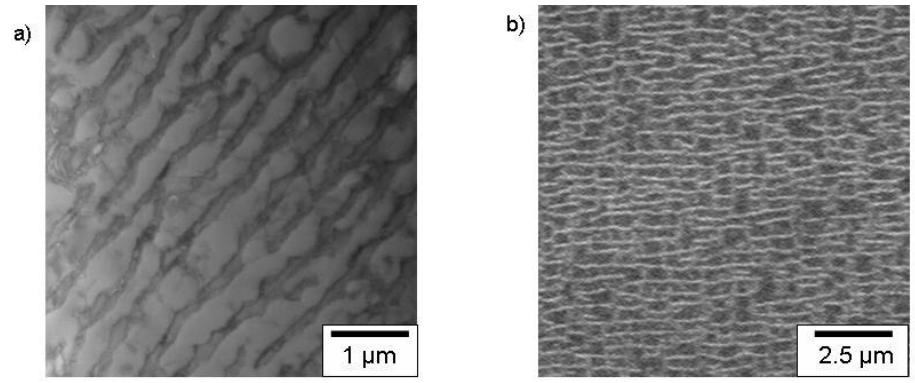

Fig. 62. PWA 1497, sample no 7, crept at 982 °C/310MPa, creep strain 0.98%, duration 167 h, showing the coarsening of rafted microstructure. The γ' phase has formed long lamellae, widening of γ channels; a) TEM, b) SEM

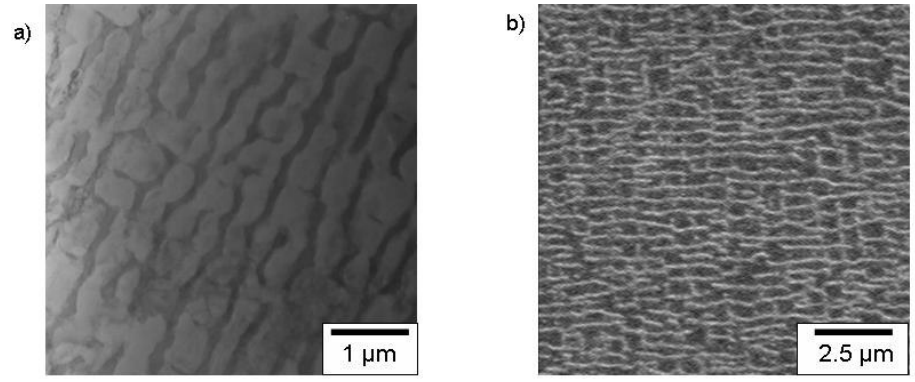

Fig. 63. PWA 1497, sample no 3, crept at 982 °C/310MPa, creep strain 2.0%, duration 190 h. Coarsening of rafted microstructure, γ' phase starting to join neighbouring lamellae, rafts become more "wavy", and widening of γ channels; a) TEM, b) SEM

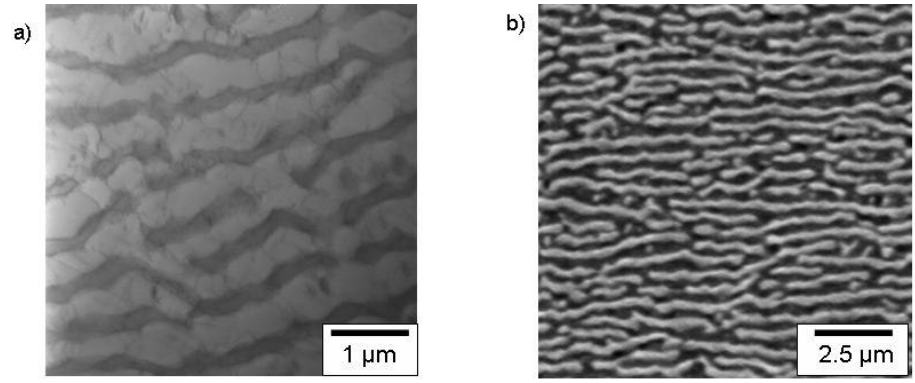

Fig. 64. PWA 1497, sample no 1, crept at 982 °C/310MPa (ruptured), creep strain 25 %, duration 286 h. This is the final state of coarsening of rafted microstructure, γ' phase becoming topologically the matrix and γ phase starting to look like the precipitates; a) TEM, b) SEM

The microstructural changes of the PWA 1497 are qualitatively similar to those of PWA 1484 superalloy already described in chapter IV-1.2

The evolution of the PWA 1497 superalloy microstructure during creep deformation was characterized quantitatively using four parameters: ***L*** – mean length of γ/γ' interface boundary, ***T*** – mean thickness of γ' phase, ***S*** – mean spacing of γ phase, ***R*** – rafting parameter ***R = L /(2T)***. The parameters and procedure of calculation was already described in detail in the Chapter III-9.2. The microstructural parameters with their standard deviations are given in Table 13.

Table 13. Evolution of microstructural parameters during creep deformation of PWA 1497

No.	Temp. [℃]	σ [MPa]	Duration [h]	Creep strain [%]	L [nm]	Δ [nm]	S [nm]	Δ [nm]	T [nm]	Δ [nm]	R
8	982	248	1.58	0.055	430	±230	100	±70	310	±160	0.69
9	982	248	219.58	0.079	470	±190	100	±70	400	±150	0.59
10	982	248	477.17	0.843	1480	±1030	170	±50	370	±130	2.00
11	982	248	477.45	1.050	1690	±1400	160	±50	280	±100	3.02
12	982	248	580.18	1.976	1920	±1410	270	±120	270	±110	3.55
2	982	248	867.41	24.793	1320	±1140	340	±120	490	±320	1.35
4	982	310	17.11	0.066	350	±150	80	±70	350	±150	0.50
6	982	310	39.61	0.110	320	±100	90	±80	300	±100	0.53
5	982	310	138.06	0.543	1000	±500	160	±90	320	±140	1.56
7	982	310	167.1	0.976	1290	±900	200	±80	270	±100	2.39
3	982	310	190.02	2.008	1480	±1000	180	±90	280	±110	2.64
1	982	310	285.05	24.808	1140	±800	240	±80	450	±250	1.27

The results were also plotted as a function of creep strain and creep duration. Plots are arranged in two columns, corresponding to 248 MPa (left column) and 310 MPa (right column) stresses, respectively. The evolution of parameter ***S*** and ***T*** is shown in Figs 65 and 66. The parameters ***L*** and ***R*** are presented in Figs 67 and 68.

The results obtained for both stresses show a similar tendency. The mean spacing of γ phase ***S*** increases during creep process, tripling its value for the ruptured specimen. For low creep strain (below 1%), ***T*** and ***L*** parameters have nearly constant values due to the cuboidal shape of γ' precipitates. Increasing creep strain above ~1% causes a decrease in mean thickness of γ' phase ***T***, which is associated with the increasing the mean length of γ/γ' interface boundary ***L*** up to maximum reached for ~2% strain**.** At higher creep strain, the ***T*** parameter increases, reaching the highest value for the final state of coarsening of rafted microstructure. The ***L*** parameter decreases as coarsening of rafted microstructure occur and the rafts become more wavy and convoluted. The rafting parameter ***R*** increases in the early stages of creep, reaches a maximum for the highest ***L*** values (at ~2% creep strain), then subsequently decreases at higher creep strain. The shape of the ***R***(ε) and ***R***(t) graphs is quite similar to corresponding ***L*** graphs due to the relatively small changes in ***T*** parameter.

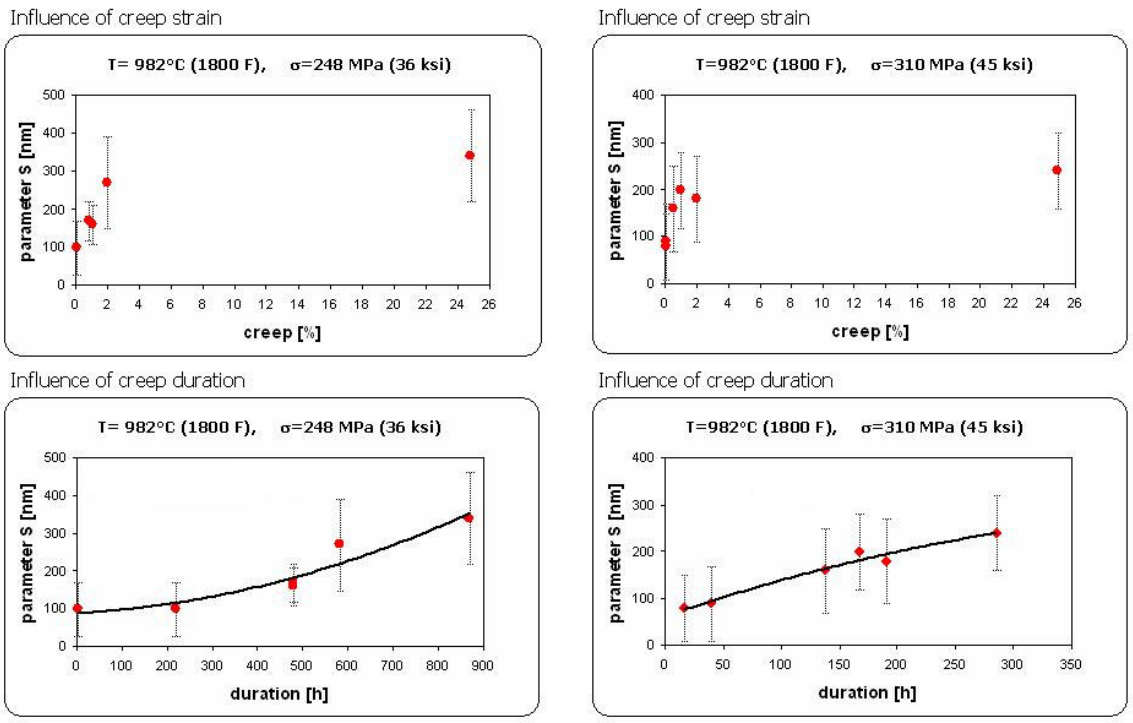

Fig. 65. The evolution of the microstructural parameter **S** (mean spacing of γ phase); the **S** parameter increases during the creep process, tripling its value for the ruptured specimen.

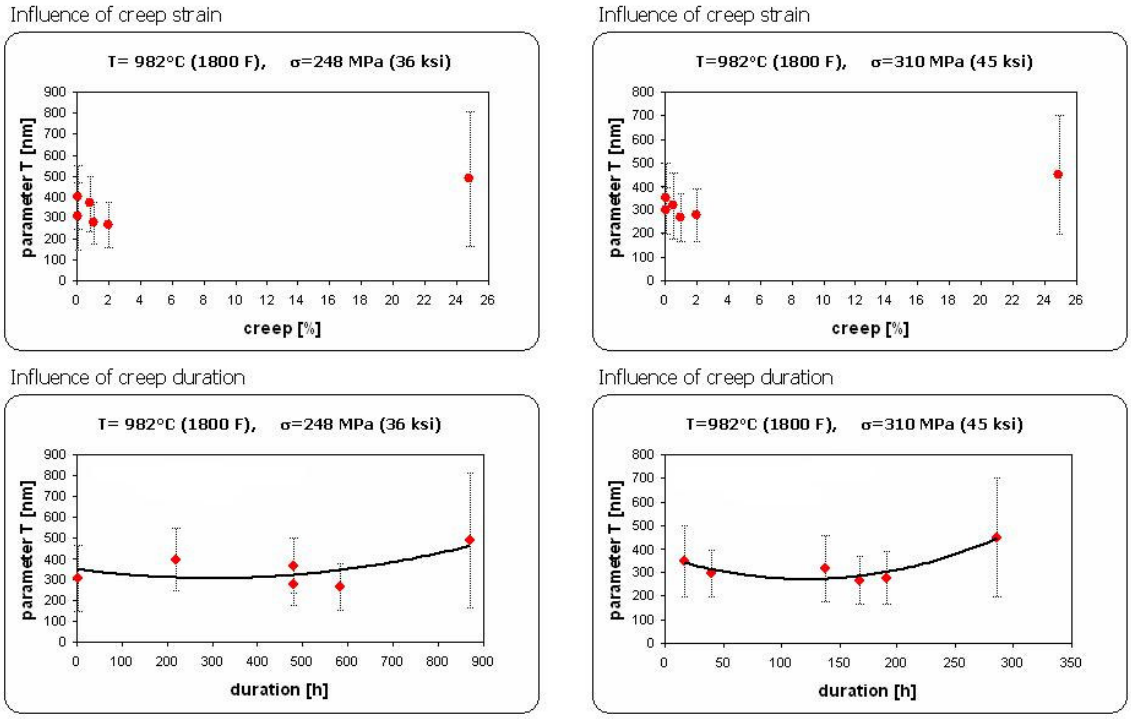

Fig. 66. Evolution of microstructural parameter **T** (mean thickness of γ'phase). The **T** parameter in the beginning decreases as the γ' particles start to create long lamellas and then increases, reaching the highest value for the final state of coarsening of rafted microstructure.

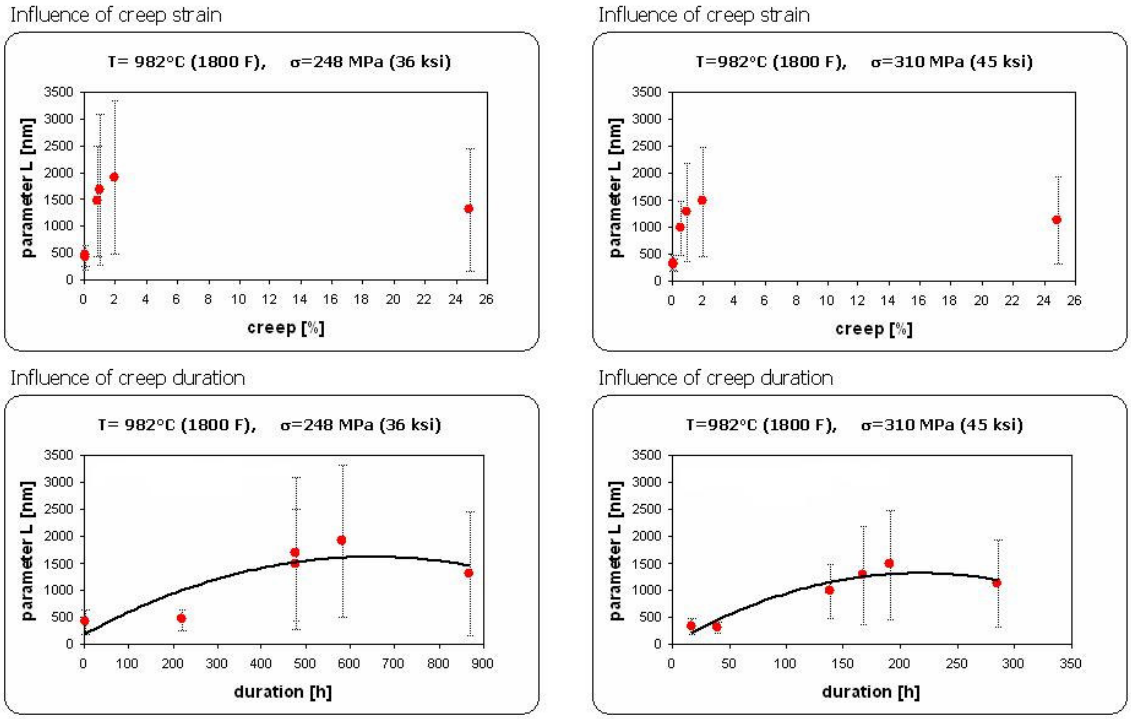

Fig. 67. Evolution of microstructural parameter **L** (mean length of γ/γ' interface boundary). The **L** parameter at first increases, reaching the highest value for the longest rafts and then decreases as coarsening of rafted microstructure proceeds and the rafts become more wavy and convoluted.

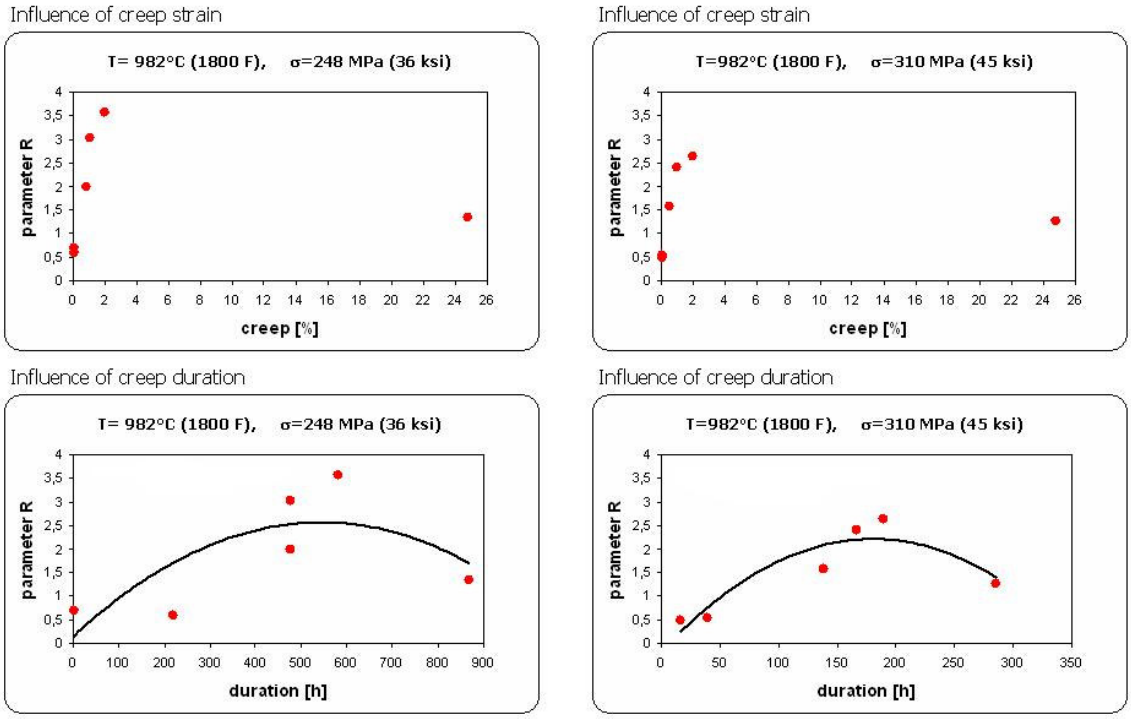

Fig. 68. Evolution of the microstructural parameter **R = L / 2T**. The rafting parameter R reaches the maximum for the highest L values, then subsequently decreases at higher creep strain as coarsening of rafted microstructure proceeds and the rafts become more wavy and convoluted.

3. Comparison of the creep induced microstructural changes for 2nd and 4th generation superalloys

The goal of this chapter is to compare and clearly analyse the microstructural stability of the second (PWA 1484) and fourth (PWA1497) generation superalloys. The detailed results of the microstructure evolution for each generation of the superalloys have already been presented and discussed in the previous chapters (Chapter III - 1 and Chapter III - 2).

3.1 Comparison of superalloys creep tested under the same conditions

The creep strain curves of the PWA 1484 and the PWA 1497 superalloys deformed under the same conditions (982 ˚C and 248 MPa) are presented in Fig. 69. The diagram shows that the PWA 1497 superalloy exhibits nearly three times better creep rupture life than the PWA 1484. The reason for this behaviour is its higher microstructural stability.

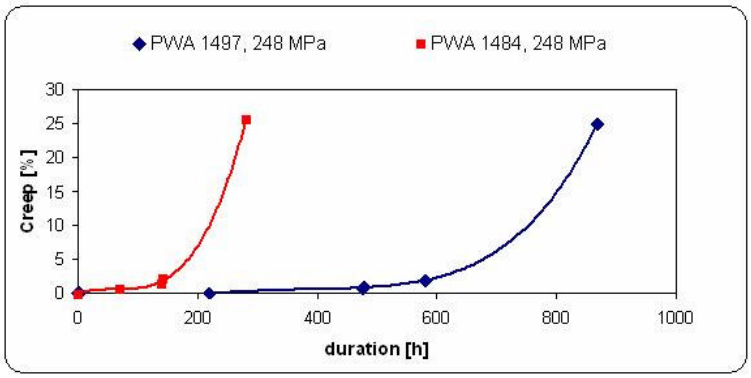

Fig. 69. Creep curves of PWA 1484 and PWA 1497 superalloys, deformed at 980 ˚C and 250 MPa. The PWA 1497 exhibits nearly three time better creep rupture life than the PWA 1484.

The results of the microstructure investigation of both superalloys creep tested under the same conditions (982 ˚C and 248 MPa) are also compared and plotted as a function of creep duration. Figs 70-73 show the evolutions of the **S**, **T**, **L** and **R** parameters. The trend line on each curve was fitted as a second-degree polynomial.

The results obtained for each parameter show a similar tendency for both superalloys, but in all cases the rate of microstructural changes is significantly slower for 4th generation PWA 1497 superalloy than for PWA 1484 superalloy. This indicates that the PWA 1497 exhibits higher microstructural stability than the PWA 1484 superalloy.

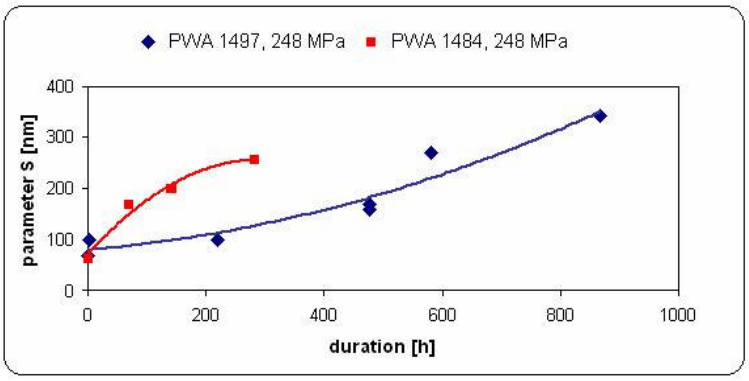

Fig. 70. The **S** parameter as a function of creep duration at 982 ˚C and 248 MPa for 2nd (PWA 1484) and 4th (PWA 1497) generation superalloys. The tendency for both superalloys is similar but the mean spacing of γ phase increases faster for PWA 1484 superalloy

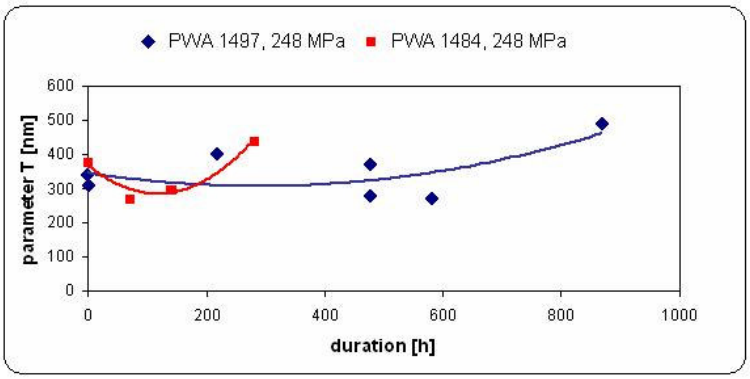

Fig. 71. The **T** parameter as a function of creep duration at 982 ˚C and 248 MPa for 2nd (PWA 1484) and 4th (PWA 1497) generation superalloys. The tendency for both superalloys is similar but the mean thickness of γ' phase increases faster for PWA 1484 superalloy

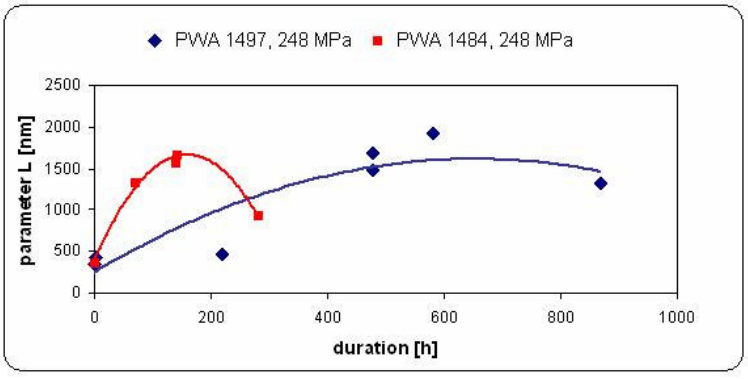

Fig. 72. The **L** parameter as a function of creep duration at 982 ˚C and 248 MPa for 2nd (PWA 1484) and 4th (PWA 1497) generation superalloys. The tendency for both superalloys is similar but the mean length of γ/γ' interface boundary increases and subsequently decreases faster for PWA 1484 superalloy

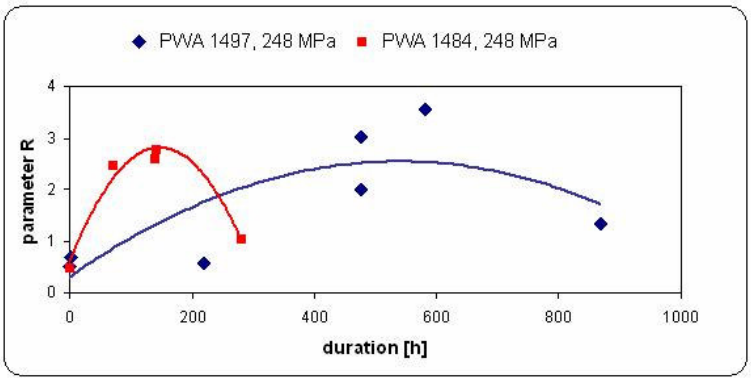

Fig. 73. The rafting parameter **R** as a function of creep duration at 982 ˚C and 248 MPa for 2nd (PWA 1484) and 4th (PWA 1497) generation alloys. The tendency for both superalloys is similar but the rafting parameter (R = L/2T) increases and subsequently decrees faster for PWA 1484 superalloy.

3.2 Comparison of superalloys creep tested at different stresses

The comparison of microstructure stability of both superalloys, creep tested at different stress, confirmed that the creep strength of 4th generation PWA 1497 is higher than that of 2nd generation PWA 1484 superalloy.

The creep diagram of the PWA 1484 and the PWA 1497 superalloys, deformed at the same temperature 982 ˚C but with different stress, are presented on Fig. 74. The creep curves for both alloys tested with different stresses are clearly comparable. The PWA 1497 can withstand around 60 MPa higher stresses during creep tests than PWA 1484, maintaining at the same time closely similar rate of creep strain.

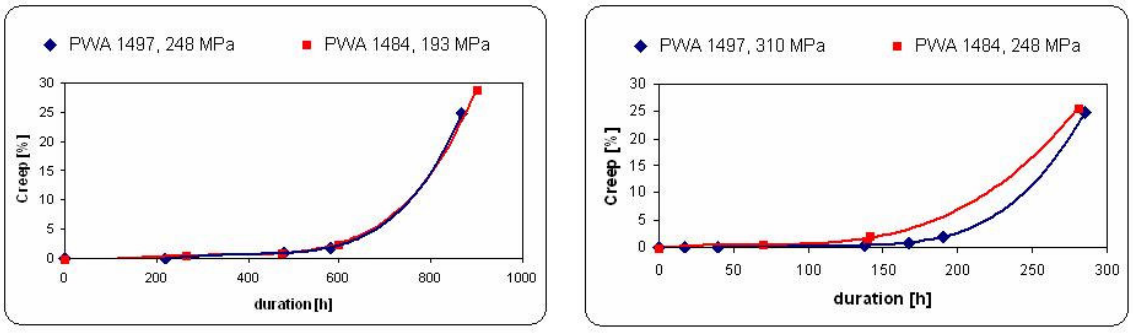

Fig. 74. Creep curves of the PWA 1484 and the PWA 1497 superalloys, deformed at 982 ˚C and various stresses: 248 MPa for PWA 1497 and 193 MPa for PWA 1484 (left column), 310 MPa for PWA 1497 and 248 MPa for PWA 1484 (right column). Creep curves for both alloys tested with different stresses are clearly comparable. PWA 1497 can withstand around 60 MPa higher stresses during creep tests than PWA 1484.

The results of microstructure evolution of both superalloys, creep tested at the same temperature (982 ˚C) but at different stress were also compared and plotted as a function of creep duration. The evolutions of **S**, **T**, **L** and **R** parameters are shown on Figs 75-78. The trend line on each curve was fitted as a second-degree polynomial.

The results of particular parameter are in good agreement for both superalloys. The PWA 1497 superalloy can endure in 980 ˚C about 60 MPa higher stress than PWA 1484 superalloy, maintaining at the same time similar microstructure changes.

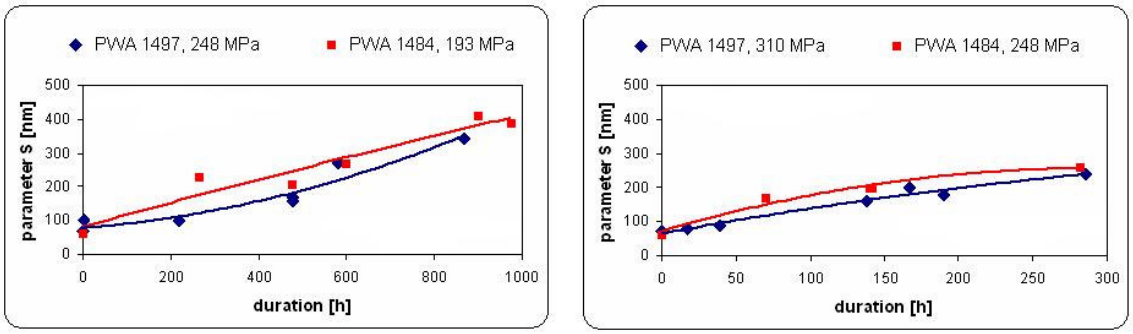

Fig. 75. **S** parameter as a function of creep duration at 982 ˚C and varies stresses: 248 MPa for PWA 1497 and 193 MPa for PWA 1484 (left column), 310 MPa for PWA 1497 and 248 MPa for PWA 1484 (right column). The mean spacing of γ phase increases very similarly for both superalloys. PWA 1497 can withstand around 60 MPa higher stress during creep tests than PWA 1484.

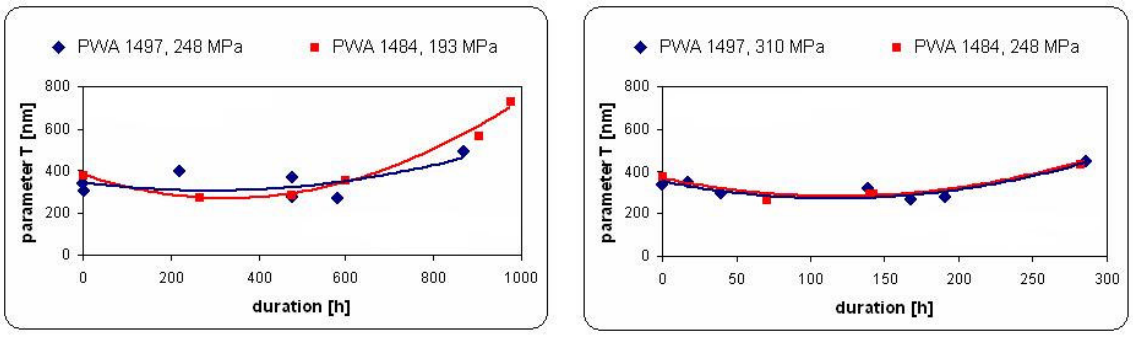

Fig. 76. **T** parameter as a function of creep duration at 982 ˚C and varies stresses: 248 MPa for PWA 1497 and 193 MPa for PWA 1484 (left column), 310 MPa for PWA 1497 and 248 MPa for PWA 1484 (right column). The mean thickness of γ' phase undergoes very similar changes for both superalloys. PWA 1497 can withstand around 60 MPa higher stress during creep tests than PWA 1484.

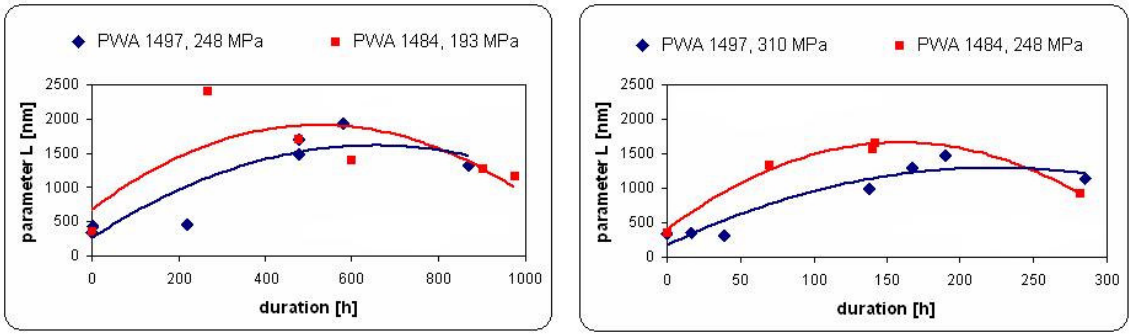

Fig. 77. The **L** parameter as a function of creep duration at 982 ˚C and various stresses: 248 MPa for PWA 1497 and 193 MPa for PWA 1484 (left column), 310 MPa for PWA 1497 and 248 MPa for PWA 1484 (right column). The mean length of γ/γ' interface boundary undergoes very similar changes for both superalloys (first increases and then subsequently decreases). PWA 1497 can withstand around 60 MPa higher stress during creep tests than PWA 1484.

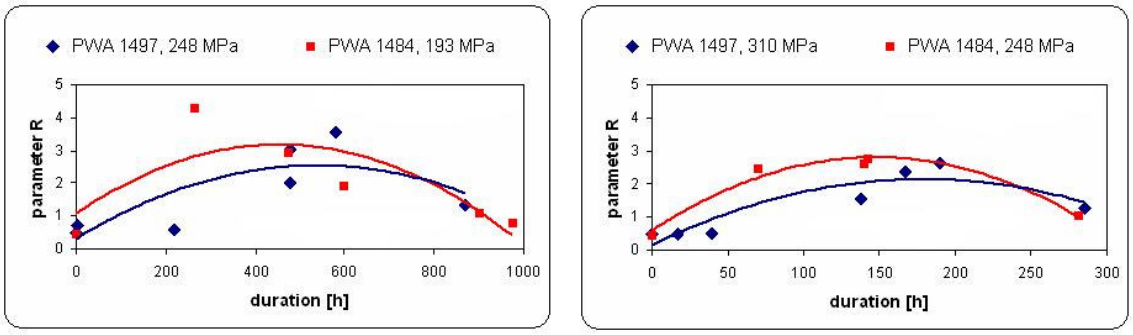

Fig. 78. The **R** parameter as a function of creep duration at 982 ˚C and varies stresses: 248 MPa for PWA 1497 and 193 MPa for PWA 1484 (left column), 310 MPa for PWA 1497 and 248 MPa for PWA 1484 (right column). The rafting parameter (R = L/2T) undergoes very similar changes for both superalloys (first increases and then subsequently decreases). PWA 1497 can stand around 60 MPa higher stress during creep tests than PWA 1484.

4. High temperature microstructural stability of both superalloys during ageing

Ageing tests were performed on the samples taken from both generation superalloys, PWA 1484 and PWA 1497. The samples used for ageing experiment were taken from different castings than those for creep testing specimens. The aim of the experiment was to investigate high temperature microstructural stability of both superalloys without external stresses and compare the results with those of creep deformed samples.

Four samples of each superalloy were isothermally aged at temperature 980 ℃ for 225, 450, 675 and 900 hours (it means with increasing time of exposure of 225 h step). Figs 79 and 80 present SEM micrographs showing microstructure evolution during ageing of the PWA 1484 and the PWA 1497 superalloys, respectively.

The 2nd generation superalloy, PWA 1484, characterizes the following microstructural changes. After ageing for 225 h, there are no visible changes in alloy microstructure in comparison with the baseline sample (labelled as: BM – 0 h). Further, after 450 h of ageing, coagulation of the γ' phase is observed, γ' particles become clearly larger and they start to group together to form short chains and blocks. Moreover widening of γ matrix channels is observed. The next 225 h of ageing leads to further particle coagulation. After 900 h of ageing γ' particles still undergo further coagulation; γ' particles distinctly start to lose their cuboidal shape, coalescing in larger extended blocks.

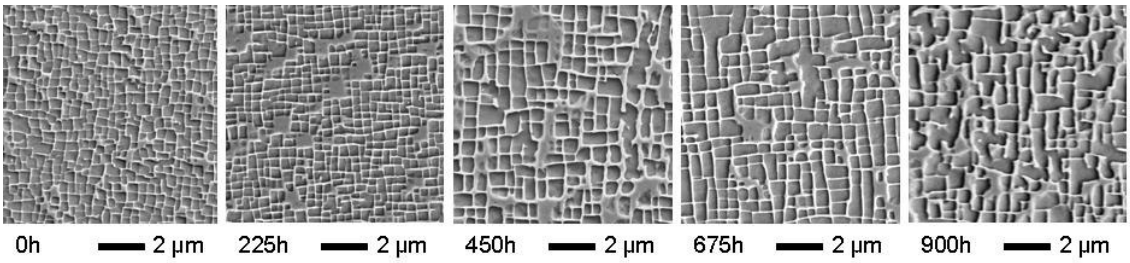

Fig. 79. PWA 1484 superalloy microstructure evolution during ageing tests at 980 ℃ up to 900 h, showing coagulation of γ' particles and loss of cuboidal shape

The 4th generation superalloy, PWA 1497, after 225 h of ageing demonstrates no microstructural changes and the microstructure is similar to that of the baseline sample (BM – 0 h). After consecutive ageing for 225 and 450 h, due to coagulation process, a slight increase in γ' particle size and a widening of the γ matrix channels are observed. Finally, 900 h of ageing leads to further coagulation, but larger, blocky γ' particles maintain their cuboidal shape.

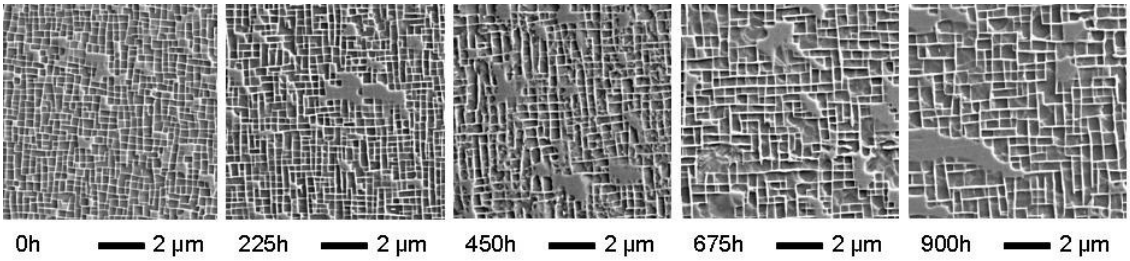

Fig. 80. PWA 1497 superalloy microstructure evolution during isothermal ageing at 980 ℃ up to 900 h, showing coagulation of γ' particles but retaining the in cuboidal shape

The microstructure evolution of both superalloys during ageing was quantitatively characterized using four parameters including: **D** – the mean size of γ' particles (calculated as equivalent circle diameter), **S** – the mean γ channel width, and two parameters describing shape of γ' particles: **k** – shape coefficient (the maximum ratio of width and height of a bounding rectangle for the particle) and **Sphericity** (describing the sphericity or roundness of the particle by using central moments). The parameters and procedure of calculation have already been described in detail in Chapter III – 9.1. The calculated microstructural parameters with their standard deviations are given in Tables 14 and 15 for the PWA 1484 and the PWA 1497 superalloys, respectively.

Tab. 14. Evolution of microstructural parameters during ageing test of PWA 1484

PWA 1484 SUPERALLOY (AGEING AT 980 °C)									
No	Test duration [h]	D [nm]	Δ [nm]	S [nm]	Δ [nm]	k	Δ	Sphericity	Δ
BM*	0	580	±90	63	±20	1.26	±0.22	0.67	±0.17
1	225	570	±90	72	±20	1.29	±0.31	0.68	±0.23
2	450	690	±190	124	±50	1.46	±0.49	0.59	±0.27
3	675	850	±340	130	±80	1.51	±0.48	0.54	±0.26
4	900	1010	±430	190	±90	1.59	±0.44	0.46	±0.24

* Baseline material

Tab. 15. Evolution of microstructural parameters during ageing test of PWA 1497

PWA 1497 SUPERALLOY (AGEING AT 980 °C)									
No	Test duration [h]	D [nm]	Δ [nm]	S [nm]	Δ [nm]	k	Δ	Sphericity	Δ
BM*	0	430	±100	68	±30	1.42	±0.38	0.58	±0.25
1	225	460	±120	82	±35	1.49	±0.51	0.57	±0.27
2	450	520	±110	82	±35	1.49	±0.42	0.54	±0.26
3	675	560	±130	96	±40	1.55	±0.39	0.50	±0.25
4	900	590	±210	94	±40	1.54	±0.47	0.52	±0.25

* Baseline material

The results of microstructure evolution of both superalloys during isothermal ageing tests at 980 ℃ were also plotted as a function of ageing duration up to 900 h. For easier comparison, plots were arranged in two columns. Left column represents 2nd generation PWA 1484 superalloy and right column - 4th generation PWA 1497 superalloy.

The evolution of parameters **D** and **S** are shown in Figs 81 and 82. The shape coefficient (**k**) and **sphericity** are presented on Figs 83 and 84.

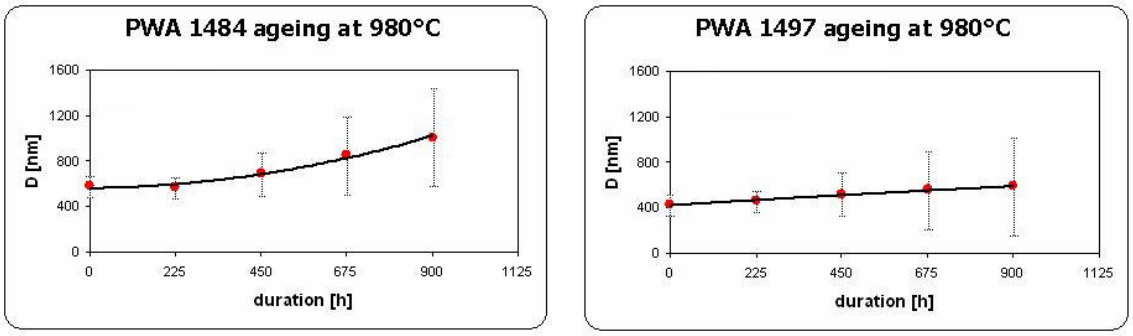

Fig. 81. Evolution of the microstructural parameter: **D** for PWA 1484 (left column) and PWA 1497 (right column) during ageing. The mean size of γ' particles increases for both superalloys due to their coagulation. PWA 1497 superalloy is characterized by distinctly slower rate of γ' particle coagulation.

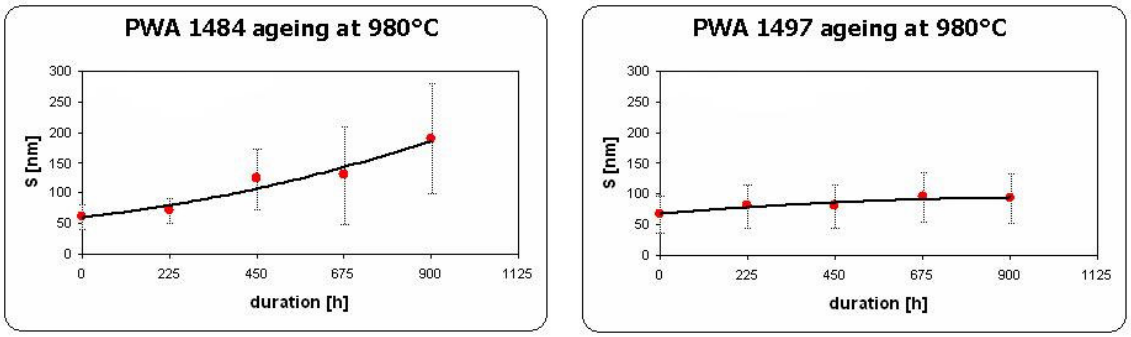

Fig. 82. Evolution of the microstructural parameter: **S** for PWA 1484 (left column) and PWA 1497 (right column) during ageing. The mean γ channel width increases for both superalloys due to γ' coagulation. PWA 1497 superalloy is characterized by distinctly slower rate of γ channels widening.

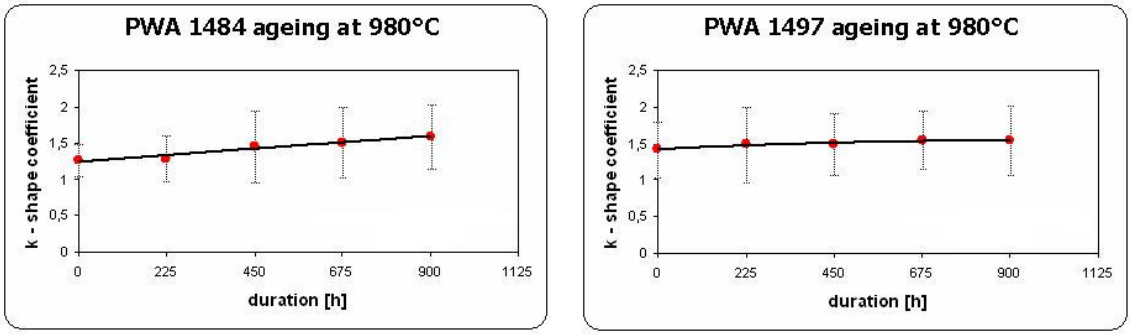

Fig. 83. Evolution of the microstructural parameter: **k** for PWA 1484 (left column) and PWA 1497 (right column) during ageing. The mean shape coefficient of γ' particles slowly increases for both superalloys but for PWA 1497 changes are significantly smaller.

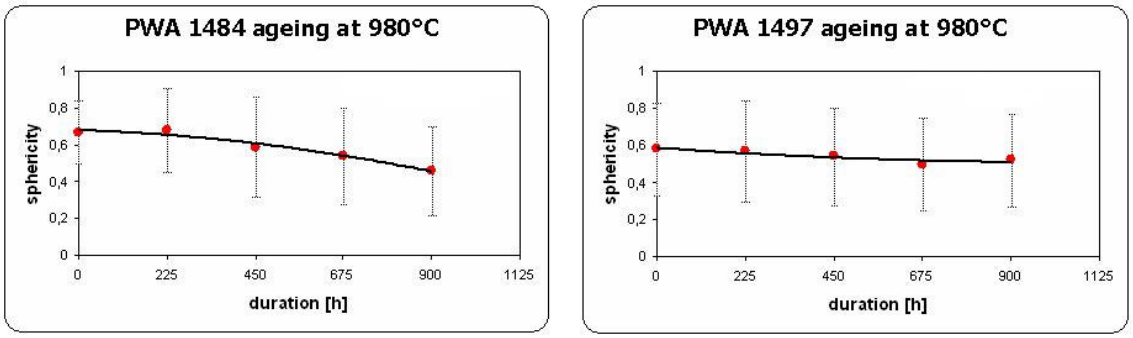

Fig. 84. Evolution of γ' particle **Sphericity** for PWA 1484 (left column) and PWA 1497 (right column) during ageing. The mean sphericity of γ' particles decreases for both superalloys but for PWA 1497 changes are significantly smaller.

The mean size of γ' particles (**D**) increases during ageing for both superalloys due to particle coagulation, but for the PWA 1497 superalloy, the rate of change is slower and the size of γ' particles is much smaller. After ageing for 900 h, the γ' particles in PWA 1484 superalloy reach almost twice the size of the γ' particles in PWA 1497.

Similar situation concerns mean γ channel width (**S**) of both superalloys. The PWA 1497 superalloy has a distinctly lower rate of γ channel widening, reaching only half of the mean dimension of γ channels of PWA 1484 at the end of ageing test.

The shape coefficient (**k**) of γ' particles slowly increases for both superalloys with the prolongation of ageing test duration due to particle coagulation processes. For the PWA 1497 superalloy changes in the γ' particle shape coefficient are significantly smaller than for the PWA 484 because γ' particles retain their cuboidal shape during growth and coagulation.

The second parameter which describes a shape evolution of γ' particles (**Sphericity),** decreases for both superalloys as the γ' particles become more extended and start to lose their cuboidal shape. However, γ' particles in the PWA 1497 superalloy retain the cuboidal shape for longer time than PWA 1484 so that the decrease in sphericity of the γ' particles in the PWA 1497 occurs more slowly.

The quantitative results obtained for both superalloys show a similar tendency but with significant differences in the rate of alloy microstructure evolution. The 4th generation PWA 1497 superalloy subjected to isothermal ageing test at 980 ℃ up to 900 h exhibits a considerably more stable microstructure than the 2nd generation PWA 1484 superalloy tested under the same conditions. The direct reason of this effect is the difference in chemical composition of both superalloys, which influences the γ/γ' misfit. The PWA 1497 superalloy is characterized by more negative γ-γ' misfit at room temperature than that of the PWA 1484 superalloy (see Chapter IV – 5). The γ/γ' misfit introduces internal stresses into alloy microstructure. During ageing γ' particles tend to minimize misfit stresses and undergo coalescence to reduce the interfacial area. New rearrangement of γ' particles widens the matrix channels, facilitating dislocation movement. Finally, the γ' particles loose coherence with the matrix γ [17].

The higher microstructural stability of the PWA 1497 superalloy during ageing might be explained by longer time needed for relaxation of internal stresses because of the more negative γ/γ' misfit. Coagulation and coalescence of γ' particles while maintaining their cuboidal shape after long-term ageing of the PWA 1497 superalloy is the most convincing evidence supporting this hypothesis.

5. The γ/γ' misfit measurements by X-ray diffractometry

The XRD measurements of γ/γ' misfit, calculated as $\delta = 2 \times (a_{\gamma'} - a_{\gamma})/(a_{\gamma'} + a_{\gamma})$ were performed at room temperature on baseline samples of PWA 1484 and PWA 1497 superalloys.

The measured lattice parameters of γ and γ' phase (a_{γ} and $a_{\gamma'}$) and γ-γ' misfit (δ) as well as the chemical composition is shown in Table 16.

Table 16. The lattice parameters of the γ and γ' phase and γ-γ' misfit (δ) of the PWA 1484 and the PWA 1497 with chemical composition of both superalloys (Ni-bal., wt %)

Alloy	a_{γ} [nm]	$a_{\gamma'}$ [nm]	δ [%]	Cr	Co	Mo	Re	Ru	W	Al	Ta	Hf
PWA 1484	0.35899	0.35857	-0.12	5	10	2	3	-	6	5.6	8.7	0.1
PWA 1497	0.36086	0.36003	-0.26	2	16.5	2	5.95	3	6	5.55	8.25	0.15

The results of γ/γ' misfit (δ) measurements reveal that both baseline samples possess at room temperature a negative lattice misfit varying between -0.12 % for 2nd generation PWA 1484 superalloy and -0.26 % for 4th generation PWA 1497 superalloy. The lattice parameters of the γ' and γ phases ($a_{\gamma'}$ and a_{γ}, respectively) are higher for the PWA 1497 superalloy and for both superalloys a_{γ} is higher than $a_{\gamma'}$. The difference between the lattice parameters (a_{γ}) and ($a_{\gamma'}$) is significantly greater (almost double) for PWA 1497 (0.00083 nm) than for PWA 1484 (0.00042 nm).

This result can be explained by a difference in alloy compositions, especially the rhenium (Re) content. The Re content of PWA 1497 superalloy (Re = 5.95%) is twice that of PWA 1484 (Re = 3.0%). Rhenium is known to partition preferentially to the γ phase and change its lattice parameter [59]. Moreover, PWA 1497 superalloy contains addition of 3% of ruthenium (Ru), which also increases the lattice parameter of γ phase significantly, but also increases the γ' phase lattice parameter slightly. The tendency of ruthenium to partition to the γ phase is not as pronounced as for rhenium. Ruthenium is also responsible for reverse partitioning effect, which has been reported for some superalloys containing this element [60-63]. The reverse partitioning effect would slightly lower the rhenium content in the γ matrix and increase it in the γ' phase with corresponding effects on the lattice parameters [59].

6. Nanoindentation hardness measurements by Atomic Force Microscopy

NI-AFM hardness investigation of the γ and γ' phases were performed on both superalloys, PWA 1484 and PWA 1497.

Figures 85-88 show PWA 1484 surface topography revealed by AFM, before and after nano-hardness measurements and Figs 89-92 those of PWA 1497 superalloy. Ten indents for each phase (γ and γ') were performed for each sample. Scan size for each AFM micrograph is 10 μm x 10 μm. Brighter colour indicates γ matrix phase and γ' phase precipitates are represented by darker shade, the contrast is obtained due to differences in height on the surface of the samples which are caused by difference in nano-hardness of the phases.

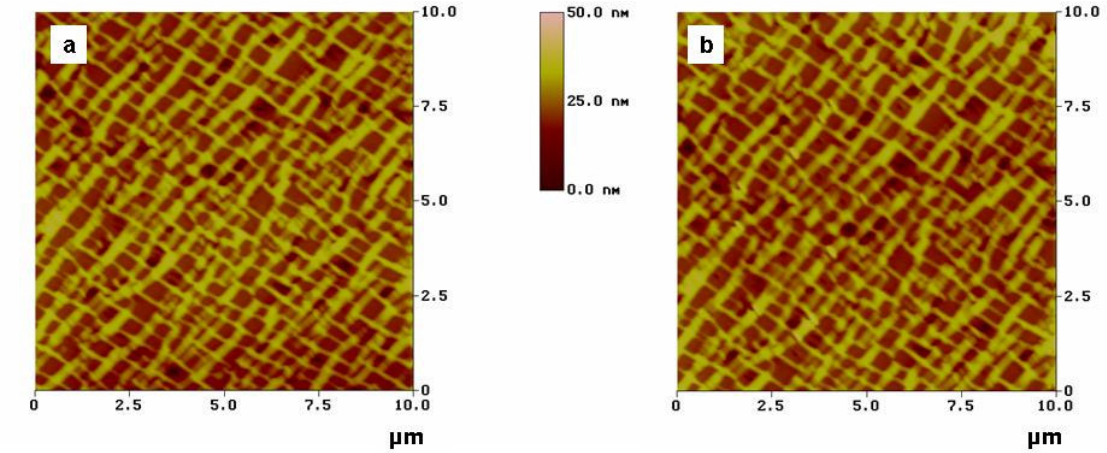

Fig. 85. PWA 1484 superalloy, baseline material: surface topography before (a) and after (b) NI-AFM tests (indents in γ and γ' phases are visible) revealed by AFM

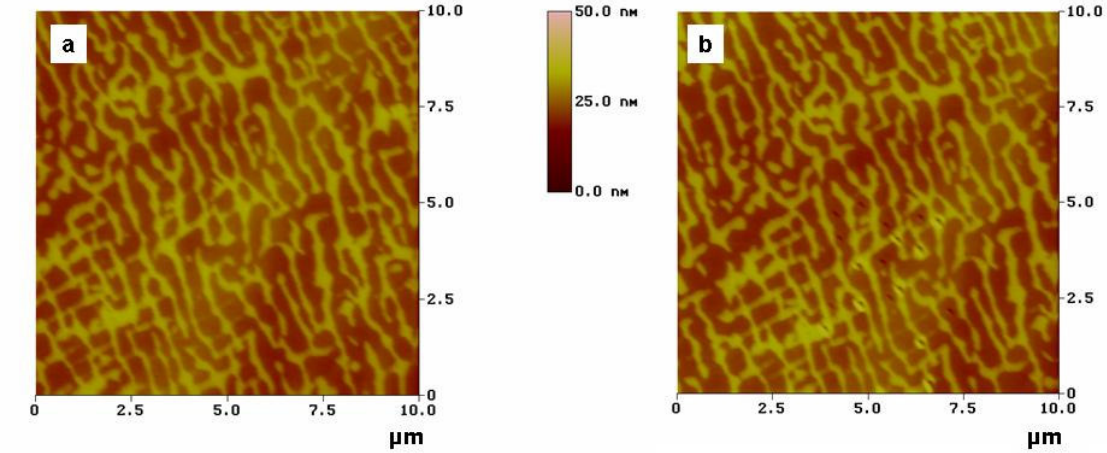

Fig. 86. PWA 1484 superalloy, sample no. 5: surface topography before (a) and after (b) NI-AFM tests (indents in γ and γ' phases are visible) revealed by AFM

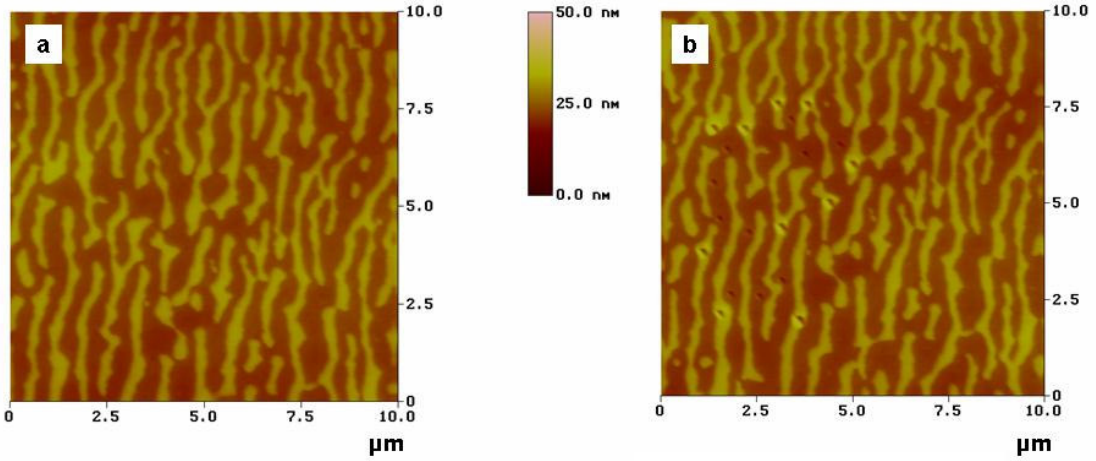

Fig. 87. PWA 1484 superalloy, sample no. 6: surface topography before (a) and after (b) NI-AFM tests (indents in γ and γ' phases are visible) revealed by AFM

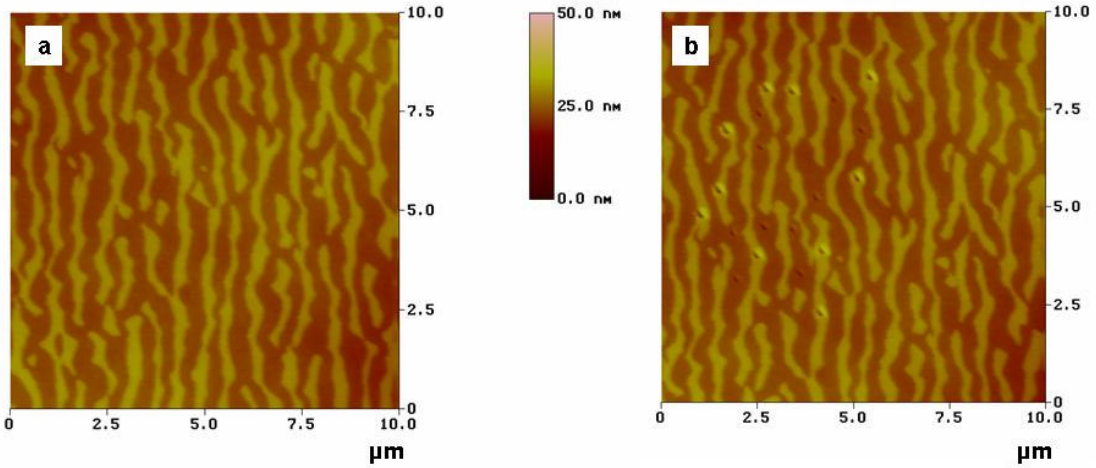

Fig. 88. PWA 1484 superalloy, sample no. 2: surface topography before (a) and after (b) NI-AFM tests (indents in γ and γ' phases are visible) revealed by AFM

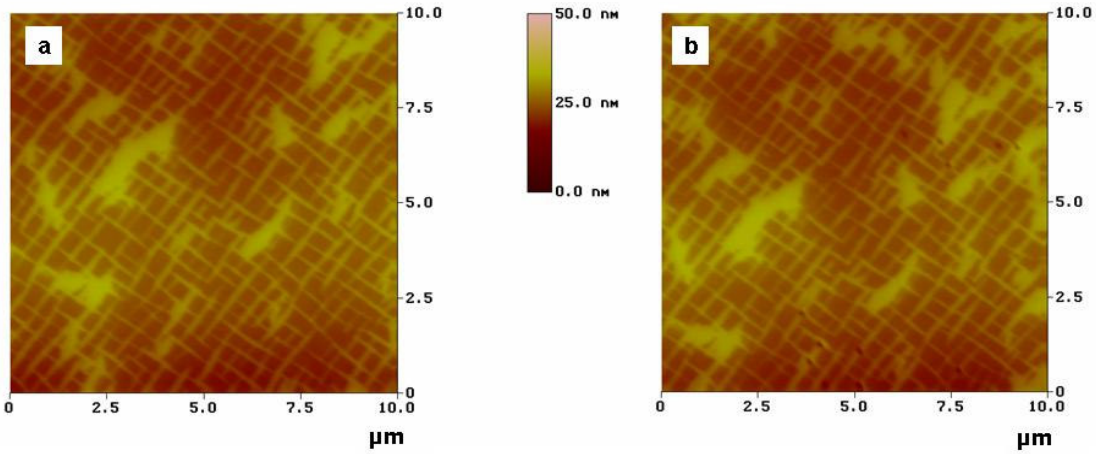

Fig. 89. PWA 1497 superalloy, baseline material: surface topography before (a) and after (b) NI-AFM tests (indents in γ and γ' phases are visible) revealed by AFM

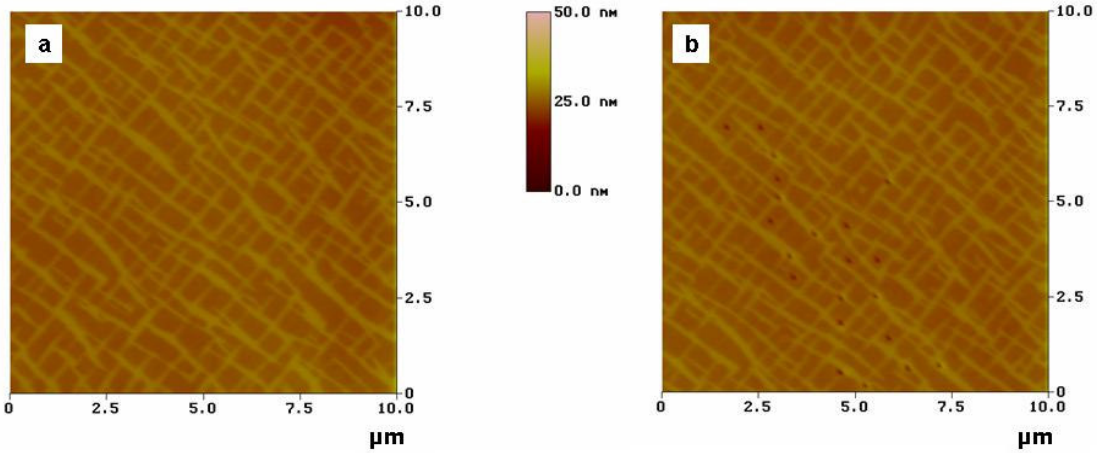

Fig. 90. PWA 1497 superalloy, sample no. 8: surface topography before (a) and after (b) NI-AFM tests (indents in γ and γ' phases are visible) revealed by AFM

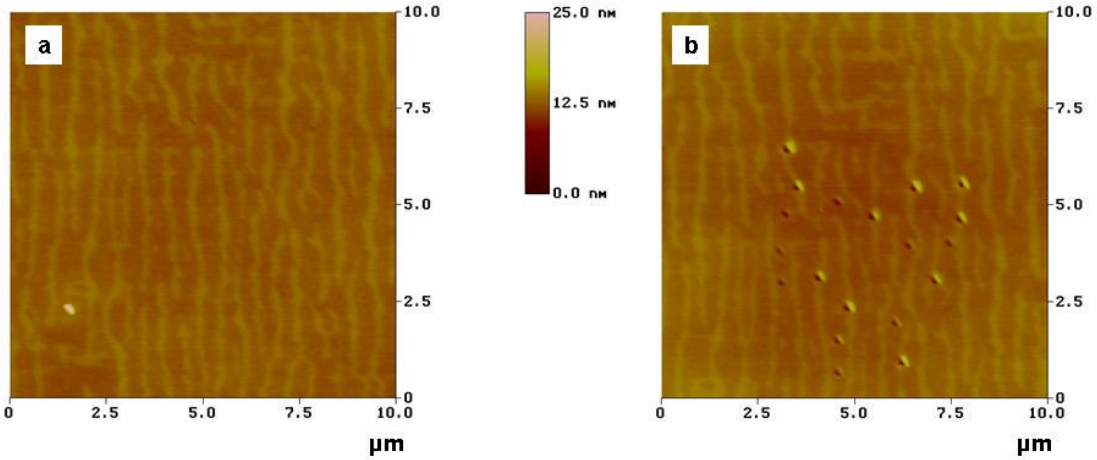

Fig. 91. PWA 1497 superalloy, sample no. 10: surface topography before (a) and after (b) NI-AFM tests (indents in γ and γ' phases are visible) revealed by AFM

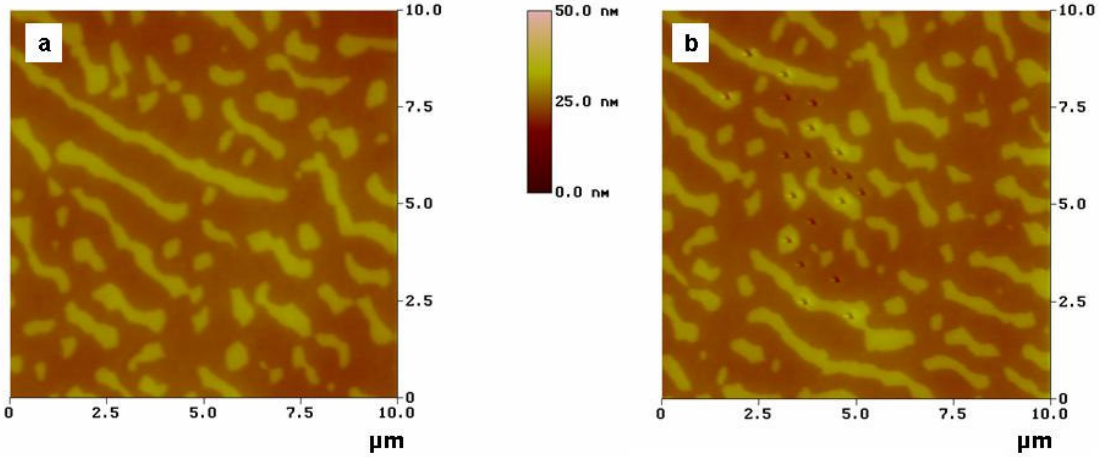

Fig. 92. PWA 1497 superalloy, sample no. 2: surface topography before (a) and after (b) NI-AFM tests (indents in γ and γ' phases are visible) revealed by AFM

The accurate nanohardness measurement results (with standard deviation) for each sample are shown in Table 17 for the PWA 1484 and Table 18 for the PWA 1497 superalloys.

Table 17. NI-AFM hardness measurements of γ and γ' phases in the PWA 1484 superalloy

PWA 1484 superalloy								
Creep samples conditions					**γ phase**		**γ' phase**	
No	Temp. [℃]	Stress [MPa]	Strain [%]	Time [h]	Hardness [GPa]	Δ [GPa]	Hardness [GPa]	Δ [GPa]
BM*	-	-	-	-	**6.83**	±0.26	**10.38**	±0.66
5	982	248	0.714	69.7	**8.22**	±0.54	**10.40**	±0.22
6	982	248	1.465	139.4	**7.04**	±0.39	**10.11**	±0.70
2	982	248	25.633	280.7	**7.50**	±0.32	**10.14**	±0.31

* Baseline material

Table 18. NI-AFM hardness measurements of γ and γ' phases in the PWA 1497 superalloy

PWA 1497 superalloy								
Creep samples conditions					**γ phase**		**γ' phase**	
No	Temp. [℃]	Stress [MPa]	Strain [%]	Time [h]	Hardness [GPa]	Δ [GPa]	Hardness [GPa]	Δ [GPa]
BM*	-	-	-	-	**8.76**	±0.50	**9.96**	±0.40
8	982	248	0.05	1.58	**9.01**	±0.50	**10.61**	±0.97
10	982	248	0.849	477.17	**7.54**	±0.49	**10.62**	±0.54
2	982	248	24.793	867.41	**7.80**	±0.30	**8.90**	±0.43

* Baseline material

Fig. 93 shows nanohardness of the γ and γ' phases in four PWA 1484 samples and Fig. 94 of the PWA 1497 superalloy for different creep strain.

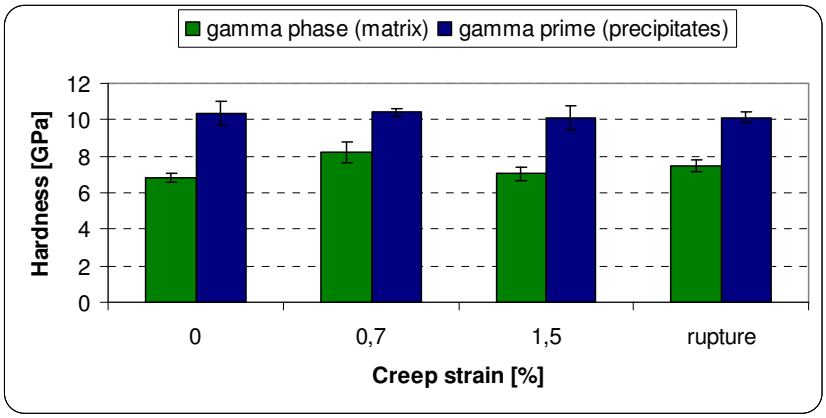

Fig. 93. PWA 1484 superalloy, comparison of γ and γ' phase nanohardness for different creep strain

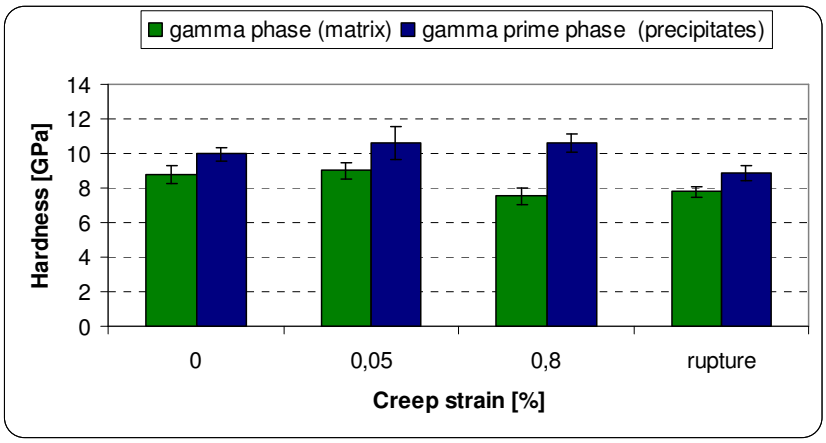

Fig. 94. PWA 1497 superalloy, comparison of γ and γ' phase nanohardness for different creep strain

The comparison of the mean nanohardness of both phases precipitated in both superalloys show that the γ' phase is always harder than the γ matrix phase. There is no tendency or clear difference in the nanohardness of γ and γ' phases in the samples after different creep deformation of both superalloys. This means that the nanohardness does not change with increasing creep strain or that the hardness changes are very small, therefore beyond a resolution of applied measurement technique.

The hardness of the γ' precipitates in the PWA 1484 superalloy is slightly higher than the nanohardness of the γ' phase of PWA 1497. The reason is most probably due to a difference in alloy chemical composition; the PWA 1497 contains less Ta which act as a strengthening element for γ' phase. The γ matrix of the PWA 1497 superalloy is on average 0.8 GPa harder than that of the PWA 1484, that might be explained by higher content of Re and Ru, since they partition predominantly to the matrix phase.

The higher stability of 4th generation superalloy PWA 1497 is related to significantly stronger solid solution strengthening, what results in higher hardness of γ matrix in comparison with that of second generation PWA 1484 superalloy.

7. Focused Ion Beam tomography of 4th generation PWA 1497 superalloy

FIB tomography of the γ and γ' phases was performed on two samples; baseline and after creep rupture test of 4th generation PWA 1497 superalloy. Three dimensional reconstruction of γ-γ' microstructure for the baseline sample is shown on Fig. 95 and for ruptured sample on Fig. 96. The procedure of 3D reconstruction have already been described in details in Chapter III - 10.

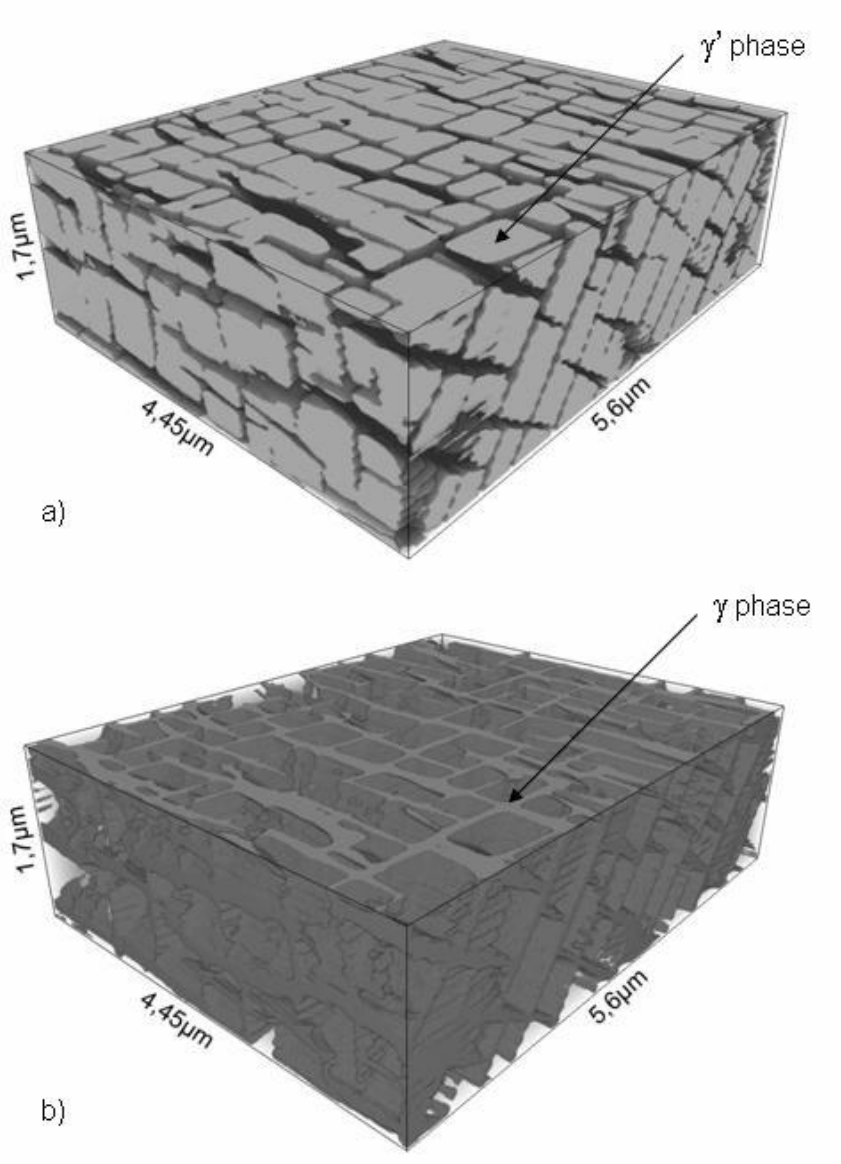

Fig. 95. PWA 1497 baseline material, 3D reconstruction showing: a) regular cuboidal morphology of γ' particles, b) γ channels

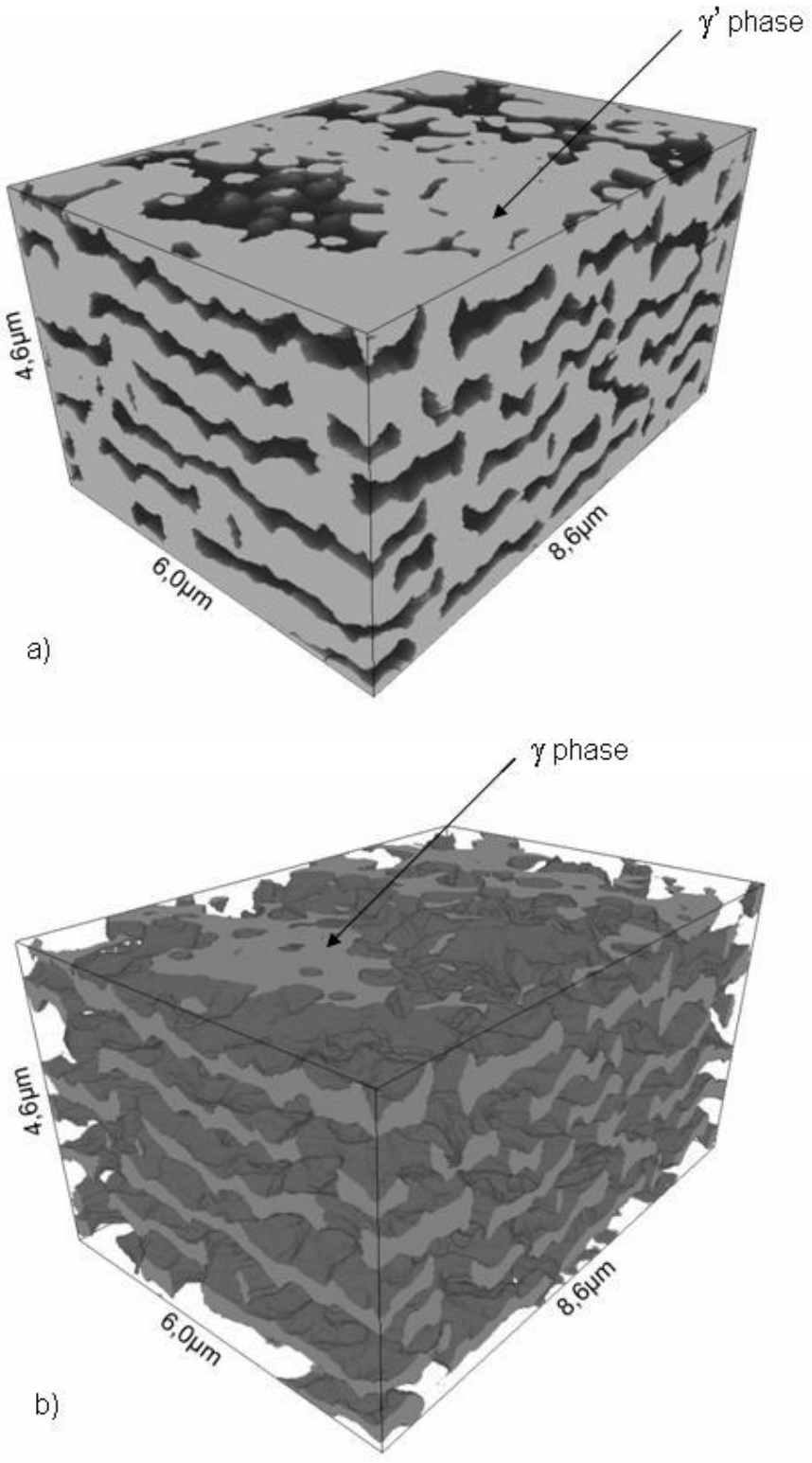

Fig. 96. PWA 1497, sample no 2 crept at 982 °C/248 MPa (ruptured), creep strain 25%, duration 870 h, 3D reconstruction showing the final stage of the rafting process-microstructural inversion: a) γ' phase becoming topologically the matrix, b) γ phase looks like the precipitates.

Based on 3D reconstruction of baseline sample the γ' phase surface fraction (f_s) was measured as 70% and the volume fraction (V_v) as 69%. The surface fraction (f_s) for sample no 2 was measured as 75% and volume fraction (V_v) as 74%. The results are in good agreement with TEM investigation of baseline sample and clearly prove that in case of the superalloys, measurements of surface fraction are adequate for volume fraction ($f_s \cong V_v$).

V. SUMMARY AND DISCUSSION

V.1. The baseline materials

The results of TEM microstructure analysis of baseline material of 2nd generation PWA 1484 and 4th generation PWA 1497 superalloys reveal that both superalloys posses regular cuboidal morphology of γ' particles separated by γ channels.

The results of quantitative microstructural analysis show similar values of microstructural parameters for both baseline superalloys. The mean dimension of γ' particles (**D**) was similar for both generations superalloys, however slightly higher for PWA 1484 (447 nm) than for PWA 1497 (442 nm), while the mean width (**S**) of γ channels was higher for PWA 1497 (70 nm) than for PWA 1484 (63 nm).

The volume fraction ($\mathbf{V_v}$) of γ' phase was higher for PWA 1484 (79%) than for PWA 1497 superalloy (72%). The results of γ' phase volume fraction (69%) for PWA 1497 were also confirmed by FIB tomography.

The γ' phase volume fraction in modern single crystal superalloys is about 70 to 80%. This is apparently the optimum value, however the γ' volume fraction for 2nd generation SC superalloys CMSX-4 has been reported by various authors in the range between 65% and 77% [64-67] and for 69% for MC2 superalloy [68]. In the case of 4rth generation SC superalloy TMS-138 the γ' volume fraction was reported as 60% [69, 70].

The microstructure of the superalloys strongly determines their mechanical properties. The volume fraction, size distribution, and shape of γ' precipitates can be optimized by composition design and heat treatment. The difference in γ' volume fraction as well as γ and γ' phase parameters between both superalloys is most probably caused by difference in chemical composition and heat treatment of both generation superalloys.

<u>The γ/γ' misfit</u>

The results of γ/γ' (δ) misfit measurements reveal that both baseline samples possess at room temperature a negative lattice misfit varying between -0.12% for 2nd generation PWA 1484 superalloy and -0.26% for 4th generation PWA 1497 superalloy. The lattice parameters of the γ' and γ phases ($a_{\gamma'}$ and a_{γ}, respectively) are higher for PWA 1497 superalloy and for both superalloys a_{γ} is higher than $a_{\gamma'}$. The difference between the lattice parameters (a_{γ}) and ($a_{\gamma'}$) is significantly greater (almost double) for PWA 1497 (0.00083 nm) than for PWA 1484 (0.00042 nm).

This result can be explained by a difference in superalloy composition, especially the rhenium (Re) content. The rhenium content of PWA 1497 superalloy (Re = 5.95%) is twice that of PWA 1484 (Re = 3.0%). Rhenium is known to partition preferentially to the γ phase and changes its lattice parameter [59]. Moreover, the PWA 1497 superalloy contains addition of 3% of ruthenium (Ru), which also increases the lattice parameter of γ phase significantly, but also increases the γ' phase lattice parameter slightly. The tendency of ruthenium to partition to the γ phase is not as pronounced as for rhenium. Ruthenium is also responsible for so-called "reverse partitioning effect", which has been reported for some superalloys containing this element [60-63]. According to Pyczak et at. [59], the reverse partitioning effect would slightly lower the rhenium content in the γ matrix and increase it in the γ' phase with corresponding effects on the lattice parameters.

The γ-γ' nanohardness

The comparison of the mean hardness of both phases of each superalloy shows that the precipitates of γ' phase are always harder than the γ matrix phase. This is mainly due to the chemical composition of both phases.

There is no tendency or clear difference in the nanohardness of γ and γ' phase in the samples after different creep deformation of both superalloys. This means that the hardness does not change with increasing creep strain or that the hardness changes are very small, therefore beyond a resolution of applied measurement technique.

The nanohardness of the γ' precipitates of PWA 1484 superalloy is slightly higher than the hardness of the γ' phase of PWA 1497. The reason is probably due to the difference in chemical composition; the PWA 1497 contains less Ta which act as a strengthening element for γ' phase. The γ matrix of the PWA 1497 superalloy is on average 0.8 GPa harder than that of PWA 1484 that might be explained by higher content of Re and Ru, since they partition predominantly to the matrix phase.

Similar result was presented by Durst et al. [44] who compared the hardness of γ and γ' in 1st (CMSX-6), 2nd (CMSX-4) and 3rd (CMSX-10) generation of the superalloys. According to Durst et al. the different generations of nickel-base superalloys clearly show a increased hardness of the γ matrix with a higher concentration of rhenium. No significant difference in the hardness of the γ' precipitates could be found.

The higher stability of 4th generation superalloy PWA 1497 is related to significantly stronger solid solution strengthening, what result in higher hardness of γ matrix in comparison with that of 2nd generation PWA 1484 superalloy. This is because creep deformation is controlled mostly by a dislocation climb in γ phase.

V.2. Microstructural stability of the superalloys during ageing and creep deformation at high temperature

Microstructural stability of both superalloys during isothermal ageing

The results of microstructure investigation after isothermal ageing at 980 ℃ up to 900 h obtained for both superalloys show a similar tendency but with significant differences in a microstructure evolution rate. The 4th generation PWA 1497 superalloy subjected to isothermal ageing at 980° C up to 900 h is characterized by considerably more stable microstructure than that of 2nd generation PWA 1484 superalloy tested in the same conditions. The direct reason of this effect is a difference in the chemical composition of both superalloys, which influences the γ/γ' misfit of those superalloys. The PWA 1497 superalloy is characterized by more negative γ/γ' misfit in room temperature than those of the PWA 1484 superalloy. The γ/γ' misfit introduces internal stresses into superalloy microstructure. During ageing, the γ' particles tend to minimize misfit stresses and undergo coalescence to reduce interface area. New rearrangement of γ' particles widens the matrix channels, facilitating dislocation movement. Finally, due to a microstructural evolution, γ' particles lose a coherence with the matrix [17].

Higher microstructural stability of the PWA 1497 superalloy during ageing might be explained by longer time needed for relaxation of internal stresses introduced by more negative γ/γ' misfit. Coagulation of γ' particles with maintaining their cuboidal shape after long-term ageing of the PWA 1497 superalloy is the most pronounced evidence supporting this hypothesis.

Microstructure stability of both superalloys during creep deformation

The evolution of the PWA 1484 and the PWA 1497 superalloy microstructures during creep deformation was characterized quantitatively using four parameters: $\boldsymbol{L}$ – mean length of γ/γ' interface boundary, $\boldsymbol{T}$ – mean thickness of γ' phase, $\boldsymbol{S}$ – mean spacing of γ phase, $\boldsymbol{R}$ – rafting parameter $\boldsymbol{R = L/(2T)}$. The procedure of measurements was adopted after Matan et al. [49].

During primary creep at 982 ℃ of the 2nd generation PWA 1484 superalloy, γ' precipitates start to join together early and continue to develop well into steady-state creep by their increased lateral extension. After about 260 hours (for 193 MPa) and 140 hours (for 248 MPa) of creep testing, the γ' rafts extended completely across both SEM and TEM micrographs from one side to the other even at lower magnifications. Further creep deformation leads to the topological inversion and coarsening of rafted microstructure. This process was described by Epishin et al. [39].

The results obtained for 193 and 248 MPa show the similar tendency. Mean spacing of γ phase *S* increases during the creep process, more then six times for the ruptured specimen (for 193 MPa) in comparison with baseline material and more then four times for 248 MPa.. Evolution of microstructural parameter *T* which represent mean thickness of γ' rafts, shows that *T* parameter increase, reaching the highest value for a topological inversion of a microstructure. The mean length of γ/γ' interface boundary (**L** parameter) decreases as rafting proceeds and the rafts become more wavy and convoluted, it is more visible for longer creep time and lover creep stress. Evolution of microstructural parameter $R = L / 2T$ shows that rafting parameter reach the maximum for the highest *L* values, then subsequently decreases at higher creep strains due to microstructure inversion.

The results obtained during this investigation are in good agreement with work of Matan et al. [49] who investigated the kinetic of rafting in the CMSX-4 (2nd generation) superalloy. However, according to Matan et al., the interpretation of the parameters *L*, *T* and *S* need to be treated with some caution. In the early stages of rafting as the individual particles undergo directional coarsening and coalescence, when the rafts are short and well aligned, the parameters *L* and *T* correspond to the average length and thickness of the γ' phase, respectively. As coarsening of rafted microstructure occure, the rafts become more wavy and convulted, the *L* parameter no longer corresponds exactly to the length of rafts. Nevertheless *L* parameter represents a measure of further degree of rafting. In the final stages of rafting, the γ' becomes the matrix phase, consequently the length of the γ' precipitates is now meaningless quantity [49].

The evolution of 4th generation PWA 1497 superalloy microstructure during creep deformation was characterized quantitatively, exactly in the same manner like for PWA 1484 superalloy. The microstructural changes of PWA 1497 superalloy are qualitatively similar to those of PWA 1484 superalloy described already above.

The results of measured parameters which describe evolution of microstructure of the PWA 1497 superalloy creep tested with stresses 248 and 310 MPa show the similar tendency. Mean spacing of γ phase *S* increases during creep process, triple its value for the ruptured specimen. For low creep strain (below 1%), *T* and *L* parameters have nearly constant values due to a cuboidal shape of γ' precipitates. Increasing of creep strain above ~1% causes the decrease of mean thickness of γ' phase *T*, what is associated with increasing the mean length of γ/γ' interface boundary *L* up to maximum reached for ~2% strain. At higher creep strain, *T* parameter increases, reaching the highest value for the final state of coarsening of rafted microstructure. Mean length of γ/γ' interface boundary *L* decreases as coarsening of rafted microstructure proceeds and the rafts become more wavy and convoluted. Rafting parameter *R* increases at early stages of creep, reach the maximum for the highest *L* values (at ~2% creep strain), then subsequently decreases at higher creep strains. The shape of the *R*(ε) and *R*(t) graphs is quite similar to corresponding *L* graphs due to relatively small changes of *T* parameter.

Comparison of the results of microstructure evolution of both superalloys creep tested at the same conditions (982 ˚C and 248 MPa) shows that the evolution of *S, T, L* and *R* parameter, show a similar tendency for both superalloys, but in all cases the PWA 1497 superalloy exhibits higher microstructural stability than the PWA 1484 superalloy; i.e. the rate of microstructure changes is significantly slower for 4th generation PWA 1497 superalloy.

The results of microstructure evolution of both superalloys, creep tested at the same temperature (982 ˚C) but with different stress were also compared and plotted as a function of creep duration. Evolution of *S, T, L* and *R* parameters shows that each measured parameter is in good agreement for both superalloys. The PWA 1497 superalloy can endure in 982 ˚C about 60 MPa higher stress than PWA 1484 superalloy, maintaining at the same time similar microstructure changes.

V.3. Focused Ion Beam tomography of 4th generation PWA 1497 superalloy

The FIB tomography of the γ and γ' phases was performed as a supplementary investigation (due to new research possibilities) on two samples; baseline and after creep

rapture of 4th generation PWA 1497 superalloy. The aim of this investigation was three dimensional visualization of γ-γ' microstructure of this superalloy.

Based on 3D reconstruction of baseline sample the γ' phase surface fraction (f_s) was measured as 70% and the volume fraction (V_v) as 69%. The surface fraction (f_s) for sample no 2 was measured as 75% and volume fraction (V_v) as 74%. The results are in good agreement with TEM investigation of baseline sample and clearly prove that in case of the superalloys, measurements of surface fraction are adequate for volume fraction ($f_s \cong V_v$). The γ' phase volume fraction of the superalloys was proved to be independent of creep time [71], however results of γ' volume fraction of crept sample was slightly higher than for baseline sample. The difference of γ' volume fraction for PWA 1497 superalloy for a baseline and crept sample was most probably caused by a statistic error (area chosen for investigation).

V.4. Future research perspective

In order to gain a better understanding of the influence of microstructure stability of both superalloys on their creep behaviour, and to obtain three dimensional stereological description of rafting process alternative methods of investigation are foreseen, due to the new research possibilities.

The Small Angle Neutron Scattering (SANS) experiment was already performed on the PWA 1484 superalloy, but the data evaluation is in progress. The data should be complementary to the results of TEM investigation, as the SANS investigation allow to obtain information from large volume of the sample.

Further Focused Ion Beam (FIB) tomography investigation is also foreseen, due to a new possibility for metrology of strengthening particles, namely three dimensional visualization of the γ' particles.

VI. CONCLUSIONS

The application of the superalloys for the most loaded and critical components of jet engines and industrial gas turbines, demand a complex knowledge about their microstructure stability during service.

In the present study, a detailed investigation of of two nickel-base single crystal superalloys, 2nd generation PWA 1484 and 4th generation PWA 1497, was performed in order to estimate stereologically their microstructure evolution and stability during ageing and creep deformation at high temperature.

The following conclusions can be drawn:

1. Baseline microstructure investigation reveal that both superalloys (PWA 1484 and PWA 1497) posses regular cuboidal morphology of γ' particles separated by γ channels. The results of quantitative microstructural analysis show similar values of microstructural parameters for both baseline materials. The mean diameter of γ' particles (**D**) was similar for both generations superalloys, however it was slightly higher for the PWA 1484 (447 nm) than for the PWA 1497 (442 nm), while the mean width of γ channels (**S**) was higher for the PWA 1497 (70 nm) than for the PWA 1484 (63 nm).
The volume fraction of γ' phase ($\mathbf{V_v}$) was higher for the PWA 1484 (79%) than for the PWA 1497 superalloy (72%). The results of γ' phase volume fraction measurements (69%) for the PWA 1497 were also confirmed by Focused Ion Beam (FIB) tomography.

1a. The XRD measurments of γ/γ' misfit reveal that both baseline samples possess at room temperature a negative lattice misfit varying between -0.12% (for 2nd generation PWA 1484 superalloy) and -0.26 (for 4th generation PWA 1497 superalloy). The lattice parameters of the γ' and γ phase ($a_{\gamma'}$) and (a_{γ}) are higher for PWA 1497 superalloy and for both superalloys a_{γ} is higher than $a_{\gamma'}$. The difference between both lattice parameters (a_{γ}) and ($a_{\gamma'}$) is significantly larger (almost double) for PWA 1497 (0.00083 nm) than for PWA 1484 (0.00042 nm).

1b. The nanoindentation hardness measurements by Atomic Force Microscopy (NI-AFM) reveal that there is no tendency or clear difference in the nanohardness of γ and γ' phase in the samples after different creep deformation of both superalloys. The hardness of the γ' precipitates of the PWA 1484 superalloy is slightly higher than the hardness of the γ' phase of

the PWA 1497. The γ matrix of the PWA 1497 superalloy is on average 0.8 GPa harder than that of the PWA 1484 due to higher content of rhenium and ruthenium, since they partition predominantly to the γ phase.

2. The microstructure of 4th generation PWA 1497 superalloy, exhibits a higher stability during isothermal ageing at 980 ˚C up to 900 h than the microstructure of the PWA 1484 superalloy aged at the same conditions.

3. The 4th generation PWA 1497 superalloy exhibits much more stable microstructure than 2nd generation PWA 1484 superalloy creep tested in the same conditions (982 ˚C and 248 MPa), what explains nearly three times better creep resistance of this superalloy. Microstructural changes caused by creep deformation at high temperature of 4th generation superalloy are qualitatively very similar to those of 2nd generation superalloy but the rate of changes is much slower.

4. The results of microstructural parameters measurments show that the PWA 1497 superalloy can endure by deformation at 982 ˚C about 60 MPa higher stress than the PWA 1484 superalloy, maintaining at the same time similar microstructure changes.

5. The higher stability of 4th generation superalloy PWA 1497 is related with significantly stronger solid solution strengthening, what results in higher hardness of γ matrix phase in comparison with 2nd generation PWA 1484 superalloy.

LITERATURE

[1] A. Czyrska-Filemonowicz, B. Dubiel, M. Ziętara, A. Cetel, "Development of single crystal Ni-based superalloys for advanced aircraft turbine blades", Inżynieria Materiałowa 3-4, 2007, pp. 128-133.

[2] M. Zitara, A. Cetel, A. Czyrska-Filemonowicz – „Microstructure Stability of 4th Generation Single Crystal Superalloy, PWA 1497, during High Temperature Creep Deformation", Materials Transactions, Vol. 52, No.03, 2011, pp.336-339.

[3] S. Walston, A. Cetel, R. MacKay, K. O'Hara, D. Duhl, R. Dreshfield - "Joint Development of a Fourth Generation Single Crystal Superalloy", Superaloys 2004, K.A. Green, et al. (eds), TMS (The Minerals, Metals & Materials Society), 2004, pp. 15-24.

[4] R.C. Reed – "The Superalloys: Fundamentals and Application", Cambridge University Press, Cambridge, 2006.

[5] M.J. Donachie, S.J. Donachie – "Superalloys a technical guide", ASM International, 2002.

[6] M. Kamaraj – "Rafting in single crystal nickel-base superalloys – An overview", Sadhana, Vol. 28, Parts 1 & 2, 2003, pp. 115-128.

[7] http://en.wikipedia.org/wiki/File:TurbineBlades.jpg

[8] Y. Koizumi, T. Kobayashi, T. Yokokawa, J. Zhang, M. Osawa, H. Harada, Y. Aoki, M. Arai - "Development of Next-Generation Ni-Base Single Crystal Superalloys", Superalloys 2004, K.A. Green et al. (eds), TMS (The Minerals, Metals & Materials Society), 2004, pp. 35-43.

[9] A. Sato, A.C. Yeh, Y. Kobayashi, T. Yokokawa, H. Harada, T. Murakumo, J. Zhang - "A 5th Generation Ni-base Single Crystral Superalloy with Superior Elevated Temperature Properties", Proc. 8th Conference on Materials for Advanced Power Engineering, Liege 2006, J. Lecomte-Beckers, F. Schubert, P.J. Ennis (eds), Schriften des Forschungszentrum Jülich, Reihe Energietechnik, 53-1, 2006, pp. 287-298.

[10] J.R. Davis (ed.) - "Directionally Solidified and Single-Crystal Superalloys", ASM Specialty Handbook: Heat-Resistant Materials, ASM International, 1997.

[11] P. Carron, T. Khan - "Evolution of Ni-based Superalloys for Single Crystal Gas Turbine Blade Application", Aerosp. Sci. Technol. 3, 1999, pp. 513-523.

[12] Y. Aoki, M. Arai, K. Chikugo, Y. Koizumi, H. Harada - "Mechanical Properties and Castability of a 4th Generation Ni-base Single Crystal Superalloy TMS-138", Proc. of the International Gas Turbine Congress 2003, Tokyo, 2-7.11.2003, pp. 1-6.

[13] http://www.nims.go.jp/eng/news/nimsnow/

[14] B. J. Piearcey - "Apparatus for producing single crystal metallic alloy objects", United States Patent 3542120, 11/24/1970.

[15] A. Onyszko, K. Kubiak, J. Sieniawski – "Turbine blades of the single crystal nickel based CMSX-6 superalloy", Journal of Achievements in Materials and Manufacturing Engineering, Vol. 32, No 1, 2009, pp. 66-69.

[16] M. Gell, D.N. Duhl, A.F. Giamei – "The Development of Single Crystal Superalloy Turbine Blades", Superalloys 1980, J.K. Tien et al. (eds), American Society for Metals, Metals Park, 1980, pp. 205-214.

[17] M. Durand-Charre – "The Microstructure of Superalloys", Gordon and Breach Science Publishers, Canada, 1997.

[18] S.R. Hegde, R.M. Kearsey, J.C. Beddoes – "Designing homogenization–solution heat treatments for single crystal superalloys", Materials Science and Engineering A, Vol. 527, 2010, pp. 5528–5538.

[19] M.S.A. Karunaratne, D.C. Cox, P. Carter, R.C. Reed, K.A. Green – " Modeling of the microsegregation in CMSX-4 superalloy and its homogenization during heat treatment", in Superalloys 2000, T.M. Pollock et al. (eds), TMS (The Minerals, Metals and Materials Society), 2000, pp. 263–272.

[20] G.E. Fuchs – "Solution heat treatment response of a third generation single crystal Ni-base superalloy", Materials Science and Engineering A, Vol. 300, 2001, pp. 52–60.

[21] G.L. Erickson – "A New, Third Generation, Single-Crystal, Casting Superalloy", Journal of Metals, Vol. 47, No. 5, 1995, pp. 36-39.

[22] T. Penkala – „Zarys Krystalografii", PWN Warszawa, 1972 pp.190-191.

[23] T. Murakumo, T. Kobayashi, Y. Koizumi, H. Harada – "Creep behaviour of Ni-base single-crystal superalloys with various γ′ volume fraction", Acta Materialia, Vol 52, 2004, pp. 3737–3744.

[23] T. Murakumo, T. Kobayashi, Y. Koizumi, H. Harada – "Creep behaviour of Ni-base single-crystal superalloys with various γ′ volume fraction", Acta Materialia, Vol 52, 2004, pp. 3737–3744.

[24] D. Goldschmidt - „Single-crystal blades in Materials for Advanced Power Engineering", Part 1, D.Coutsouradis, J.H. Davidson, J. Ewald, P. Greenfield, T. Khan, M. Malik, DB Meadowcroft (eds), Kluwer Academic Publishers, Sept. 1994, pp. 661-674.

[25] F. Diologent, P. Caron, T. d'Almeida, A. Jacques, P. Bastie – "The γ/γ′mismatch in Ni based superalloys: In situ measurements during a creep test", Nuclear Instruments and Methods in Physics Research B, Vol 200, 2003, pp. 346–351.

[26] H. A. Kuhn, H. Biermann, T. Ungar and H. Mughrabi – "X-ray study of creep deformation induced changes of the lattice misfit in the gamma prime hardened monocrystalline nickel-base superalloy SRR99", Acta Metallurgica et Materialia, Vol. 11, 1991, pp. 2783–2794.

[27] T. Sugui, W. Minggang, Y. Huichen, Y. Xingfu, L.Tang, Q. Benjiang – ”Influence of element Re on lattice misfits and stress rupture properties of single crystal nickel-based superalloys”, Materials Science and Engineering A, Vol. 527, 2010, pp. 4458–4465.

[28] Q. Z. Chen, D. M. Knowles – “The microstructures of base/modified RR2072 SX superalloys and their effects on creep properties at elevated temperatures”, Acta Materialia, Vol. 50, 2002, pp. 1095–1112.

[29] A. Defresne, L. Remy – “Fatigue behaviour of CMSX 2 superalloy [001] single crystals at high temperature I: Low cycle fatigue of notched specimens”, Materials Science and Engineering A, Vol. 129, 1990, pp. 45-53.

[30] C.M.F Rae, R.C. Reed – “The precipitation of topologically close-packed phases in rhenium-containing superalloys”, Acta Mater., Vol. 49, 2001, pp. 4113-4125.

[31] M. Pessah-Simonetti, P. Donnadieu, P. Caron – “T.C.P. phase particles embedded in a superalloy matrix: Interpretation and prediction of the orientation relationships”, Scripta Metallurgica et Materialia, Vol. 30, 1994, pp. 1553-1558.

[32] M. Simonetti, P. Caron – “Role and behaviour of μ phase during deformation of a nickel-based single crystal superalloys”, Materials Science and Engineering A, Vol. 254, 1998, pp. 1-12.

[33] A. Sato, H. Harada, T. Yokokawa, T. Murakumo, Y. Koizumi, T. Kobayashi, H. Imai – “The effects of ruthenium on the phase stability of fourth generation Ni-base single crystal superalloys”, Scripta Materialia, Vol. 54, 2006, pp. 1679–1684.

[34] D.P. Pope, S.S. Ezz - “Mechanical properties of Ni_3Al and nickel-base alloys with high volume fraction of γ’ ”, International Metals Reviews, Vol. 29, 1984, pp. 137-166.

[35] A. Royer, P. Bastie, M. Veron - “In situ determination of γ‘ phase volume and of relations between lattice parametres and precipitate morphology in Ni-based single crystal superalloy”, Acta Mater. Vol. 46, 1998, pp. 5357-5368.

[36] I.M. Wilcock, P. Lukas, M. Maldini, J. Klabbers, B. Dubiel, M.B. Henderson - "The creep behaviour of as-cast SX CM186LC at industrial gas turbine operating conditions", Proc. 7 Int. Conference on Materials for Advanced Power Engineering 2002, 30.09-2.10.2002, Liege, J. Lecomte-Beckers, M. Caron, F. Schubert, P.J. Ennis (eds), Schriften des Forschungszentrum Jülich, 21, 2002, pp. 139-148.

[37] F.R.N. Nabarro, C.M. Cress, P. Kotschy - “Thermodynamic driving force for rafting in superalloys,” Acta Mater. Vol. 44, 1996, pp. 3189-3198.

[38] C.K. Bullough, M. Toulious, M. Oehl, P. Lukas - “The characterization of the single crystal superalloy CMSX-4 for industrial gas turbines blading applications”, Proc. 6th Conference on Materials for Advanced Power Engineering, Liege, 5-7.10.1998, ed. by J.Lecomte-Beckers, F. Schubert (eds), 1998, pp. 316 – 322.

[39] A. Epishin, T. Link, U. Brückner, P.D. Portella - "Kinetics of the topological inversion of the γ/γ' microstructure during creep of a nickel-based superalloy", Acta Mater. Vol. 49, 2001, pp. 4017-4023.

[40] LAUE non-commercial computer software developed at the Faculty of Metal Engineering and Industrial Computer Science of the AGH University of Science and Technology.

[41] MAKRO 50 non-commercial computer software developed at the Faculty of Metal Engineering and Industrial Computer Science of the AGH University of Science and Technology.

[42] http://cimewww.epfl.ch/people/stadelmann/jemsWebSite/jems.html

[43] M. Göken, M. Kempf – "Microstructural properties of superalloys investigated by nanoindentations in an atomic force microscope", Acta Mater., Vol. 47, 1999, pp. 1043-1052.

[44] K. Durst, M. Göken – "Micromechanical characterisation of the influence of rhenium on the mechanical properties in nickel-base superalloys", Materials Science and Engineering A, 2004, pp. 312–316.

[45] S. Neumeier, M. Dinkela, F. Pyczak, M. Göken – "Nanoindentation and XRD investigations of single crystalline Ni–Ge brazed nickel-base superalloys PWA 1483 and René N5", Materials Science and Engineering A, Vol. 528, 2011, pp. 815–822.

[46] W.C. Oliver, G.M. Pharr - "An Improved Technique for Determining Hardness and Elastic-Modulus Using Load and Displacement Sensing Indentation Experiments", J. Mater. Res., Vol. 7, 1992, pp. 1564-1583.

[47] T. Schöberl, H.S. Gupta, P. Fratzl - "Measurements of mechanical properties in Ni-base superalloys using nanoindentation and atomic force microscopy", Materials Science and Engineering A, Vol. 363, 2003, pp. 211–220.

[48] Image analysis software of Soft Imaging System GmbH, http://www.softimaging.net

[49] N. Matan, D. C. Cox, C.M.F. Rae, R.C Reed - "On the kinetics of rafting in CMSX-4 superalloy single crystals", Acta Mater., Vol. 47, 1999, pp. 2031-2045.

[50] A. Epishin - materials from the COST 538 meeting, Baden, Switzerland, 24-25 October 2005, unpublished.

[51] M. Ignat, J. Y. Buffiere, J. M. Chaix - "Microstructures induced by stress gradient in nickel-base superalloy", Acta Metal. Mater., Vol. 41, 1993, pp. 855-862.

[52] A.J. Kubis, G.J. Shiflet, D.N. Dunn, R. Hull – „Focused Ion-Beam Tomography", Metalurgical and Materials Transactions A, Vol.35, 2004, pp 1935-1943.

[53] M.D. Uchic, M.A. Groeber, D.M. Dimiduka, J.P. Simmons – "3D microstructural characterization of nickel superalloys via serial-sectioning using a dual beam FIB-SEM", Scripta Materialia, Vol. 55, 2006, pp. 23–28.

[54] O. Hassomeris, G. Schumacher, M. Krüger, M. Heilmaier, J. Banhart – "Phase continuity in high temperature Mo-Si-B alloys: A FIB-Tomography Study", Intermetallics, Vol. 19, 2011, pp. 470-475.

[55] http://fiji.sc/wiki/index.php/Fiji

[56] http://www.vsg3d.com/avizo/fire

[57] www.mavi-3d.de3d-analyse.itwm.fraunhofer.dewww.itwm.fraunhofer.de

[58] A. Epishin, T. Link, H. Harada, Y. Koizumi and T. Kobayashi: Superalloys 2004, K.A. Green et al. (eds), The Minerals, Metals & Materials Society, 2004, pp. 137-143.

[59] F. Pyczak, S. Neumeier, M. Göken - "Influence of lattice misfit on the internal stress and strain states before and after creep investigated in nickel-base superalloys containing rhenium and ruthenium", Materials Science and Engineering A, 510–511, 2009, pp. 295–300

[60] F. Pyczak, B. Devrient, H. Mughrabi – "The Effects of Different Alloying Elements on the Thermal Expansion Coefficients, Lattice Constants and Misfit of Nickel-Based Superalloys Investigated by X-Ray Diffraction", Proceedings of the 10th International Symposium on Superalloys, 2004, pp. 827–836.

[61] A.P. Ofori, C.J. Humphreys, S. Tin, C.N. Jones – "A TEM Study of the Effect of Platinum Group Metals in Advanced Single Crystal Nickel-Base Superalloys", Proceedings of the 10th International Symposium on Superalloys, 2004, pp. 787–793.

[62] L.J. Carroll, Q. Feng, J.F.Mansfield, T.M. Pollock – "High refractory, low misfit Ru-containing single-crystal superalloys", Metall. Mater. Trans. A, Vol. 37, 2006, pp. 2927–2938.

[63] J.H. Liao, H.Y. Bor, C.G. Chao, T.F. Liu – "Effects of Rhenium on Microstructure and Phase Stability of MAR-M247 Ni-Base Fine-Grain Superalloy", Mater. Trans., Vol 51, 2010, pp. 810-817.

[64] F. Pyczak, B. Devrient, F.C. Neuner, H. Mughrabi – "The influence of different alloying elements on the development of the γ/γ′ microstructure of nickel-base superalloys during high-temperature annealing and deformation", Acta Materialia, Vol. 53, 2005, pp. 3879-3891.

[65] Y.H. Zhang, D.M. Knowles, P.J. Withers – "Microstructural development in Pt-aluminide coating on CMSX-4 superalloy during TMF", Surface and Coatings Technology, Vol. 107, 1998, pp. 76–83.

[66] K.Y. Cheng, C.Y. Jo, D.H. Kim, T. Jin, Z.Q. Hu – "Influence of local chemical segregation on the γ′ directional coarsening behavior in single crystal superalloy CMSX-4" Materials Characterization Vol. 60, 2009, pp. 210-218.

[67] A. Szczotok, J. Richter, J. Cwajna – „Stereological characterization of γ′ phase precipitation in CMSX-6 monocrystalline nickel-base superalloy", Materials Characterization, Vol. 60, 2009, pp.1114-1119.

[68] A. Bourhettar, A. Hazotte, M. Troyon – "Atomic Force Microscopy imaging to measure precipitate volume fraction in nickel-based superalloys", Materials Characterization, Vol. 34, 1995, pp. 265-270.

[69] H. Zhou, Y. Ro, H. Harada, Y. Aoki, M. Arai – "Deformation microstructures after low-cycle fatigue in a fourth-generation Ni-base SC superalloy TMS-138", Materials Science and Engineering A, Vol. 381, 2004, pp. 20-27.

[70] A.C. Yeh, A. Sato, T, Kobayashi, H, Harada – "On the creep and phase stability of advanced Ni-base single crystal superalloys", Materials Science and Engineering A, Vol 490, 2008, pp. 445–451.

[71] U. Hemmersmeier, M. Feller-Kniepmeier – „Element distribution in the macro- and microstructure of Nikel base superalloy CMSX-4", Materials Science and Engineering A, Vol. 248, 1998, pp. 87–97.

LIST OF SYMBOLS

IGT- Industrial Gas Turbines
DS - Directionally Solidified
SC - Single Crystal
CC - Conventionally Cast
TCP - Topologically Closed Packed
ΔT – solutioning window
γ' - Ni_3Al strengthening phase
γ - matrix phase
γ/γ'- eutectic areas;
γ-γ'- interface between γ and γ'
δ - lattice mismatch
LI_2 –structure Ni_3Al
a_γ - γ lattice parameter
$a_{\gamma'}$ - γ' lattice parameter
MC- melt (cast) carbides
σ - normal stress
f.c.c. - Face-Centred Cubic
LM - Light Microscopy
SEM - Scanning Electron Microscopy
TEM - Transmission Electron Microscopy
SAED - Selected Area Electron Diffraction
AFM- Atomic Force Microscopy
NI-AFM - Nanoindentation in Atomic Force Microscopy
FIB – Focused Ion Beam
SANS - Small Angle Neutron Scattering
$\mathbf{f_s}$ - surface fraction of γ' particles
$\mathbf{V_v}$ - volume fraction of γ' particles
D - mean size of γ' particles
k - shape coefficient
S - mean width of γ phase (channels)
T – mean thickness of γ' phase
L – mean length of γ' phase
R – rafting parameter, defined as: ***R=L/(2T)***

Acknowledgements

This work was partially supported by Pratt & Whitney, US under Contract No 24117 I would like to acknowledge Pratt & Whitney for providing the materials used in this investigation and for permission to publish the results.

I greatly appreciate the help of my supervisor Prof. Aleksandra Czyrska-Filemonowicz, Dr Beata Dubiel as well as following personae in completing my PhD thesis:

Prof. P.J. Ennis, Prof. P.A. Buffat, Prof. W. Ratuszek, Dr. W. Osuch, Prof. S. Dymek. Prof. K. Wiencek, Dr A. Wusatowska-Sarnek, MSc. G. Cempura, MSc. A. Gruszczyński, Mrs. K. Płońska-Niżnik

Stabilność mikrostruktury monokrystalicznych nadstopów niklu II i IV generacji podczas wysokotemperaturowego pełzania

Akademia Górniczo Hutnicza im. Stanisława Staszica w Krakowie
Wydział Inżynierii metali i Informatyki Przemysłowej

mgr inż. Maciej Ziętara

Streszczenie

Nadstopy niklu stosowane są jako materiały na łopatki turbin silników odrzutowych i stacjonarnych turbin gazowych w przemyśle energetycznym.
W pracy przedstawiono wnikliwą analizę stabilności mikrostruktury monokrystalicznych nadstopów niklu II generacji (PWA 1484) i IV generacji (PWA 1497) podczas procesu wysokotemperaturowego pełzania oraz starzenia, ze szczególnym uwzględnieniem geometrycznego opisu ewolucji mikrostruktury w obu nadstopach.
Metodami skaningowej mikroskopii elektronowej (SEM), transmisyjnej mikroskopii elektronowej (TEM) oraz skaningowo-transmisyjnej mikroskopii elektronowej (STEM) przeprowadzono ilościową i jakościową analizę mikrostruktury nadstopów oraz wyznaczono parametry stereologiczne faz γ i γ'. Wykonano również badania rentgenowskie, wyznaczając dla obu nadstopów w stanie dostawy współczynnik niedopasowania sieci (δ) w temperaturze pokojowej. Przeprowadzono badania nano-twardości faz γ i γ' w obu nadstopach (NI-AFM) za pomocą mikroskopii sił atomowych. Ponadto dla nadstopu IV generacji PWA 1497 przeprowadzono trójwymiarową wizualizację mikrostruktury za pomocą tomografii elektronowej z wykorzystaniem skaningowego mikroskopu elektronowego z działem jonowym. Wykonane badania pozwoliły na porównanie stabilności mikrostruktury obu nadstopów odkształconych przez pełzanie w wysokiej temperaturze. W wyniku przeprowadzonych badań stwierdzono większą stabilność mikrostruktury nadstopu IV generacji, PWA 1497 podczas pełzania w wysokiej temperaturze w porównaniu z mikrostrukturą nadstopu II generacji PWA 1484.

Wstęp

Rozwój monokrystalicznych nadstopów na osnowie niklu trwa już od ponad czterdziestu lat. Wprowadzenie tej grupy materiałów do zastosowania na łopatki turbin silników odrzutowych jest uważane za jedno z największych osiągnięć technologicznych ostatnich dwóch dekad. Monokrystaliczne nadstopy niklu cechują się miedzy innymi dużą odpornością na pełzanie oraz wytrzymałością w wysokich temperaturach. Te dobre właściwości zawdzięczają umocnieniu osnowy γ koherentnymi cząstkami fazy γ' o dużym ułamku objętości. Monokrystaliczne nadstopy niklu są stosowane głównie jako materiał na łopatki turbin silników odrzutowych oraz przemysłowych turbin gazowych. Łopatki turbin pracują w bardzo wysokich temperaturach i poddawane są naprężeniom rozciągającym, spowodowanym działaniem siły odśrodkowej, co powoduje pełzanie materiału. W trakcie procesu pełzania monokrystalicznych nadstopów niklu dochodzi do kierunkowej koagulacji fazy γ'; proces ten określany jest w literaturze angielskojęzycznej jako „rafting". Rozpoczęcie procesu kierunkowej koagulacji fazy γ' odbywa się w początkowym stadium pełzania w wysokiej temperaturze (powyżej 900°C) oraz niskim naprężeniu (około 100 MPa). Zjawisko „raftingu"

polega na zmianie kształtu sześciennych wydzieleń fazy γ' na długie płytkowe wydzielania, które w późniejszej fazie procesu zmieniają morfologię i ulegają pofałdowaniu. Końcowym etapem kierunkowej koagulacji fazy γ' jest topologiczna inwersja mikrostruktury faz γ-γ'. Zjawisko „raftingu" w znacznym stopniu determinuje odporność monokrystalicznych nadstopów niklu na pełzanie w wysokich temperaturach.
Rozwój monokrystalicznych nadstopów niklu jest spowodowany dążeniem do ciągłego podwyższania temperatury eksploatacyjnej turbin gazowych. Dąży się do ustalenia optymalnego składu chemicznego monokrystalicznych nadstopów niklu, który zapewniłby polepszenie odporności na pełzanie oraz wytrzymałości na zmęczenie mechaniczne i cieplne. Warunkiem polepszania odporności na pełzanie jest poprawa stabilności mikrostruktury nadstopów podczas pełzania.

Cel badań

Ustalenie zmian mikrostruktury monokrystalicznych nadstopów na osnowie niklu podczas pracy w wysokich temperaturach i znacznym obciążeniu, wymaga systematycznych badań przy użyciu mikroskopii elektronowej.

Dostępne publikacje naukowe ograniczają się do opisu zmian mikrostruktury niektórych nadstopów drugiej generacji, zachodzących w początkowych stadiach ich pełzania. Natomiast brak jest danych literaturowych opisujących stabilność mikrostruktury monokrystalicznych nadstopach niklu czwartej generacji.

Znajomość stabilności mikrostruktury jest najważniejszym czynnikiem przy przewidywaniu właściwości mechanicznych monokrystalicznych nadstopów niklu, koniecznych do pracy w krytycznych warunkach na elementy łopatek silników odrzutowych oraz przemysłowych turbin gazowych. Szczególnie ważny jest dokładny ilościowy opis ewolucji mikrostruktury nadstopów za pomocą parametrów stereologicznych. Dane te są wykorzystywane do ciągłego rozwoju modeli matematycznych wspomagających projektowanie nowych materiałów na elementy silników lotniczych i przemysłowych turbin gazowych.

Celem badań było porównanie stabilności mikrostruktury monokrystalicznych nadstopów niklu drugiej generacji (nadstop PWA 1484) oraz czwartej generacji (nadstop PWA 1497), podczas wysokotemperaturowego pełzania, ze szczególnym uwzględnieniem geometrycznego opisu ewolucji mikrostruktury w obu nadstopach.

Materiały i metodyka badań

Materiałem do badań były dwa nadstopy na osnowie niklu dostarczone prze firmę Pratt & Whitney, US w postaci prętów o średnicy 20 mm po obróbce cieplnej. Skład chemiczny badanych nadstopów przedstawiono w Tabeli 1.

Tabela 1. Skład chemiczny nadstopów PWA 1484 oraz PWA 1497 (% masy)

Materiał	Cr	Co	Mo	Re	Ru	W	Al	Ta	Hf
PWA 1484	5	10	2	3	-	6	5,6	8,7	0,1
PWA 1497	2	16,5	2	5,95	3	6	5,55	8,25	0,15

Warunki obróbki cieplnej dla nadstopów PWA 1484 i PWA 1497 nie zostały ujawnione przez firmę Pratt & Whitney (badania do pracy doktorskiej wykonano w projektach realizowanych z klauzurą poufności).

Próby pełzania zostały przeprowadzone w Instytucie Lotnictwa w Warszawie. Wszystkie próbki zostały przygotowane z zachowaniem krystalograficznej orientacji <001> wzdłuż osi próbki. Geometria przygotowanych próbek została przedstawiona na Rys. 20 w rozprawie doktorskiej.
Dwadzieścia dwie próbki (10 próbek z nadstopu PWA 1484 oraz 12 próbek z nadstopu PWA 1497) zostało poddanych pełzaniu w tej samej temperaturze (982ºC, co odpowiada 1800ºF) przy różnym naprężeniu i różnych stopniach odkształcenia. Dokładny opis warunków pełzania poszczególnych próbek został przedstawiony w Tabelach 7 i 8 rozprawy.

Schemat przygotowania próbek do badan XRD, LM, SEM, TEM oraz AFM został przedstawiony na Rys. 22.

Badania rentgenowskie próbek w stanie dostawy obejmowały pomiary orientacji krystalograficznej (wykonane za pomocą dyfraktometru TuR M60) oraz pomiary współczynnika niedopasowania sieci γ/γ' (wykonane za pomocą dyfraktometru D500 SIEMENS).

Badania mikrostruktury wykonano za pomocą mikroskopów świetlnych OPTECH model XJL-17, AXIO Imager M1m, skaningowego mikroskopu elektronowego CAMBRIDGE STEREOSCAN 120, mikroskopu elektronowego SEM/FIB NEON 40EsB CrossBeam, oraz transmisyjnych mikroskopów elektronowych JEOL JEM-200CX i JEM-2010 ARP. Cienkie folie do badań TEM wykonano metodą strumieniowego polerowania elektrolitycznego w odczynniku o składzie 450 ml $CH_2OHCH_2OC_4H_9$ + 450 ml CH_3COOH + 100 ml $HCLO_4$, przy napięciu 26 V i w temperaturze -4 °C.

Tomografię elektronową wykonano dla nadstopu IV generacji PWA 1497 dla próbki w stanie dostawy oraz po zerwaniu podczas procesu pełzania. Do przedstawienia mikrostruktury w trójwymiarowej przestrzeni wykorzystano skaningowy mikroskop elektronowy z działem jonowym (FIB). Trójwymiarową wizualizację mikrostruktury materiału wykonano za pomocą oprogramowania komputerowego, Avizo Fire 6.2.

Badania nano-twardości wykonano w temperaturze pokojowej za pomocą mikroskopu sił atomowych Veeco Instruments wyposażonym w przystawkę do badań nano-twardości - Triboscope force transducer firmy Hysitron. Badania nano-twardości przeprowadzono na wybranych próbkach obu nadstopów (Tabela 9). Schemat wykonywania pomiaru nano-twardości został przedstawiony na Rys. 24.

Analiza obrazów mikrostruktury uzyskanych za pomocą skaningowej oraz transmisyjnej mikroskopii elektronowej została przeprowadzona za pomocą komercyjnego oprogramowania komputerowego “AnalySIS 3.2”.

Stereologiczna procedura charakteryzacji mikrostruktury materiałów w stanie dostawy obejmowała wyznaczenie następujących parametrów mikrostruktury:
f_s - udział powierzchniowy wydzieleń fazy γ'
V_v - udział objętościowy wydzieleń fazy γ' ($f_s \cong V_v$)
d – średnia wielkość wydzieleń fazy γ', (Rys. 25)

k – współczynnik kształtu, (Rys. 26)
S – średnia szerokość kanałów fazy γ

Schematyczne przedstawienie sposobów detekcji wydzieleń fazy γ' zostało przedstawione na Rys. 27.

Stereologiczna procedura charakteryzacji mikrostruktury materiałów po procesie pełzania, obejmowała wyznaczenie następujących parametrów mikrostruktury, opisujących w sposób geometryczny stopień ewolucji mikrostruktury.
L – średnia długość powierzchni międzyfazowej γ/γ' (w kierunku prostopadłym do kierunku naprężenia)
T – średnia szerokość fazy γ' (w kierunku równoległym do kierunku naprężenia)
S – średnia szerokość fazy γ (w kierunku równoległym do kierunku naprężenia)
R – parametr raftingu, zdefiniowany jako: R=L/(2T)

Parametry ***T*** i ***S*** zostały wyznaczone na podstawie obrazów mikrostruktury uzyskanych za pomocą transmisyjnej mikroskopii elektronowej (TEM). Do wyznaczenia parametrów użyto metody siecznych, schemat wyznaczania tych parametrów został przedstawiony na Rys. 28. Parametr ***L*** został wyznaczony na podstawie obrazów mikrostruktury uzyskanych za pomocą skaningowej mikroskopii elektronowej (SEM).
Procedura wyznaczania parametru ***L*** oparta była na analizie poziomego rzutu granicy międzyfazowej γ/γ', wyodrębnionej dzięki jednostronnemu filtrowaniu gradientowemu, górno i dolno przepustowemu. Uzyskane wyniki zostały następnie uśrednieniu zgodnie ze wzorem $L = (L_{górny} + L_{dolny})/2$. Sposób wyznaczania parametru mikrostruktury L został schematycznie przedstawiony na Rys. 29.

Wyniki badań i ich dyskusja

I. Materiały w stanie dostawy

Badania mikrostruktury nadstopów II (PWA 1484) oraz IV (PWA 1497) generacji w stanie dostawy ujawniły, że oba nadstopy posiadają mikrostrukturę składającą się z regularnych sześciennych wydzieleń fazy γ' rozdzielonych kanałami fazy γ oraz resztkowej eutektyki γ-γ'. Wyniki pomiarów wykazały, że oba nadstopy posiadają podobne wielkości parametrów mikrostruktury. Średnia średnica wydzieleń fazy γ'
(**D**) dla nadstopu PWA 1484 osiągnęła nieznacznie większą wartość 447 nm w porównaniu z nadstopem PWA 1497 dla którego średnia średnica wydzieleń fazy γ' posiadała wartość 442 nm. Średnia szerokość kanałów fazy γ (**S**) osiągnęła większą wartość dla nadstopu PWA 1497 (70 nm) niż dla nadstopu PWA 1484 (63 nm). Udział objętościowy fazy γ' ($\mathbf{V_v}$) dla nadstopu PWA 1484 osiągnął większą wartość (79%) niż dla nadstopu PWA 1497 (72%). Pomiary udziału objętościowego fazy γ' dla nadstopu IV generacji (PWA 1497) zostały również potwierdzone (69%) badaniami za pomocą tomografii elektronowej z wykorzystaniem skaningowego mikroskopu elektronowego z działem jonowym (FIB). Różnice parametrów mikrostruktury oraz udziału objętościowego fazy γ' obu nadstopów (PWA 1484 i PWA 1497) związane są z różnicami w składzie chemicznym oraz obróbce cieplnej tych nadstopów.
Udział objętościowy fazy γ' w nowoczesnych monokrystalicznych nadstopach niklu sięga miedzy 70 a 80%. Według danych literaturowych, taki udział objętościowy fazy γ' stanowi obecnie optymalną wartość. Jednak dla nadstopu II generacji CMSX-4 w literaturze można

znaleźć różne wartości udziału objętościowego między 65 a 77% [64-67] oraz 69% dla nadstopu II generacji MC2 [68]. W przypadku monokrystalicznego nadstopu IV generacji (TMS-138) udział objętościowy fazy γ' został zmierzony jako 60% [69, 70].
Mikrostruktura monokrystalicznych nadstopów niklu w znacznym stopniu determinuje ich własności mechaniczne. Udział objętościowy, kształt oraz rozkład wielkości cząstek fazy γ' mogą być zoptymalizowane poprzez skład chemiczny oraz obróbkę cieplną nadstopów.

Pomiar współczynnika niedopasowania sieci γ/γ'

Wyniki badań współczynnika niedopasowania sieci γ/γ' (δ) w stanie dostawy ujawniły, że w temperaturze pokojowej oba nadstopy posiadają ujemną wartość tego współczynnika. Wartość współczynnika niedopasowania sieci waha się od -0.12 % dla nadstopu drugiej generacji (PWA 1484) do -0.26 % dla nadstopu czwartej generacji (PWA 1497). Parametry sieci faz γ oraz γ' ($a_{\gamma'}$ i a_{γ}) posiadają wyższe wartości dla nadstopu PWA 1497. Dla obydwu nadstopów parametr sieci fazy γ posiada wyższe wartości niż parametr sieci fazy γ' (Tabela 1). Różnica pomiędzy parametrami sieci (a_{γ}) oraz ($a_{\gamma'}$) jest znacznie większa (prawie dwukrotna) dla nadstopu PWA 1497 (0.00083 nm) niż dla nadstopu PWA 1484 (0.00042 nm).
Wyniki pomiarów można wytłumaczyć różnicą w składzie chemicznym obu nadstopów, a w szczególności zawartością renu (Re). Zawartość renu w nadstopie PWA 1497 (Re = 5,95%) jest prawie dwukrotnie wyższa niż w nadstopie PWA 1484 (Re = 3,0%). Ren dyfunduje głównie do fazy γ, co powoduje wzrost parametru jej sieci [59]. Ponadto, nadstop PWA 1497 zawiera dodatkowo w swym składzie chemicznym ruten (Ru) w ilości 3%, który również znacząco zwiększa parametr sieci fazy γ oraz w niewielkim stopniu parametr sieci fazy γ'. Ruten jest również odpowiedzialny za *„reverse partitioning effect"*, który został opisany również w innych nadstopach niklu zawierających ten pierwiastek [60-63]. Według Pyczaka i współautorów [59]efekt ten w niewielkim stopniu zmniejsza zawartość renu w osnowie γ ale podwyższa jego zawartość w wydzieleniach fazy γ', co wpływa na parametry sieci obu faz.

Badania nano-twardości faz γ oraz γ'

Badania nano-twardości obu nadstopów wykonane za pomocą mikroskopii sił atomowych wykazały, że faza γ' posiada zawsze wyższą twardość od fazy γ, co jest spowodowane różnicami w składzie chemicznym obu faz. Badania wykazały również że przy różnych stopniach odkształcenia brak wyraźnej różnicy w nano-twardości dla faz γ oraz fazy γ'. Świadczy to, że nano-twardość obu faz nie zmienią się wraz ze stopniem odkształcenia w trakcie pełzania lub zmiany nano-twardości są poza zdolnością rozdzielczą metody pomiarowej.
Twardość fazy γ' dla nadstopu PWA 1484 jest nieznacznie wyższa niż dla nadstopu PWA 1497. Osnowa fazy γ nadstopu PWA 1497 jest twardsza o średnio 0.8 GPa w stosunku do osnowy γ nadstopu PWA 1484. Jest to spowodowane wyższą zawartością renu i dodatkiem rutenu, które dyfundują głównie do osnowy γ nadstopu PWA 1497.
Podobne wyniki pomiarów nano-twardości zostały zaprezentowane przez Dursta i współautorów [44], którzy porównali nano-twardość faz γ oraz γ' w nadstopach I (CMSX-6), II (CMSX-4) oraz III (CMSX-10) generacji. Zgodnie z wynikami ich badań, nano-twardość fazy γ wzrasta wraz z zawartością renu, nie wpływa to natomiast na nano-twardość fazy γ'.
Wyższa stabilność mikrostruktury nadstopu IV generacji (PWA 1497) jest związana ze znacznie silniejszym umocnieniem roztworowym powodującym zwiększoną twardość osnowy γ w porównaniu z osnową nadstopu II generacji PWA 1484.

II. Stabilność mikrostruktury monokrystalicznych nadstopów niklu PWA 1484 i PWA 1497 podczas starzenia w wysokiej temperaturze

Wyniki badań mikrostrukturalnych obu nadstopów po izotermicznym starzeniu w temperaturze 980°C wykazały podobny charakter zmian; różnice wystąpiły jednak w szybkości koagulacji i koalescencji fazy γ'. Nadstop czwartej generacji, PWA 1497, poddany starzeniu w czasie 900 godzin charakteryzuje się znacząco stabilniejszą mikrostrukturą w porównaniu do nadstopu drugiej generacji, PWA 1484. Główną przyczyną tego efektu są różnice w składzie chemicznym obu nadstopów, wpływające na zmiany współczynnika niedopasowania sieci γ/γ'. Nadstop PWA 1497 charakteryzuje się bardziej ujemnym współczynnikiem niedopasowania sieci γ/γ', co wprowadza znacznie większe naprężenia wewnętrzne w mikrostrukturze nadstopu. Podczas starzenia sześcienne wydzielenia fazy γ' dążą do zminimalizowania naprężeń wywołanych niedopasowaniem sieci i ulegają koalescencji oraz koagulacji redukując powierzchnię międzyfazową. Nowe ułożenie wydzieleń fazy γ' powoduje poszerzenie kanałów osnowy γ, zwiększając w ten sposób możliwość ruchu dyslokacji. W końcowej fazie procesu koagulacji, wydzielenia fazy γ' tracą koherencję z osnową γ [17]. Znacząco wyższą stabilność monokrystalicznego nadstopu niklu czwartej generacji (PWA 1497) podczas starzenia w wysokiej temperaturze można tłumaczyć dłuższym czasem potrzebnym na relaksację naprężeń wewnętrznych spowodowanych bardziej ujemnym współczynnikiem niedopasowania sieci γ/γ'. Brak utraty sześciennego kształtu wydzieleń fazy γ' podczas długotrwałego starzenia w wysokiej temperaturze nadstopu PWA 1497 potwierdza tą hipotezę.

III. Stabilność mikrostruktury monokrystalicznych nadstopów niklu PWA 1484 i PWA 1497 podczas pełzania w wysokiej temperaturze

Podczas początkowego stadium pełzania monokrystalicznego nadstopu niklu PWA 1484 (druga generacja) w temperaturze 982°C, sześcienne wydzielenia fazy γ' w stadium ustalonego pełzania zaczynają łączyć się w długie płytkowe wydzielenia. Po około 260 h próby pełzania przy naprężeniu 193 MPa oraz 140 h przy naprężeniu 248 MPa, płytkowe wydzielenia fazy γ' widoczne są na całych obrazach SEM oraz TEM nawet przy małych powiększeniach. W dalszym ciągu procesu pełzania, płytkowe wydzielenia fazy γ' ulegają pofałdowaniu oraz zaczynają się ze sobą łączyć. Zmiany te prowadzą do tzw. „topologicznej inwersji mikrostruktury", proces ten został szczegółowo opisany przez Epishin i współautorów [39] W końcowej fazie procesu pełzania następuje dalszy rozrostu mikrostruktury γ-γ'.

Wyniki pomiarów parametrów stereologicznych mikrostruktury nadstopów odkształconych zarówno przy naprężeniu 193 MPa jak i przy naprężeniu 248 MPa przedstawiają podobną tendencję. Średnia szerokość fazy γ (*S*) wzrasta podczas procesu pełzania ponad sześciokrotnie dla próbek zerwanych przy naprężeniu 193 MPa w porównaniu ze stanem dostawy oraz ponad czterokrotnie dla próbek zerwanych przy naprężeniu 248 MPa. Zmiany parametru mikrostruktury *T* wykazały, że średnia szerokość fazy γ' wzrasta osiągając najwyższa wartość dla końcowego stopnia rozrostu mikrostruktury γ-γ'. Średnia długość powierzchni międzyfazowej γ/γ' (parametr *L*) maleje w trakcie ewolucji mikrostruktury w miarę jak faza γ' stają się bardziej pofałdowane, widoczne jest to zwłaszcza dla dłuższych czasów pełzania i mniejszego naprężenia. Zmiany parametru raftingu ($R = L / 2T$) wykazują, że parametr ten osiąga maksimum dla najdłuższych wydzieleń fazy γ' a następnie maleje dla najwyższych stopni odkształcenia i końcowego stopnia rozrostu mikrostruktury γ-γ'.

Wyniki pomiarów parametrów opisujących ewolucję mikrostruktury nadstopu PWA 1484 otrzymane w trakcie badań, są zgodne z wynikami opublikowanymi przez Matana i współautorów [49] którzy przeprowadzili badania kinetyki procesu raftingu w nadstopie drugiej generacji CMSX-4. Matan i współautorzy zwrócili uwagę na fakt, że interpretacja parametrów mikrostruktury (*L*, *T* oraz *S*) powinna być wykonywana z pewną ostrożnością. W początkowym stadium procesu raftingu kiedy wydzielenia fazy γ' są jeszcze krótkie i rozdzielone, parametry *L* i *T* odpowiadają średnim pomiarom długości i szerokości wydzieleń fazy γ'. W miarę postępowania kierunkowej koagulacji fazy γ', wydzielenia tej fazy stają się bardziej pofałdowane, a w konsekwencji czego parametr *L* przestaje odpowiadać dokładnie średniej długości wydzieleń fazy γ' (jednak w dalszym ciągu może być traktowany jako stopień zaawansowania procesu raftingu) [44].

Badania stabilności mikrostruktury monokrystalicznego nadstopu niklu PWA 1497 (czwarta generacja) podczas procesu pełzania zostały wykonane dokładnie w taki sam sposób jak dla nadstopu drugiej generacji, PWA 1484. Charakteryzacja nadstopu PWA 1497 po pełzaniu wykazała, że ewolucja mikrostruktury (opisana w sposób jakościowy) przebiegała w podobny sposób jak dla nadstopu PWA 1484.

Wyniki pomiarów parametrów stereologicznych opisujących ewolucję mikrostruktury nadstopu PWA 1497 podczas procesu pełzania w temperaturze 980 °C przy naprężeniach 248 MPa oraz 310 MPa przedstawiają podobną tendencję.

Średnia szerokość fazy γ (*S*) wzrasta w trakcie procesu pełzania, potrajając swoją wartość, dla próbek pełzanych do zerwania. Dla małych stopni odkształcenia (poniżej 1%), parametry *T* oraz *L* posiadają prawie stałe wartości, spowodowane jest to brakiem utraty sześciennego kształtu przez wydzielenia fazy γ'. Wzrost stopnia odkształcenia powyżej ~1% powoduje spadek średniej szerokości fazy γ' (parametr *T*), jest to związane ze wzrostem długości fazy γ' (parametr *L*) osiągającej wartość maksymalną dla ~2% odkształcenia. Dla wyższych stopni odkształcenia, parametr *T* wzrasta osiągając maksymalna wartość dla końcowego stopnia rozrostu mikrostruktury γ-γ'. Średnia długość powierzchni międzyfazowej γ/γ' (parametr *L*) maleje w miarę ewolucji mikrostruktury. Wartości parametru raftingu (*R*) wzrastają w początkowym stadium pełzania, osiągając maksimum dla najdłuższych wydzieleń fazy γ' (~2% odkształcenia), a następnie maleją dla wyższych stopni odkształcenia.

Porównanie wyników badań stabilności mikrostruktury monokrystalicznych nadstopów niklu drugiej oraz czwartej generacji, podczas pełzania w tych samych warunkach (982˚C, 248 MPa) wykazały że zmiany parametrów mikrostruktury *S, T, L* oraz *R* zachowują tą samą tendencję dla obu nadstopów. Jednak w przypadku nadstopu PWA 1497 (4 generacja) zmiany mikrostruktury zachodzą zdecydowanie wolniej, co świadczy o znacznie większej stabilności mikrostruktury nadstopu czwartej generacji podczas pełzania.

Wyniki badań stabilności mikrostruktury monokrystalicznych nadstopów niklu drugiej oraz czwartej generacji, podczas procesu pełzania w tej samej temperaturze (982˚C) ale przy różnym naprężeniu również zostały porównane i przedstawione w funkcji czasu pełzania. Zmiany parametrów mikrostruktury *S, T, L* oraz *R* dla nadstopu PWA 1484 (2 generacja) są tego samego rzędu wielkości jak dla nadstopu PWA 1497 (4 generacja) poddanego pełzaniu przy naprężeniu o 60 MPa większym. Świadczy to również o znacznie większej stabilności mikrostruktury nadstopu czwartej generacji.

Tomografia elektronowa monokrystalicznego nadstopu IV generacji PWA 1497

Tomografię elektronową z wykorzystaniem skaningowego mikroskopu elektronowego z działem jonowym wykonano celem trójwymiarowego zobrazowania mikrostruktury γ-γ' nadstopu IV generacji (PWA 1497) w stanie dostawy oraz mikrostruktury nadstopu po zerwaniu w próbie pełzania. Wyniki badań uzyskane metodami tomografii elektronowej porównano z wynikami pomiarów uzyskanych za pomocą TEM. Pomiary parametrów mikrostruktury oparte na trójwymiarowych rekonstrukcjach, wykazały że udział powierzchniowy (f_s) fazy γ' dla próbki w stanie dostawy wyniósł 70% natomiast udział objętościowy (V_v) został obliczony jako 69%. Dla próbki nr zerwanej w próbie pełzania udział powierzchniowy (f_s) wyniósł 75%, natomiast udział objętościowy (V_v) 74%. Wyniki pomiarów próbki w stanie dostawy prezentują zgodność z wynikami uzyskanymi za pomocą pomiarów TEM i potwierdzają, że w przypadku monokrystalicznych nadstopów niklu udział powierzchniowy fazy γ' jest porównywalny z udziałem objętościowym ($f_s \cong V_v$). Udział objętościowy fazy γ' w trakcie procesu pełzania pozostaje stały [71] jednak dla próbki nr 2 wzrósł on nieznacznie w porównaniu do próbki ze stanu dostawy, co prawdopodobnie zostało spowodowane błędem statystycznym związanym z miejscem pomiaru.

Wnioski

Zastosowanie nadstopów na osnowie niklu na najbardziej obciążone elementy lotniczych silników odrzutowych oraz przemysłowych turbin gazowych, wymaga kompleksowej wiedzy na temat stabilności mikrostruktury tych stopów w ekstremalnych warunkach pracy.
Na podstawie badań stabilności mikrostruktury nadstopów II (PWA 1484) oraz IV (PWA 1497) generacji stwierdzono, że:

1. Badania mikrostruktury nadstopów II i IV generacji w stanie dostawy ujawniły że mikrostruktura obu nadstopów składa się z regularnych sześciennych wydzieleń fazy γ' rozdzielonych kanałami fazy γ. Wyniki pomiarów wykazały, że oba nadstopy posiadają podobne wielkości parametrów mikrostruktury. Średnia średnica wydzieleń fazy γ' (**D**) dla nadstopu PWA 1484 osiągnęła nieznacznie większą wartość 447 nm w porównaniu z nadstopem PWA 1497 dla którego średnia średnica wydzieleń fazy γ' posiadała wartość 442 nm. Średnia szerokość kanałów fazy γ (**S**) osiągnęła większą wartość dla nadstopu PWA 1497 (70 nm) niż dla nadstopu PWA 1484 (63 nm). Udział objętościowy fazy γ' dla nadstopu PWA 1484 osiągnął większą wartość (79%) niż dla nadstopu PWA 1497 (72%). Pomiary udziału objętościowego fazy γ' dla nadstopu IV generacji PWA 1497 zostały również potwierdzone (69%) metodami tomografii elektronowej wykonanej z wykorzystaniem skaningowego mikroskopu elektronowego z działem jonowym (FIB).

1a. Wyniki badań rentgenowskich współczynnika niedopasowania sieci γ/γ' w stanie dostawy ujawniły, że w temperaturze pokojowej oba nadstopy posiadają ujemną wartość tego współczynnika. Wartość współczynnika niedopasowania sieci waha się od -0.12 % dla nadstopu drugiej generacji PWA 1484 do -0.26 % dla nadstopu czwartej generacji PWA 1497. Parametry sieci faz γ oraz γ' ($a_{\gamma'}$ i a_{γ}) posiadają wyższe wartości dla nadstopu PWA 1497. Dla obydwu nadstopów parametr sieci fazy γ posiada wyższe wartości niż parametr

sieci fazy γ'. Różnica pomiędzy parametrami sieci (a_γ) oraz ($a_{\gamma'}$) jest znacznie większa (prawie podwójna) dla nadstopu PWA 1497 (0,00083 nm) niż dla nadstopu PWA 1484 (0,00042 nm).

1b. Badania nano-twardości obu nadstopów wykonane za pomocą mikroskopu sił atomowych wykazały, że brak jest przy różnych stopniach odkształcenia wyraźnej różnicy w nano twardości faz γ oraz γ'. Twardość fazy γ' dla nadstopu PWA 1484 jest nieznacznie wyższa niż dla nadstopu PWA 1497. Osnowa fazy γ nadstopu PWA 1497 jest twardsza o średnio 0.8 GPa w stosunku do osnowy γ nadstopu PWA 1484. Jest to spowodowane wyższą zawartością renu i dodatkiem rutenu, które dyfundują głównie do osnowy γ nadstopu IV generacji.

2. Mikrostruktura nadstopu IV generacji, PWA 1497, podczas procesu starzenia w 980˚C w czasie 900 h wykazuje znacznie większą stabilność w porównaniu do mikrostruktury nadstopu II generacji, PWA 1484.

3. Nadstop IV generacji, PWA 1497, posiada znacząco większą stabilność mikrostruktury w porównaniu z nadstopem II generacji, PWA 1484, poddanym próbie pełzania w tych samych warunkach (982˚C, 248 MPa), co tłumaczy prawie trzykrotnie wyższą odporność na pełznie tego nadstopu. Zmiany mikrostruktury spowodowane odkształceniem przez pełzanie w wysokiej temperaturze obu nadstopów posiadają ten sam charakter, jednak szybkość zmian mikrostruktury nadstopu PWA 1497 jest znacznie mniejsza.

4. Wyniki pomiarów parametrów mikrostruktury wykazały, że nadstop IV generacji PWA 1497, poddany pełzaniu w temperaturze 982˚C można obciążyć o około 60 MPa wyższym naprężeniem w stosunku do nadstopu II generacji PWA 1484, utrzymując przy tym podobne zmiany mikrostruktury.

5. Wyższa stabilność mikrostruktury nadstopu IV generacji PWA 1497 jest związana ze znacznie silniejszym umocnieniem roztworowym tego nadstopu powodującym zwiększoną twardość osnowy γ w porównaniu z osnową nadstopu II generacji PWA 1484.